Improved Design of a High Lift System for General Aviation Aircraft

Master thesis

Dino Florjancic

Technische Universiteit Delft

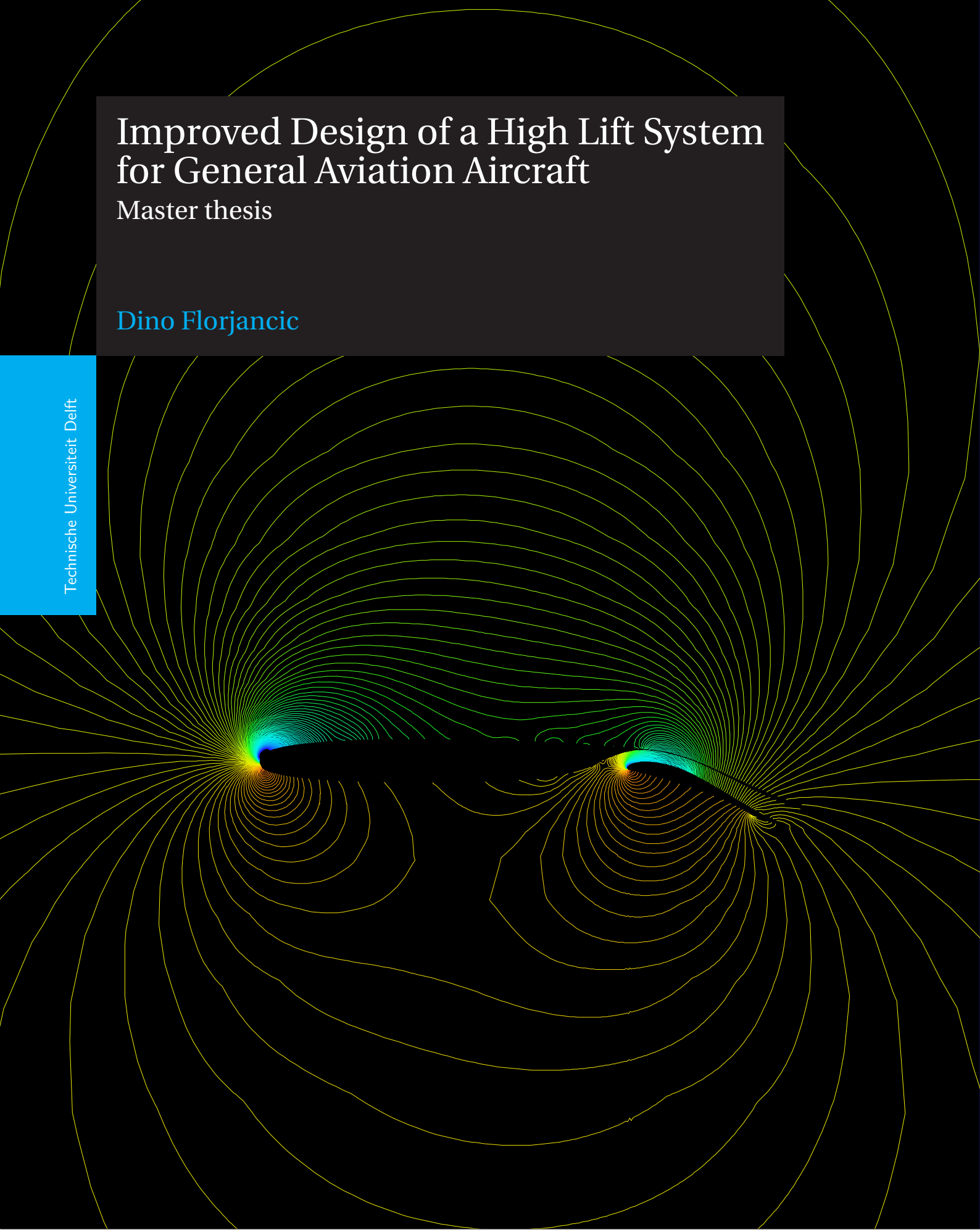

TU Delft Delft University of Technology

Challenge the future

IMPROVED DESIGN OF A HIGH LIFT SYSTEM FOR GENERAL AVIATION AIRCRAFT

MASTER THESIS

by

Dino Florjancic

in partial fulfillment of the requirements for the degree of

Master of Science

at the Delft University of Technology,

to be defended publicly on Tuesday August 25, 2015 at 1:30 PM.

Student number:	4317866
Tesis registraion number:	039#15#MT#FPP
Supervisors:	Prof. dr. ir. L. L. M. Veldhuis
	Ir. D. Steenhuizen

An electronic version of this thesis is available at http://repository.tudelft.nl/.

Department of Flight Performance and Propulsion
Faculty of Aerospace Engineering • Delft University of Technology

TU Delft Delft University of Technology

DELFT UNIVERSITY OF TECHNOLOGY
DEPARTMENT OF
FLIGHT PERFORMANCE AND PROPULSION

The undersigned hereby certify that they have read and recommend to the Faculty of Aerospace Engineering for acceptance a thesis entitled **Improved Design of a Hight Lift System for General Aviation Aircraft** by **Dino Florjancic** in partial fulfillment of the requirements for the degree of **Master of Science**.

Dated: August 25, 2015

Head of department:

Prof.dr.ir. L.L.M. Veldhuis

Supervisor:

Ir. Durk Steenhuizen

Reader:

Ir. W.A. Timmer

PREFACE

On the 19th of August 2013 I landed at the Schiphol airport for the first time. In the next two years, another 22 flights would follow, allowing me to migrate between The Netherlands and Slovenia in order to study abroad and still keep in touch with my home. This is only possible because the developments in aircraft engineering have made the air travel fast, reliable and affordable. But as the aircraft industry keeps on growing exponentially at a rate of 5% annually, the amount of fuel burnt and greenhouse gasses emitted by the aircraft is growing as well. Therefore there are great challenges remaining for the institutions like TU Delft which I am proud to have been part of, even if just as a masters student, for the last two years. High lift systems, the topic of this thesis, play an important role in making the aircraft more fuel efficient.

To say that I learned a lot during my masters at the TU would be an understatement. Through lectures and many extra curricular events the TU gave me great insight in aerospace engineering, as well as taught me a lot of useful analytical skills. I hope I also gave a small contribution back in the form of this thesis. At this point I would like to thank Leo Veldhuis who, as a chairman of the Flight Performance and Propulsion group, approved my proposal for this project and showed a lot of enthusiasm for it, and Durk Steenhuizen who served as my day to day supervisor and gave me all the necessary feedback. A smooth collaboration with the supervisors allowed me to finish this project in the planned time frame.

The initial idea for the topic of the research came from Gregor Veble of the Pipistrel company, who I would like to thank for giving me this opportunity. Additionally I would like to thank Tine Tomazic, Vid Plevnik and Miha Skof, all of them Pipistrel personnel, who helped me with various technical data and advice.

My study abroad would not have been possible without the scholarship programme of the Slovene Human Resources Development and Scholarship Fund (Javni sklad RS za razvoj kadrov in stipendije), which almost completely funded my study at the TU Delft.

Special thanks goes to Max Baan who offered me to print the hardcopies of the thesis while I was not in Delft, as well as gave me feedback and advice throughout my time in the "Kamertje 1" (including the frequent checking of my screen for any signs of thesis-unrelated websites). I also acknowledge all the other members of the "Kamertje 1" during my stay there for making the atmosphere highly motivational.

I met a lot of people during my stay in The Netherlands, but only few of them I got to know well. One of them is Mustafa Can Karadayi, with whom we spent many hours working together on the assignments as well as discussing countless random topics from physics to society. The others are the fellow Slovenian students in Delft, who made me feel at home on many occasions.

I would also like to thank my parents and my sister for being so genuinely happy during each of my visits at home. The same is true for my grandparents, my aunts and my cousins - I thank them for all of the support not only during my study in Delft but in general. And a very special thanks goes to my girlfriend, Amelija, because of her trust in me and in our relationship while I was away.

Dino Florjancic
Delft, August 2015

ABSTRACT

Relatively high wing loading leads to increase in fuel efficiency in commercial as well as in small general aviation aircraft, but requires sophisticated high lift devices to keep the take-off and landing distances within acceptable limits. High lift devices can in turn have a detrimental effect on cruise performance, and thus fuel efficiency, in the form of additional parasitic drag of the high lift system mechanism fairings under the wing. In addition, the weight and complexity of the high lift system increases with its performance. The purpose of this research is to increase the payload of a highly efficient propeller driven 4-seater general aviation aircraft by improving its plain flap high lift system while the range stays the same. Therefore a detailed design of the high lift system is required, as well as the evaluation of the overall aircraft performance.

A study of existing high lift systems in general aviation aircraft is conducted, based on which a preliminary design decision to implement a single-slotted flap with a dropped hinge mechanism is made. An optimization loop is developed within which the flap geometry is generated based on nine design variables (including the position of the hinge point and the flap deflection angle) and the clean configuration airfoil shape. Two-dimensional aerodynamic analysis of the two-element airfoil section is performed by the MSES code at three different angles of attack. A method of reading the maximum value of displacement thickness on the flap upper surface is implemented to algorithmically detect separated flow and discard the flap designs that suffer from separation at low angles of attack in order to avoid jumps in the lift curve. Three-dimensional aerodynamic characteristics of the aircraft with deployed flaps are estimated using semi-empirical methods. The drag of the mechanism fairings is also estimated by a semi-empirical method. A simple performance model is used to predict the payload, which represents the objective function of the optimization. Landing and take-off distances are also calculated using the performance equations. Matlab's genetic algorithm and pattern search algorithm are used to perform global and local optimization of the flap geometry.

The resulting single-slotted flap design increase the maximum take-off weight by 13% which results in the increase in payload of 42%. Take-off distance increases by 12.5% and landing distance increases by 16.5%. Maximum sectional lift coefficient is improved by 27% with respect to the original plain flap. The additional cruise drag due to mechanism fairings increases the fuel weight by 3% for the range of 1000 nm. Limiting phenomena in achieving the highest two-dimensional lift coefficient is the bursting of main element's wake, rather than flow separation off the airfoil surface. The method of monitoring the displacement thickness of the flap wake is successful in ensuring that the optimized flap has no jumps in the lift curve.

CONTENTS

List of Notations

Variables

α	angle of attack [°]
δ^*	displacement thickness []
δ_f	Flap deflection angle [°]
η_{pr}	Propeller efficiency []
γ	Climb angle [°]
μ	Tire rolling friction coefficient) []
ρ	Air density [$\frac{kg}{m^3}$]
σ	Normal stress [$\frac{N}{m^2}$]
σ	Shear stress [$\frac{N}{m^2}$]
A	Aspect ratio []
b	Wing span [m]
c	Specific fuel consumption [$\frac{N}{Ws}$]
C_M	Pitching moment coefficient, 3D []
C_m	Pitching moment coefficient, 2D []
C_p	Pressure coefficient []
C_{D0}	Profile drag coefficient, 3D []
C_D	Drag coefficient, 3D []
C_d	Drag coefficient, 2D []
C_L	Lift coefficient, 3D []
C_l	Lift coefficient, 2D []
F	Force [N]
F_{act}	Actuator force [N]
g	Gravitational acceleration [$\frac{m}{s^2}$]
g	gap between airfoil elements []
h_{TR}	Altitude after transition [m]
K_A	Aerodynamic coefficient in take-off and landing distance equations []
K_T	Thrust coefficient in take-off and landing distance equations []
M	Moment [Nm]
m	Mass [kg]
MAC	Mean aerodynamic chord [m]
$MTOM$	Maximum take-off mass [kg]
$MTOW$	Maximum take-off weight [N]

n	Load factor []
o	overlap between airfoil elements []
R	Range [nm], radius of transition path [m]
S	Wing area [m^2]
s_C	Climbing distance [m]
s_R	Rotation distance [m]
s_{GR}	Ground roll distance [m]
s_{lan}	Take-off distance [m]
s_{T-O}	Take-off distance [m]
s_{TR}	Transition distance [m]
T	Thrust [N]
t_r	Wing thickness at the root [m]
T_{hin}	Moment about the flap hinge axis [Nm]
V	Velocity []
V_{S0}	Stall speed in landing configuration (full flaps) [$\frac{m}{s}$]
V_{S1}	Stall speed in a given configuration [$\frac{m}{s}$]
W	Weight [N]

Acronyms

CG	Center of gravity
FAR	Federal Aviation Regulations
MSES	Airfoil analysis and design software
NACA	National Advisory Comittee for Aeronautics
RANS	Reynolds averaged Navier Stokes
VSAERO	Three-dimensional panel code software

List of Figures

LIST OF TABLES

1

INTRODUCTION

Modern general aviation aircraft designs tend to have relatively high wing loading in order to decrease aircraft empty weight and fuel burn for the same payload as described in reference [1]. The benefits of higher wing loading come at the expense of low-speed performance. Higher lift coefficients are needed to carry the same weight at the same dynamic pressure on a smaller wing. The main function of a high lift systems is to provide higher lift coefficient in take-off and landing configurations, while affecting the cruise performance as little as possible.

Pipistrel Panthera, a 4-seater propeller driven aircraft, is employed with a plain flap high lift system. The improvement of this system is the subject of the project. The initial objective, as specified by Pipistrel, is:

- Design an improved high lift system for Panthera model that can replace the current plain flap system with no or very little changes to the current wing structure. The aerodynamic shape of the wing in cruise condition may not change. The goal of the improved high lift system is to increase the payload by keeping the stall speed with full flaps the same. Cruise speed and range should also stay the same. The effect on field performance should be identified.

From the initial task given by Pipistrel, the research question is formed as follows:

- What is the optimal high lift system design for a highly efficient 4 seater general aviation aircraft for improved payload?

Figure 1.1 shows the Panthera wing planform and airfoil cross section in clean configuration with plain flap installed. The newly designed flap must preserve the same clean configuration aerodynamic shape, may not extend further than the rear spar position (approximately at $0.7c$) and must keep the same span and spanwise position.

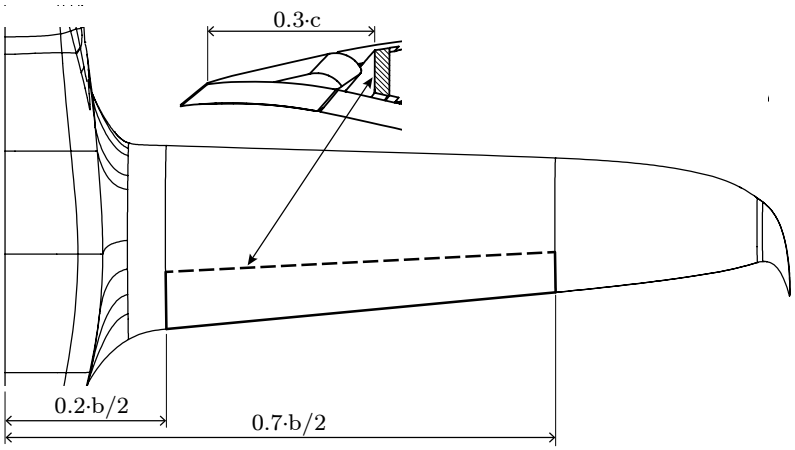

Figure 1.1: Panthera wing planform and airfoil section with plain flap.

Reference [2] from 1974 provides results of an optimization of a slotted flap for a general aviation airfoil and reference [3] presents a project of upgrading a plain flap system on a small propeller driven aircraft. The present work includes an overall aircraft performance model in the optimization loop, taking into account the drag of the flap mechanism fairings and increases in weights of fuel, wing and landing gear as the $MTOW$ increases due to improved high lift system. The optimization also integrates the flap mechanism design parameters to define the position of the flap.

Masters theses from Faculty of Aerospace Engineering at TU Delft of Zaccai [4], Bertels [5], Moerland [6], van den Berg [7] and Hoogendijk [8] all cover different aspects of high lift systems. The main difference of the present project is that its objective is to design a high lift system in detail for the specified application, rather than provide a conceptual or preliminary design tool. The second difference is that it deals with general aviation aircraft, while the existing theses were mainly considering the transport aircraft.

The present thesis report begins with a brief summary of the reviewed literature on high lift aerodynamics (section 2.1), flap mechanisms (section 2.3) and high lift systems in use on small general aviation aircraft (section 2.2). The literature review forms an integral part of the design process since, together with a preliminary performance study, it provides enough information for preliminary design decisions (section 2.4).

Chapter 3 presents in detail the methods used in the optimization process that forms the main part of the project. In brief, the methodology is divided into performance model (section 3.1), two-dimensional aerodynamics (section 3.2), three-dimensional aerodynamics (section 3.3), mechanism design (section 3.4) and weight estimation (section 3.5). The optimization process as a whole is presented in section 3.6. Section 3.7 presents the actual aircraft data used in the optimization runs.

Finally, the results are presented and discussed in chapter 4, which also includes the conclusions and recommendations for future work.

Figure 1.2: Pipistrel Panthera.

NOTE: Some parts of the original thesis report are removed from the public version due to confidentiality reasons. This includes parts of the figures and in some cases complete subsections.

2

LITERATURE REVIEW

In this chapter, a short summary of the reviewed literature relevant to the project is presented. First, the aerodynamic considerations regarding high lift design are discussed (section 2.1). Next, Pipistrel Panthera's competitors and their high lift systems are analysed (section 2.2). Flap mechanisms follow (section 2.3) before the literature review is concluded with a section on preliminary design decisions that can be made from the finding of the literature review (section 2.4).

2.1. AERODYNAMIC CONSIDERATIONS IN THE DESIGN OF HIGH LIFT SYSTEMS

Aerodynamic aspects of airfoil design for high lift are discussed in this section. The theory of obtaining maximum possible C_l of an airfoil is described first (subsection 2.1.1) and afterwards some types of high lift devices are introduced (subsection 2.1.2). In addition, see appendix A.5 for some unconventional types.

2.1.1. HIGH LIFT THEORY

The present section is a brief review of the two papers presented in 70's by then McDonnell Douglas Corporation aerodynamicists Robert H. Liebeck [9] and A.M.O. Smith [10]. They both try to explain the theoretical grounds for achieving maximum possible lift of a single or multi-element airfoil.

Reference [10] explains that the maximum two-dimensional lift coefficient of a potential flow about a cylinder is 4π. Such flow has two stagnation points that move closer to each other with increasing circulation, see figure 2.1. Maximum circulation and thus lift is obtained when they coincide. Lift coefficient of 4π is a much higher value than what has practically been achieved. Typical maximum lift coefficient of a single airfoil used in aircraft wings is about 1.5 [11]. Real flow is not potential, but viscous, rotational and compressible, which causes the overestimation of maximum lift coefficient in potential flow theory.

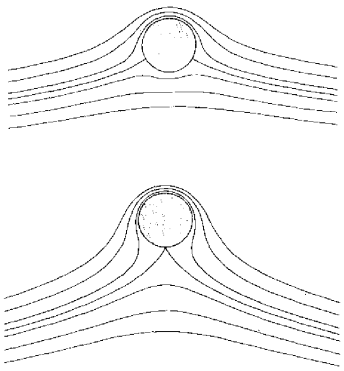

Figure 2.1: Potential flow about a cylinder (from [10]).

Viscous flow in the boundary layer separates from the airfoil surface if it experiences too large adverse pressure gradients. Separation usually represents the maximum lift limit. Reference [9] analyses pressure distributions about an airfoil that would produce highest lift for a given Reynolds number. For this to be achieved, boundary layer on the upper surface must be as close to separation as possible. Liebeck uses the Stratford pressure distribution [12] as a limiting pressure recovery curve that the boundary layer is going to cope with without separation. The shape of this curve for a given Reynolds number and pressure coefficient at trailing edge (for single airfoil a Cp of 0.2 is a good approximation) depends on the start of flow decceleration, see figure 2.2. In figure 2.2, flow is assumed laminar up to the start of decceleration and turbulent from there on. This is the ideal case since the boundary

layer thickness is lower for laminar flow, while turbulent flow is less prone to separation [12]. It is thus possible to find the pressure distribution that gives maximum area under the $Cp(x)$ curve which means maximum lift.

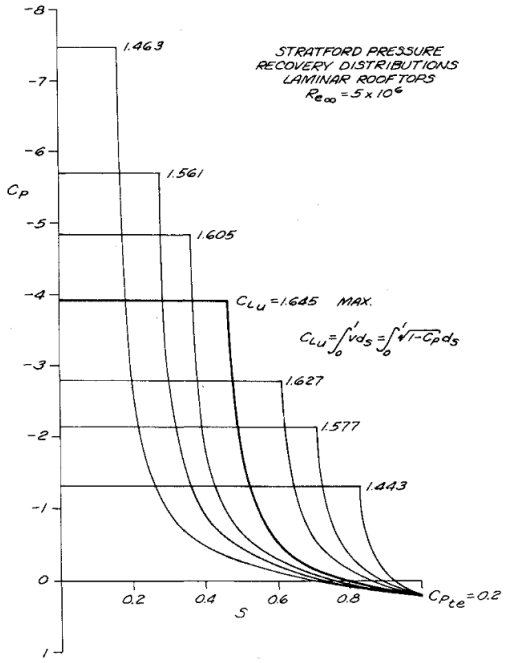

Figure 2.2: Limiting Stratford pressure distributions. Flow is laminar up to the start of decceleration and turbulent from this point on (from [9]).

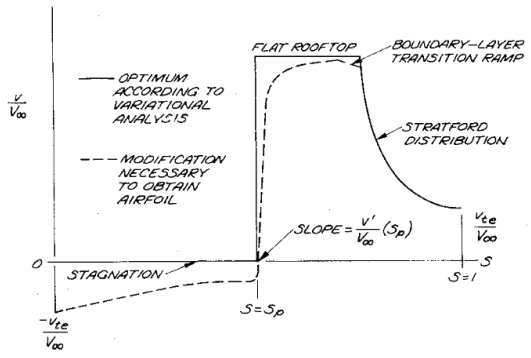

Figure 2.3: Ideal and realistic approximation of the pressure distribution on the airfoil (from [9]).

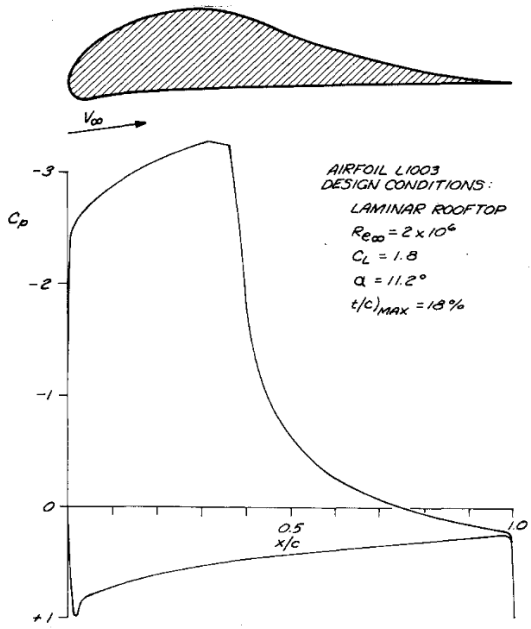

Figure 2.4: L1003 airfoil and its pressure distribution at the angle of attack for maximum lift (from [9]).

On the lower surface, the flow should be as slow as possible to further increase the area between the upper and

lower surface $Cp(x)$ curves. Ideally, the flow on the lower surface would be stagnating throughout the chord. This is not possible in practice as it would mean discontinuities in the flow. Liebeck therefore smoothens the pressure distribution (figure 2.3) and, using an inverse method (for an example of such a method see reference [13]), designs an airfoil that closely matches the desired pressure distribution, figure 2.4. The L1003 airfoil has a maximum lift coefficient of 1.8. Even higher lift coefficient is achieved with the airfoil in figure 2.5 that has a fairly similar upper surface to the L1003 airfoil, but a much more cambered lower surface.

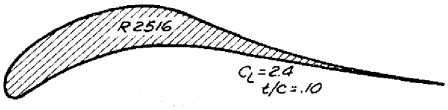

Figure 2.5: R2516 airfoil (from [9])

By inspecting the pressure distribution in figure 2.4, we observe that there is large area on the right hand side of the upper surface pressure recovery curve that is out of reach. If we delay the start of pressure recovery (for the same pressure peak), the boundary layer will not have enough space to slow down to the trailing edge velocity without separation. This is where multi-element airfoils come into play.

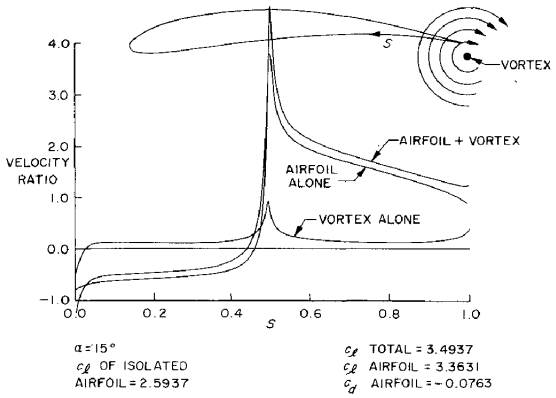

Figure 2.6: The effect of aft airfoil on the trailing edge velocity of the front airfoil (from [10])

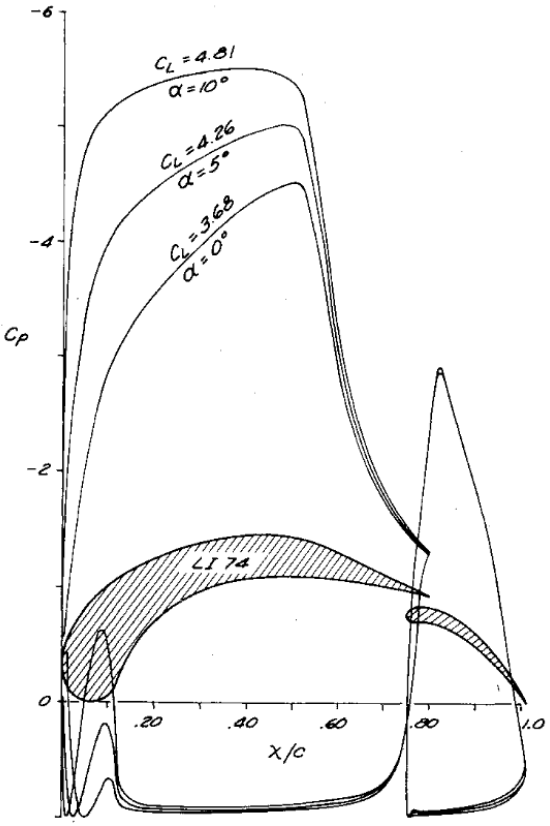

Figure 2.7: Pressure distribution of the L174 two-element airfoil (from [9])

Smith [10] explains the interaction of two closely positioned airfoils by replacing one of them with a vortex that has the same circulation as the replaced airfoil. The effect of the airfoil at the rear on the airfoil at the front is that the circulation from the aft airfoil increases the trailing edge velocity of the front airfoil, see figure 2.6. Consequently the flow on the front airfoil does not need to slow that much, which will allow a later start of the decceleration and a larger area under its $Cp(x)$ curve. On the other hand the flow over the aft airfoil starts with a fresh boundary layer that can again sustain the limiting Stratford pressure recovery. This way a larger area under the $Cp(x)$ curve is obtained with two airfoils then with a single one. Figure 2.7 shows an

example where the Cp at the trailing edge of the front airfoil is as low as -1.3.

Expanding this philosophy it is clear that adding another element or more elements will increase the maximum lift coefficient, which has been proven in practice. The question is, what is the optimum number of elements and what should be their respective chord lengths. Liebeck [9] suggests that the flow over the first element should be accelerated to the point where local Mach number is just below critical, making the optimum design dependent on the freestream Mach number. Chord length of the first element and the design of additional elements should then be adjusted to gradually decrease the trailing edge velocities of the following elements without separation.

2.1.2. TYPES OF HIGH LIFT DEVICES

Single and multi-element airfoils described in subsection 2.1.1 have relatively high maximum lift coefficients. However, they cannot be used for aircraft wings as they cannot offer the desired cruise performance because of their relatively high drag coefficients even at low angles of attack. High lift airfoils used in practical applications in aircraft wings have always been derived from the initial cruise shape via rotating or extending one or more parts of the section from cruise position into the high lift position. Figure 2.8a shows typical high lift configurations in use.

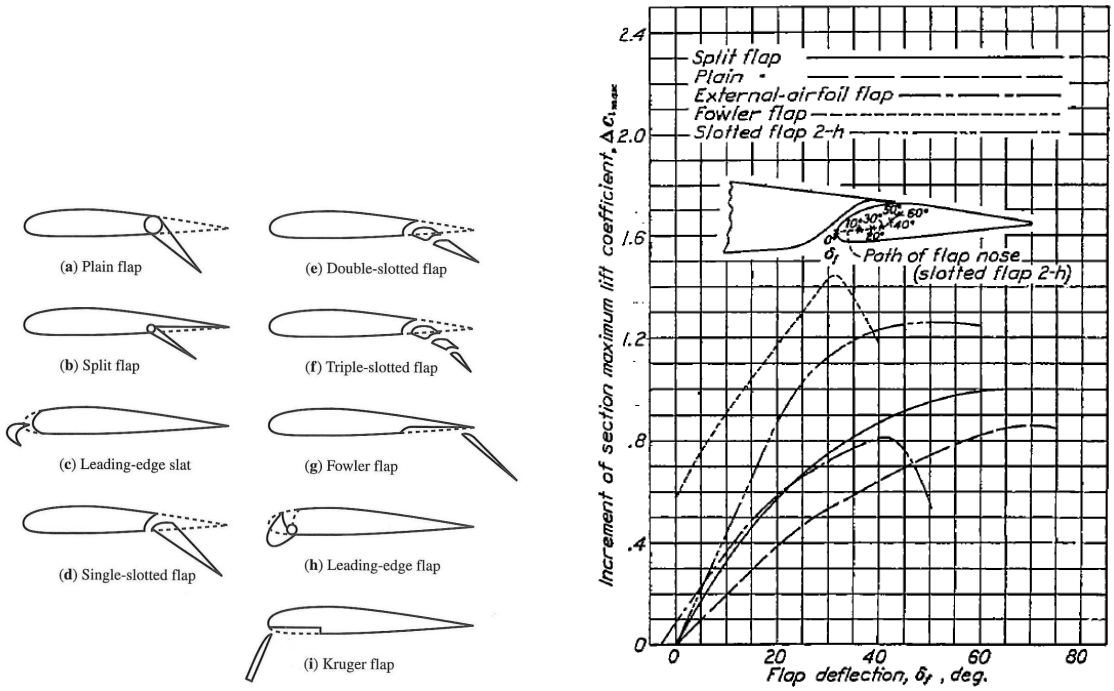

(a) **(b)**

Figure 2.8: a) typical high lift devices in use (from [11]), b) $C_{l_{max}}$ with respect to δ_f for various trailing-edge high lift devices (from [14]).

It is common for larger passenger aircraft to incorporate leading- and trailing-edge devices. A comprehensive review of high lift systems used in commercial airliners is available in reference [15]. Aircraft designed in 1960's feature the highest number of elements in their high lift configuration, the prime example being the Boeing 747 with variable camber Krueger flap at the leading edge and triple slotted trailing edge flaps. In newer designs, manufacturers are trying to achieve similar high lift performance with much simpler solutions to decrease weight and cost [15]. Two most recent airliners, Airbus A350 and Boeing 787, only use leading-edge slats and single-slotted trailing-edge flaps.

In light general aviation aircraft the improved performance of complex high lift systems does not outweigh their cost and weight. There are virtually no aircraft in this category employed with leading-edge devices (see section 2.2). Trailing edge devices vary between plain flaps and single-slotted or Fowler flaps. These

devices are explained in more detail in the remainder of this subsection. Table 2.1 sums the approximate high lift performance of wing sections employed with typical trailing-edge high lift devices. Figure 2.8b show $C_{l_{max}}(\delta_f)$ curves for some examples from reference [14].

Airfoil only	1.4-1.5
Plain flap	+0.9
Split flap	+1.0
Slotted flap	+1.3
Fowler flap	+1.3 c'/c

Table 2.1: Increments of $C_{l_{max}}$ for different types of trailing edge high lift devices w.r.t. clean airfoil (from [16], [11])

Plain flap

Plain flap is one of the simplest high lift devices. It operates as a moving aft part of the airfoil and is widely used as a control device in form of ailerons, elevators and rudders. The main difference is that in case of a high lift device, the flap deflections are much higher than in case of a control device. A simply hinged plain flap is shown in figure 2.9.

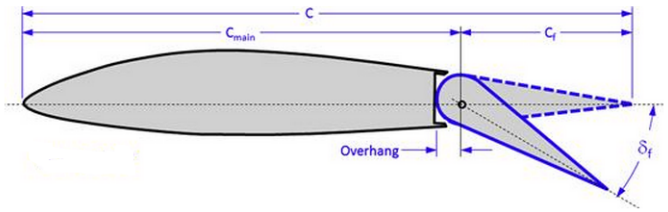

Figure 2.9: Simply hinged plain flap (from [17])

Reference [18] presents wind-tunnel data for numerous airfoils equipped with plain flaps of different chord lengths. The highest lift coefficient found in the report is 2.4, measured on a NACA23013 airfoil with a c_f/c of 0.2 at a flap deflection of about 70° at a Reynolds number of $3.5x10^6$. Such a high flap deflection is not unusual for maximum lift coefficient of airfoils with plain flaps. Figure 2.10 compares maximum lift coefficient of different airfoils with varying flap chord lenghts. It indicates that the optimal c_f/c is about 0.2-0.25. Figure 2.11 shows the effect of flap size on drag polar with lift to drag ratio increasing with c_f/c from 0.1 to 0.3, mainly at higher lift coefficients.

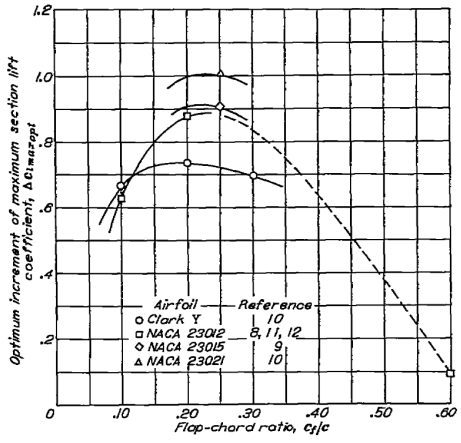

Figure 2.10: Optimal c_f/c ratios for different airfoils (from [18])

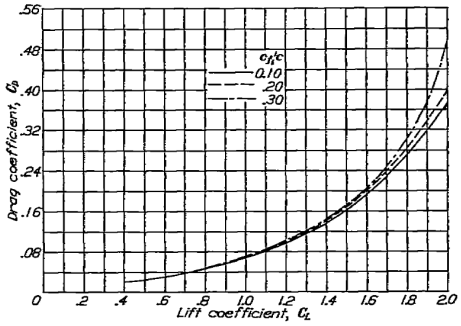

Figure 2.11: Drag polars for plain flaps of different c_f/c ratios (from [18])

Split flap

Split flap, figure 2.12, is another relatively simple device that increases the maximum lift coefficient of the airfoil. Literature on aircraft design (e.g. refereces [11], [16]) state that split flaps are considered an obsolete design because of a high drag coefficient, especially at take-off lift coefficients, in comparison with plain flaps. However, wind tunnel test data from NACA experiments in 1930's indicates that the drag of a split flap is not higher than the drag of the plain flap at low lift coefficients, while at higher lift coefficients the split flap even has lower drag than a plain flap. Those experiments were conducted at a Reynolds number of $3.5x10^6$.

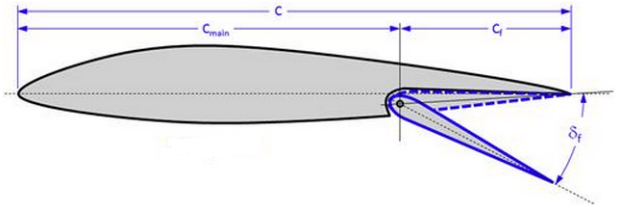

Figure 2.12: Split flap (from [17]).

The disadvantage of split flaps are the vibrational loads on the flap because of a large portion of separated flow downstream of the flap that can be unsteady.

Slotted flap and Fowler flap

Pure Fowler motion of the flap means that the flap only translates rearward, extending the effective chord. A slotted flap will in practice almost always have both a Fowler motion and an angular motion. On the other hand it is possible to have a system with Fowler motion and no gap. Some flap mechanisms initially provide predominantly Fowler motion for use during take-off and climb while at larger flap extraction higher angular deflection is provided for use during approach and landing.

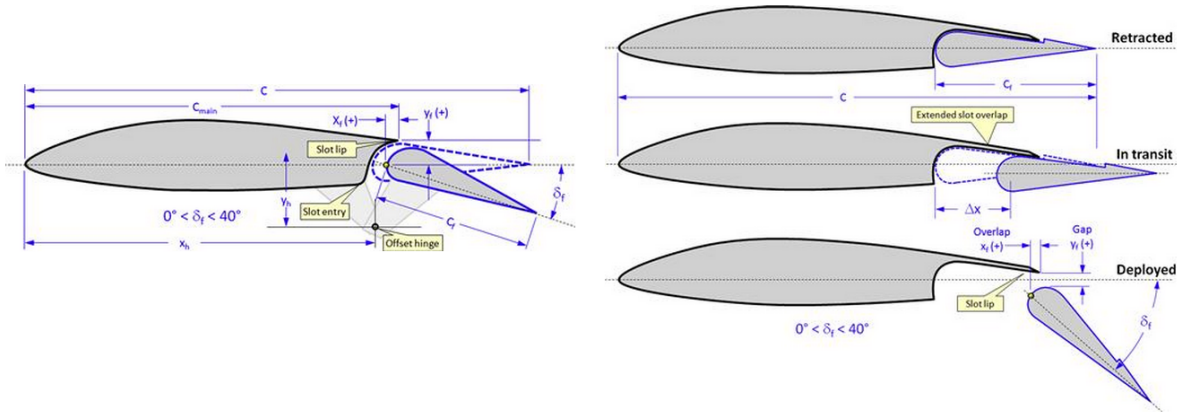

Figure 2.13: Slotted flap (left) and Fowler flap (right) (from [17]).

As noted in section 2.1.1, slotted airfoils have potential to reach higher lift coefficients then single-element airfoils. Reference [18] gives a brief review of wind tunnel test results of various airfoil-flap combinations. Values of maximum lift coefficient of up to 3.45 are reported. When comparing this values with plain or split flaps, it is important to recognise that C_l values are based on the clean airfoil chord length, i.e. with flap retracted. Therefore some increase in lift coefficient comes purely from extending the effective chord. For better comparison it is useful to look at the C_l based on the extended chord.

Reference [14] gives detailed experimental results on flap shape and position optimization. There is relatively small chord extension at low flap deflections, but at higher deflections, where maximum lift is measured, effective chord is even shortened. Maximum lift coefficient measured is 2.8, which is 0.4 more than for a plain flap. This is the common lift increment of a slotted flap without Fowler motion reported in aircraft design books, such as references [11] and [16].

Position of the flap relative to the main airfoil is critical when designing for maximum lift. Reference [10]

explains that the circulation effect of the flap on the dumping velocity of the main airfoil is decreasing with increasing gap. But too small a gap blocks the required airflow through it. This is due to the thickness of the boundary layer, which is Reynolds number dependent, therefore the design of multi-element airfoils is very Reynolds number specific. References [19] and [20] describe dependencies of high lift aerodynamics on Reynolds number on the basis of large-scale wind tunnel tests needed for the design of commercial airliners. This data was very scarce until nineties, but for the purpose of the general aviation 4-seater category aircraft the data at Reynolds numbers of about $2x10^6$ is already sufficient and some of it has been obtained already in 1930's.

Reference	[14]	[2]	[21]
Type	Slotted flap, no Fowler	Fowler flap	Fowler flap + slat
Year	1939	1974	1991
Clean airfoil	NACA 23012	GA(W)-1	MD 30P30N
C_{lmax}	2.8	3.8	4.6
Re	$3.5x10^6$	$2.2x10^6$	$9x10^6$
Flap deflection	50°	40°	35°
Gap	1.3%c	2.7%c	1.8%c
Overlap	0.8%c	-0.7%c	0%c

Table 2.2: Flap position optimization results from three different studies.

Wind tunnel optimization of flap position relative to the main airfoil was conducted in references [14], [2] and [21], table 2.2 sums up the results. Note the difference in configurations and Reynolds number. We can conclude that a gap of 2%c and overlap of 0%c would be good starting points for the initial design, but the final optimal position will depend on the actual geometry and Reynolds number. Figure 2.14 shows a typical plot of a flap position optimization study that shows contours of constant lift coefficients. It can be seen that the optimum space is relatively small and therefore the positioning of the flap is crucial for successful design. Furthermore, the optimal position of the flap for maximum lift-to-drag ratio is usually different to the optimal position for maximum lift.

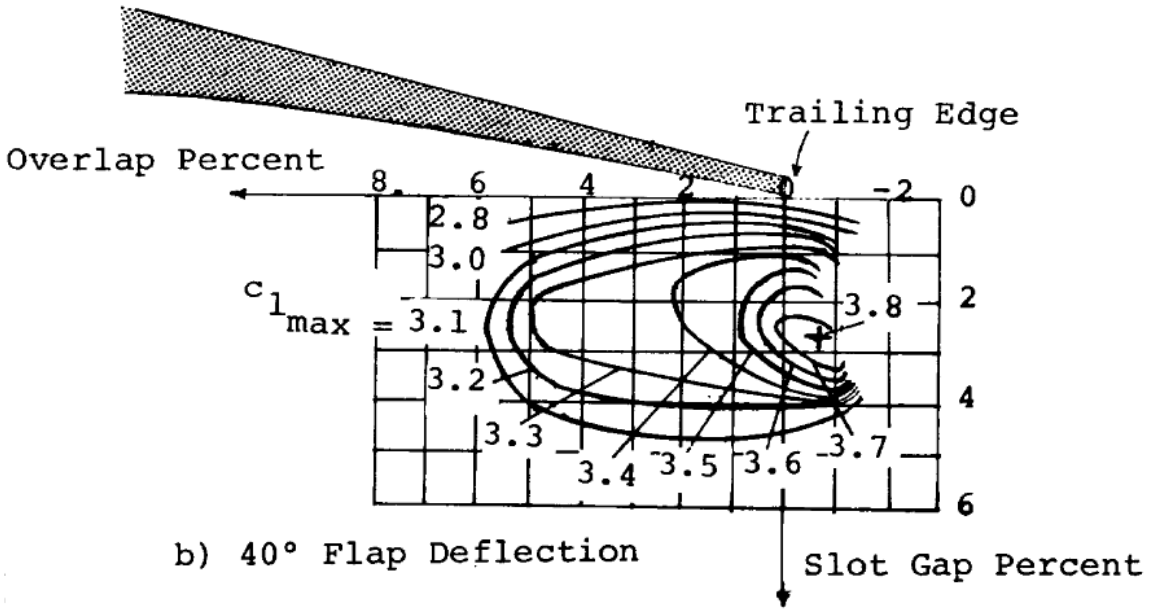

Figure 2.14: Constant C_l contours for different flap positions (from [2])

2.1.3. STALL HYSTERESIS

Another phenomena related to the flow through the slots is hysteresis. When the stall occurs, it is important that the flow reattaches after as minimal decrease in angle of attack as possible. Some configurations show problematic hysteresis, where the angle of attack needs to be dramatically reduced, in some cases to negative angles, in order for the flow to reattach. The phenomenon is not well understood and there is a lack of computational methods to predict it. References [22] and [23] investigate the issue on the basis of wind tunnel tests.

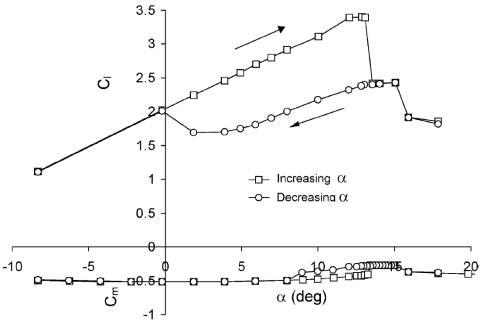

Figure 2.15: Example of stall hysteresis as seen on the lift curve (from [22]).

Figure 2.15 shows the difference in lift curves when the angle of attack is increasing up to stall and then decreasing back. References [22] and [23] state the bursting of a laminar separation bubble on the flap upper surface as one of the main causes of hysteresis and also show no signs of hysteresis when the flow over the flap is fully turbulent due to forced early transition. Since the hysteresis is not possible to predict with a steady aerodynamic analysis, forced transition on the flap could be a solution if a configuration is found to suffer from hysteresis in the wind tunnel tests after the design has been completed.

2.2. COMPETITION ANALYSIS

An analysis of Pipistrel Panthera's competitors or aircraft of similar configuration, size and price was conducted. This is to compare the current Panthera design to similar aircraft and possibly identify the desired increase in performance of the improved design. Some design and performance data of these aircraft is available in the table 2.3 at the end of this section and some of the airrcaft are discussed in more detail in the following subsections.

2.2.1. DIAMOND DA40 XLT

DA40 is a high aspect ratio composite aircraft. It is equipped with plain flaps. At the wing root, small portion of the bottom surface of the flap extends further inboard, adding a small split flap (see figure 2.16). Plain flap cannot be extended this far inboard because of the fuselage over the wing, but the bottom side still offers space for the split flap. This way some additional lift is obtained. Although plain flaps are inferior to the slotted flaps in producing high lift, the DA40 has the highest certified lift coefficient of all compared aircraft, see table 2.3.

Figure 2.16: Plain flap of the Diamond DA40 with visible split flap at the wing root. [24]

2.2.2. CESSNA 172 AND 182

Cessna 172 and 182 models feature the same wing planform and high lift systems. The latter is a slotted flap type with a fairly long Fowler motion (Beechcraft Bonanza is another example of this type of flaps). Pictures of the flap are shown in figures 2.17 to 2.19. Motion is provided by track mechanism, tracks being simply cut out of a plate. Motion is driven by a pushrod mounted to the flap leading edge (figure 2.19) between the two tracks. Fowler motion development with deflection of the flap is linear throughout its travel. Maximum flap deflection is 30°. Older 182 models used to have a maximum deflection of 40°. Stall speed of the 182 reported in table 2.3 holds for the older models with higher flap deflections. According to [25] flap deflection was limited to lower angle due to too steep approach angles making it difficult for pilots to flare and touch down.

Advantage of the plate tracks is that they do not stick out of the wing in clean configuration. With this mechanism Cessna has achieved a relatively large Fowler motion with virtually no drag penalty in cruise. The downside of plate tracks is that such mechanism is overconstrained if the flap is tapered and conical motion is needed. Plate tracks are also more difficult to maintain and more prone to freeplay issues.

Figure 2.17: Cessna 172 flap in a deflected position with visible slot. [26]

Figure 2.18: Close-up of plate tracks. [27]

Figure 2.19: Pushrod for flap actuation. [27]

Figure 2.20: SR22 with visible dropped hinges under the wing. [28]

Figure 2.21: SR22 flap with a dropped hinge bracket. [29]

2.2.3. CIRRUS SR20 AND SR22

SR20 and SR22 have the same wings, SR22 having higher payload and stronger engine. They feature slotted flaps actuated via a dropped hinge mechanism (Piper PA28 and Cessna TTx). As can be seen in figure 2.20, the mechanism sticks out of the wing, causing some parasite drag. Advantage of this mechanism is that it is the simplest way to open the slot between the main airfoil and the flap.

2.2.4. CESSNA TTX

The TTx is the only airplane in table 2.3 that is faster than Panthera. In contrast to Cessnas 172 and 182, it is equipped with dropped hinge mechanisms that actuate the slotted flaps (see figure 2.22). The hinges are shorter than on the SR22 and longer than on the PA28. The TTx has four hinges under each wing, while the SR20, SR22 and PA28 have three.

Figure 2.22: Cessna TTx with four dropped hinges on each wing. [30]

Reference		[31]	[30]	[30]	[30]	[32]	[33]	[33]	[34]	[35]
		Panthera 260 HP	Cessna 172S Skyhawk	Cessna 182 Turbo Skylane JT-A	Cessna TTx	Diamond DA-40 XLT	Cirrus SR22	Cirrus SR20	Piper PA Cherokee Archer	Beechraft Bonanza
Year of introduction		2014	1956	1956	2004	1998	2001	1999	1960	1947
MTOM	[kg]	1315	1157	1406	1633	1199	1633	1386	1157	1656
Wing area	[m2]	11.2	16.2	16	13	13.5	13.5	13.71	16	16.8
Wing loading	[kg/m2]	117.4	71.4	87.9	125.6	88.8	121	101.1	72.3	98.6
Wing span	[m]	10.86	11	10.97	10.97	12	11.68	11.68	10.8	10.21
Maximum power	[hp]	260	180	227	310	180	310	200	180	300
Stall speed	[KIAS]	60	47	49	60	49	60	56	46	NA
Take-off distance (50 ft)	[m]	540	497	422	579	518	535	451	490	583
Climb rate	[fpm]	1550	730	1000	1400	1120	1270	828	667	1230
Landing distance	[m]	570	407	411	805	638	714	803	442	NA
Cruise speed	[KTAS]	198	124	156	235	150	183	155	128	176
Range	[nm]	1000	518	1360	1229	720	1050	625	522	852
Service ceiling	[ft]	24900	14000	20000	NA	16400	17500	17500	14100	18500
Useful payload	[kg]	500	415	462	454	390	607	421	395	469
Empty mass (calc.)	[kg]	815	742	944	1179	809	1026	965	762	1187
Fuel volume (full)	[l]	210	212	360	386	190	348	221	182	273
Fuel mass ()	[kg]	155	156	265	284	140	256	163	134	201
Payload after fuel (calc.)	[kg]	345	259	197	170	250	351	258	261	268
C_L @ stall speed (calc.)	[]	1.97	1.96	2.21	2.11	2.24	2.03	1.95	2.07	NA
C_L @ cruise speed (calc.)	[]	0.18	0.28	0.22	0.14	0.24	0.22	0.25	0.27	NA
Flap type		Plain flap	Slotted flap	Slotted flap	Slotted flap	Plain flap	Slotted flap	Slotted flap	Slotted flap	Slotted flap
Mechanism type		Simple hinge	Plate tracks	Plate tracks	Dropped hinge	Simple hinge	Dropped hinge	Dropped hinge	Dropped hinge	Plate tracks

Table 2.3: Light general aviation aircaft comparison. Some parameters are calculated approximately from the available data. C_L is calculated from the data on stall (and cruise) speed and wing area.

2.3. FLAP MECHANISMS

In comparison to the current plain flap system on Pipistrel Panthera, there are several possible improvements from the aerodynamic point of view, as seen in section 2.1. It is the mechanical side that limits the design space because the desired movement of the flap relative to the main wing calls for a mechanism that is in some cases large and heavy enough to make a certain design option not viable. It is therefore of great importance to compare different mechanisms that are in use. In this section, kinematic characteristics of flap mechanisms are discussed first (subsection 2.3.1), before some types of the mechanisms are described in more detail (subsection 2.3.2).

2.3.1. KINEMATICS OF FLAP MECHANISMS

Before discussing kinematic properties of flap mechanisms, it is necessary to define the parameters that are important for aerodynamic performance of a high lift system, namely the Fowler motion, flap deflection, gap and overlap (figure 2.23). Overlap is positive when the leading edge of the flap is in front of the trailing edge of the main element, i.e. when the elements are overlapping. It is negative when they are not overlapping and is in such case a chordwise distance between them. Gap is the minimum distance between the elements. *WRP* in figure 2.23 stands for "wing reference plane" from which the flap deflection is measured.

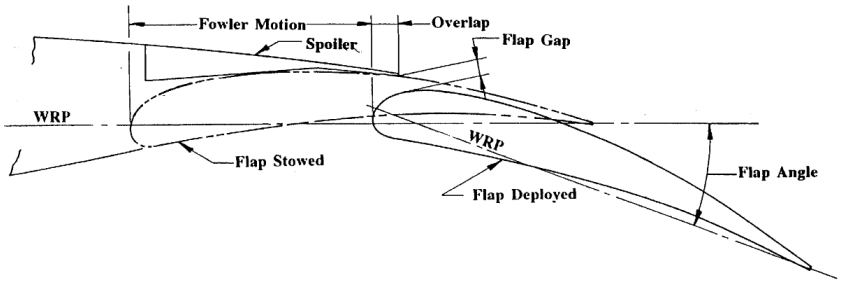

Figure 2.23: Definition of kinematic parameters (from [36])

From an aerodynamic point of view it is desirable to initially have Fowler motion with little flap deflection for take-off. For landing, higher deflection is needed with minimal Fowler motion. Mechanisms that better satisfy these requirements tend to be more complex than the ones that have less satisfying kinematics.

Figure 2.23 from [36] shows Fowler motion development depending on angular deflection for several mechanisms used in commercial airliners. Despite the dropped hinge mechanism having the worst Fowler motion development curve, the two most recently designed commercial airliners, Airbus A350 and Boeing 787, make use of the dropped hinge mechanism for their single-slotted trailing edge flaps. They additionally use spoilers and cove doors to control the gap [4], but it is clear that the aircraft industry is moving towards simpler mechanical solutions in order to reduce part count and weight.

In case of a tapered flap, the three-dimensional motion is ideally conical, so that the flap extends for the same percentage of the chord all along its length. The outboard edge therefore needs to rotate about a smaller radius than the inboard edge, see figure 2.24.

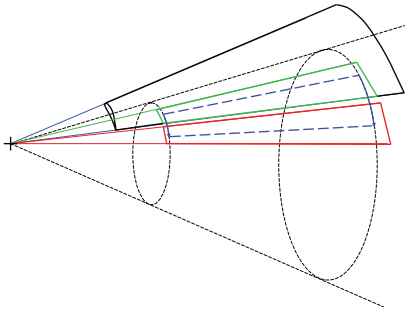

Figure 2.24: Conical motion of the flap on a tapered (and in this case also swept) wing (from [37]).

2.3.2. TYPES OF FLAP MECHANISMS

Mechanisms in use in general aviation aircraft are mainly simple hinge (plain flap), dropped hinge and plate tracks.

Simple hinge and dropped hinge

The term *simple hinge* is used when the hinge line of the flap is within the flap itself, usually close to the leading edge of the flap. Such mechanism is currently used on the Panthera aircraft. In case of a dropped

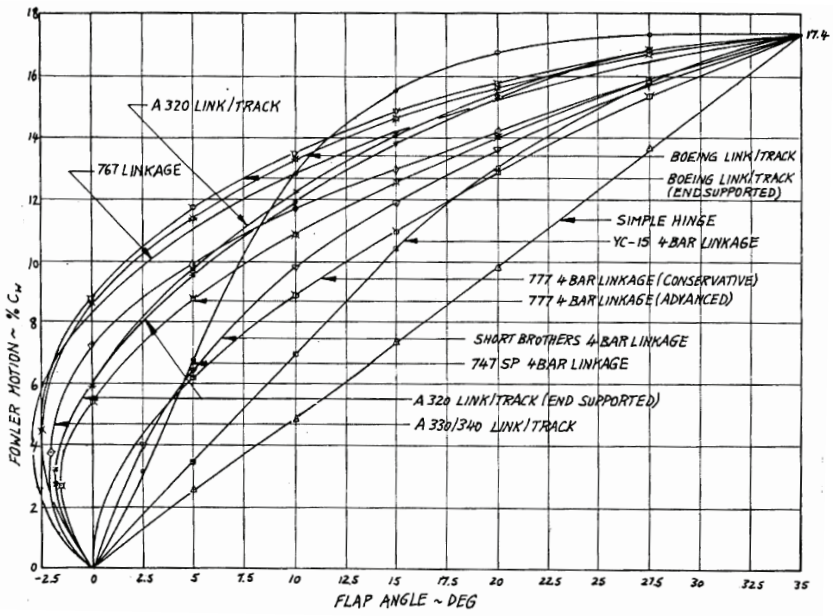

Figure 2.25: Fowler motion versus flap deflection angle for different mechanisms (from [36])

hinge, the hinge line is below the wing bottom surface. Figure 2.26 shows a detailed drawing of a dropped hinge mechanism of the Cirrus SR20. Only the inboard hinge is shown (port wing). Conical motion is possible with a dropped hinge mechanism by simply angling the hinge axis (closer to the flap at the outboard edge than at the inboard edge).

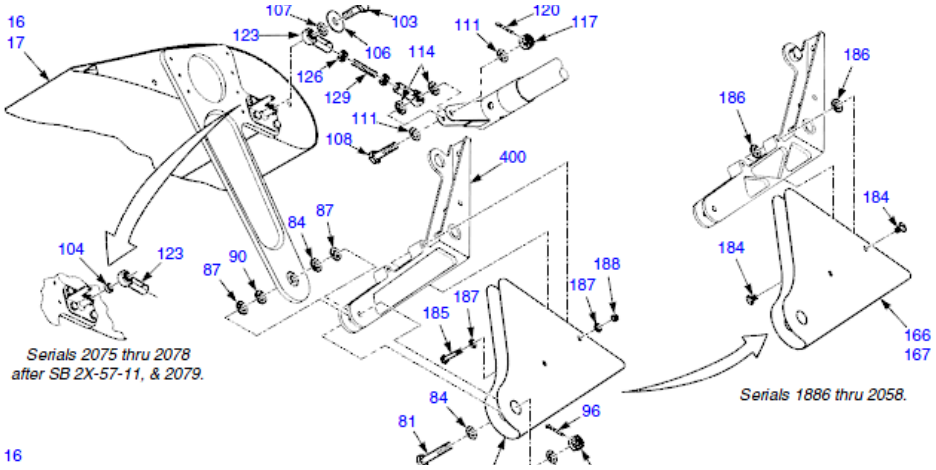

Figure 2.26: Drawing of the Cirrus SR20 dropped hinge mechanism (from [38]).

Plate tracks

Beechcraft Bonanza (figure 2.27a) and Cessnas 172 and 182 feature prime examples of plate track mechanisms. Plate tracks are an attractive option because they are almost fully enclosed in the wing, but still offer Fowler motion similar to a dropped hinge. However, if the flap is tapered and conical motion is desired, the plate tracks overconstrain the mechanism and none of the modern light general aviation aircraft discussed in section 2.2 uses plate tracks.

Four bar linkage

Although not used in light general aviation aircraft, the four bar linkage mechanism is worth considering since it could be mounted on a support of similar size to the dropped hinge support. An example of a well

packaged mechanism is in figure 2.27b. This is a Boeing 747SP mechanism that is completely enclosed by the flap, as the flap itself is not a cusped one. Blue link in figure 2.27b is the ground link. Red link is the drive link. Flap is mounted on the yellow link and the green link completes the mechanism.

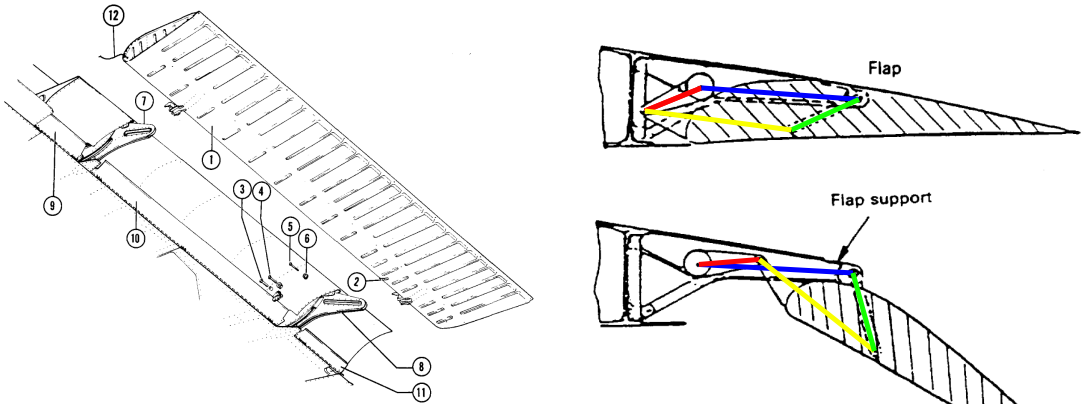

Figure 2.27: a) flap tracks of Beechcraft Bonanza (from [39]), b) Boeing 747SP four bar linkage (from [15]).

2.3.3. ACTUATION SYSTEMS

FAR 23 regulations allow different actuators for left and right flaps, but the certification process is much more straightforward if both flaps are mechanically connected and only one actuator is used. The flaps can be actuated in the midspan of the flap (see figure 2.19), which requires more linkages, or at the inboard hinge like in figure 2.26 (the tube in the center at the top of the figure is connected to the actuator seen in figure 2.28, note the other end of the tube at the left of this figure).

Typical actuators in use are electromechanical linear actuators (figure 2.28). Electric motor is used as a driving element that is connected to a screw drive via a gearbox. The screw drive translated the rotational motion into linear movement of the pushrod. According to reference [40] the weight of the linear actuators varies between 2 kg and 4 kg for the range of maximum loads from 1000 N to 6000 N, which is normally required in light general aviation aircraft.

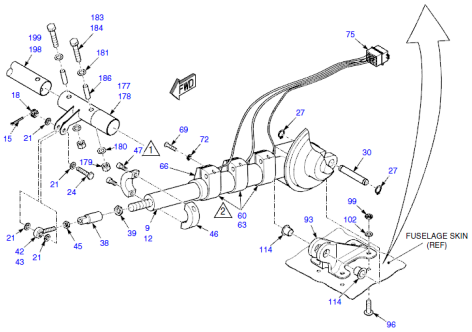

Figure 2.28: Electromechanical linear actuator from Cirrus SR20 (from [38]).

2.4. PRELIMINARY DESIGN

After the review of the literature and existing light general aviation aircraft, some design decisions could be made in order to narrow down the options and start with a detailed design. Looking at table 2.3, there is no clear connection between the type of the high lift system and the $C_{L_{max}}$, since the highest $C_{L_{max}}$ is calculated for the DA40, which features a plain flap. Only the Cirrus SR22 has a marginally higher payload than the Panthera, but it also has more than 300 kg higher $MTOM$.

A preliminary performance analysis was conducted, with the increase in C_L as an input, to investigate the effect of increased C_L on the overall performance of the aircraft. The drag of the mechanism fairings was also only approximated for this analysis. The detailed assumptions of the analysis are listed below.

- It was assumed that single-slotted flaps are fitted to the aircraft instead of plain flaps.
- $\Delta C_{L,max}$ (full flaps) of up to 0.25 was considered, in steps of 0.05. According to table 2.3, this would bring Panthera's C_L on top of the competition.

- Stall speed with full flaps (landing configuration), V_{S0}, was kept constant, while $MTOW$ was increased in each step according to the increase in $C_{L_{max}}$
- Stall speed in take-off configuration, V_{S1}, was kept constant.
- Initial values for C_L and C_D were obtained from drag polar data at the ground run angle of attack.
- In each step, ΔC_L in ground run was increased for the same amount as in full flap configuration.
- C_D in ground run was kept constant for all steps.
- L/D in take-off climb was kept constant for all steps.
- C_{D0} in cruise configuration was increased gradually each step to account for fairing drag of the improved high lift system, so that it reached 1.7% of initial cruise drag in the last step (see section 3.4.3 for the estimation of fairing drag). It was increasing proportionally to $\sqrt{\frac{\Delta C_{Lmax}}{max(\Delta C_{Lmax})}}$.
- Ratio between cruise velocity and velocity for best range (best L/D) was kept constant for all steps.
- Range was kept constant for all steps.
- Reserve fuel was assumed constant for all steps. Therefore observed increase in fuel weight was only due to increased fuel consumption during cruise for specified range, whereas in reality also the reserve fuel weight would increase.
- Aircraft structural weight was increased each step due to increase in wing weight and landing gear weight.
- Increase in wing weight was estimated according to the method from appendix C in reference [41], see also section 3.5.1.
- Increase in landing gear weight was estimated according to chapter 8 of reference [41], see also section 3.5.2.
- Weight of the high lift system was assumed constant.
- Changes in trim condition were not taken into account.

The results of this study are summarized in table 2.4, where the values $MTOW$ and $W_{payload}$ before the increase in $C_{L_{max}}$ are denoted with subscript 0. The most important conclusion of the study is that an increase in $C_{L_{max}}$ of 0.25 increases the payload by 34.5%, as the increases in the weights of fuel, wing and landing gear are much smaller than the increase in $MTOW$.

$\Delta C_{L_{max}}$	0.25
$\Delta MTOW / MTOW_0$	12%
$\Delta W_{payload} / W_{payload_0}$	34.5%
$\Delta W_{payload} / \Delta MTOW$	79.3%
$\Delta W_{fuel} / \Delta MTOW$	10.4%
$\Delta W_{wing} / \Delta MTOW$	5.7%
$\Delta W_{lan.gear} / \Delta MTOW$	4.6%

Table 2.4: Results of preliminary performance analysis.

The method described in section 3.3.1 suggests that to achieve an increase in $C_{L_{max}}$ of 0.25, an increase in two-dimensional $C_{l_{max}}$ of the airfoil should be at least 0.5. To achieve such an improvement compared to the plain flap, the literature review on high lift system types suggests that a slotted flap is necessary.

An interesting concept of a slotted flap with the rotation axis inside the flap, effectively making it a slotted plain flap, was analysed in reference [42]. Figure 2.29 shows the flap in both retracted and deployed position. In the deployed position, the flow has to turn rather abruptly in order to flow through the gap. Reference [42] states that provides the results of a two-dimensional RANS computations that suggest an increase in $C_{l_{max}}$ of about 0.4 with respect to the plain flap. Although this is a promising result, considering that no external

mechanism is needed, the flap suffers from separation at lower angles of attack, which results in a non-linear lift curve and also increases the chance of stall hysteresis (see section 2.1.3).

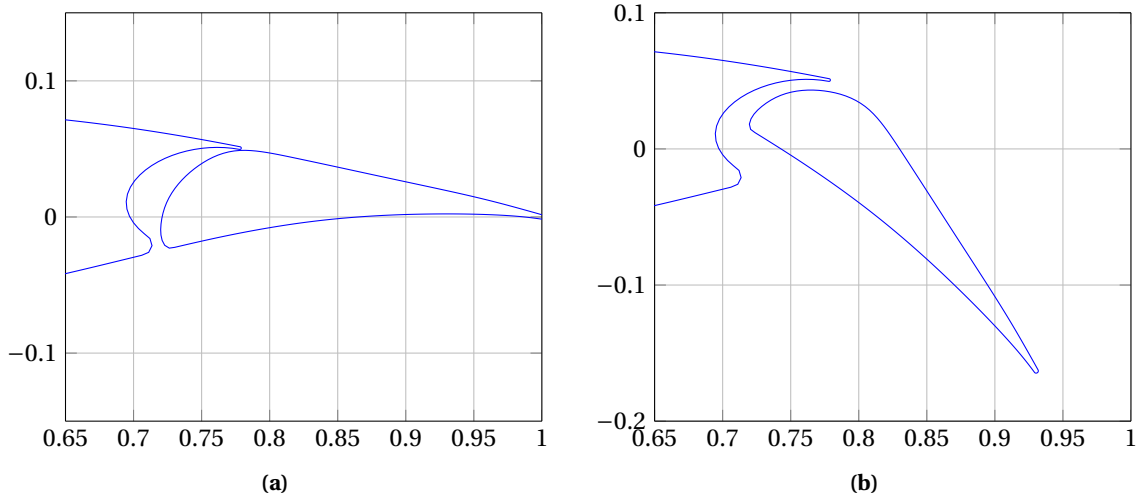

Figure 2.29: Slotted plain flap in clean (a) and deployed (b) configuration (from [42]).

From the findings of the preliminary performance analysis it was decided that a single-slotted flap with a dropped hinge mechanism would be the best option to meet the project objectives. Slotted flap is necessary to achieve a substantial increase in payload over the plain flap. Dropped hinge has a disadvantage of the fairing drag compared to the plate tracks and four-bar linkage, but is best suited for the conical motion that is necessary because of the tapered flap. Dropped hinge is also the most common mechanism for slotted flaps used in modern light general aviation aircraft.

Three supports per flap are necessary, as in the case of Cirrus SR20 and SR22 that have similar wings to Panthera's. The flap will be actuated at the inner hinge, again similar to the Cirrus, since there is little space in the wing to house linkages for actuation at the midspan of the flap. See appendix A.7 for the sketch of the actuation mechanism.

3

METHODOLOGY

In this chapter all the methods that were used during the design process are described in detail. Performance model is presented first (section 3.1), followed by two-dimensional aerodynamic analysis that includes a description of the MSES code and parametrization of the airfoil section (section 3.2). Next, three-dimensional aerodynamic analysis is presented by first introducing the VSAERO code that was used to validate the semi-empirical methods that follow (section 3.3). Before the method for estimating the drag of the flap support fairings, the mechanical sizing of the brackets is described (section 3.4). Estimating the weight of the wing and landing gear is also presented (section 3.5). Finally, the workflow diagrams of the optimization routine are shown (section 3.6). The actual aircraft data is omitted up to the section 3.7, where all the relevant data is presented. Correlation of the methods with the aircraft data is also presented in that section.

3.1. PERFORMANCE MODEL

The goal of the assignment is to increase the useful payload of the airplane by enhancing its high lift performance. Therefore a performance calculation model needs to be established. This model will be used for evaluation of different designs of the high lift system on the full aircraft level. Take-off, landing and cruise performance will be analysed for each design. There are many books on aircraft design and performance that contain similar performance models. The equations of the model used in this project are based on the book of Raymer [16].

There is a certain amount of simplification involved in deriving such equations. The results should still be sufficiently accurate, providing that the various aircraft-specific coefficients are as accurate as possible. Even if the results are slightly off the actual aircraft performance, our intention is to compare different but similar designs. If the model is applied consistently, it should give the desired insight in the impact of design variations.

3.1.1. TAKE-OFF

Part 23 of Federal Aviation Regulations (FAR 23) [43] defines the take-off distance as the ground distance covered from standstill to the point where the aircraft is 50 ft (15.23 m) above the ground. The distance can be computed as a sum of ground roll distance, rotation distance, transition distance and the climbing distance:

$$s_{T-O} = s_{GR} + s_R + s_{TR} + s_C \tag{3.1}$$

Ground roll distance is computed by equation (3.2). For more information on derivation of this expression see reference [16], section 17.8.

$$s_{GR} = \frac{1}{2\,g\,K_A}\, ln\Big(\frac{K_T + K_A V_f^2}{K_T + K_A V_i^2}\Big) \tag{3.2}$$

V_i and V_f are initial and final velocity, respectively. Initial velocity for ground run is 0, while final velocity is the velocity at the start of rotation. According to FAR 23, V_{S1} can be used for this velocity. V_{S1} is the stall speed for a given configuration, in this case with flaps in take-off position and with extended landing gear. Coefficients K_A and K_T in equation (3.2) are defined as:

$$K_T = \frac{T}{W} - \mu \tag{3.3}$$

$$K_A = \frac{\rho}{2\frac{W}{S}}(\mu C_L - C_{D0} - K C_L^2) \tag{3.4}$$

Since equation (3.2) is derived by integrating the inverse of acceleration over V^2, the average thrust needs to be used that is approximated by the thrust at $1/\sqrt{2}\,V_f$, according to [16]. If more detailed thrust data depending on velocity is obtained, the model can be improved.

Tire rolling friction coefficient μ for hard, dry runways is chosen as 0.03, according to [16]. Weight is taken as maximum take-off weight, $MTOW$. Standard atmosphere is assumed, giving the air density of 1.225 kg/m^3. S is the reference wing area. Lift coefficient during ground run is constant and will be obtained by flight-test data, as well as the drag polar (K, C_{D0}).

The duration of rotation is dependent on the pilot, but can be assumed to take 1 second at V_f. Rotation distance is given by equation 3.5. The transition distance is computed from the radius of transition path, R, and the climbing angle, γ, in equation (3.6). If lift is assumed equal to weight during this phase, the climbing angle is given by equation (3.7). Radius R is obtained with equation (3.8), where transition velocity V_{TR} is the average velocity during the transition. Since the aircraft accelerates from V_{S1} to $1.2 \cdot V_{S1}$, the average velocity is then $1.1 \cdot V_{S1}$. This acceleration comes from FAR 23 requirement that the 50 ft obstacle is overflown with the velocity 1.2 times higher than V_{S1}.

$$s_R = 1sec \cdot V_f \tag{3.5}$$

$$s_{TR} = R \cdot sin\gamma \tag{3.6}$$

$$\gamma = \frac{T}{W} - \frac{D}{L} \tag{3.7}$$

$$R = \frac{V_{TR}^2}{g(n-1)} \tag{3.8}$$

$$V_{TR} = 1.1 \cdot V_{S1} \tag{3.9}$$

Load factor n in equation (3.8) is given by equation (3.10), again see reference [16] for more information. Ratio C_L/C_{Lmax} can be taken as 0.9, according to [16]. This is the ratio of the actual lift coefficient during the transition phase and the maximum lift coefficient in take-off configuration.

$$n = \frac{C_L}{C_{Lmax}} \cdot 1.1^2 = 1.089 \tag{3.10}$$

It needs to be checked if the aircraft is already above the 50 ft obstacle during the transition maneuver. The altitude after the transition is given by equation (3.11). If this turns out to be more than 50 ft, the transition distance up to the altitude of 50 ft is computed by equation (3.12). If transition is executed up to the climb phase, the transition distance is then given by (3.13).

$$h_{TR} = R(1 - cos\gamma) \tag{3.11}$$

$$s_{TR50} = \sqrt{R^2 - (R - 50ft)^2} \tag{3.12}$$

$$s_{TR} = R \cdot sin\gamma \tag{3.13}$$

Distance during climb to the altitude of 50 ft is computed by equation (3.14). Now all the terms of equation (3.1) are known and the take-off distance can be computed.

$$s_C = \frac{50ft - h_{TR}}{tan\gamma} \tag{3.14}$$

3.1.2. LANDING

FAR 23 defines the landing distance as the ground distance from the point where the aircraft is 50 ft above the ground to the point where it has stopped to a standstill. The approach angle before the flare maneuver has to be 3° and the approach speed must be at least 1.3 times higher than V_{S0}, which is the stall speed in landing configuration: flaps fully extended, landing gear deployed, idle thrust.

For the calculation of approach distance, flare distance and ground roll distance the same equations as for take-off can be used with appropriate modifications in mind. Raymer [16] suggests a touch down velocity V_{TD} to be 1.15 times V_{S0}, giving the average flaring velocity V_{fl} of 1.23 times V_{S0}, and the load factor during landing to be 1.2. Tire rolling friction coefficient due to deployed brakes during ground run can be taken as approximately 10 times higher than during take-off.

3.1.3. CRUISE

Cruise performance will also be affected because of the changes in the high lift system. When $MTOW$ is increased due to enhanced high lift performance, the lift needed for steady, level flight needs to increase. Consequently, the induced drag will be higher, demanding more thrust for the same cruise speed. Flap mechanism fairings might also cause additional drag that will similarly affect cruise performance. Additionally, the new high lift system might affect the weight of the airframe in three ways. First, the system itself can change its weight during the design process. Second, increased $MTOW$ will cause the wing structure to become heavier to withstand higher loads. Third, landing gear weight will also increase due to higher loads during landing.

The constraint of the design process is to keep the range constant, thus the fuel needed for the same range will increase for higher MTOW. Only after the calculation of cruise performance the conclusion can be made about the increase in payload due to improved high lift system.

For calculation of cruise performance it will be assumed that lift coefficient and cruising velocity are constant throughout the cruise, meaning that the aircraft needs to climb to higher altitude to reduce dynamic pressure for the equations to be valid [16]. Thrust required for cruise at the desired velocity is calculated from thrust to weight ratio by equation (3.15). Alternatively, if total drag coefficient in cruise condition is known instead of C_D and K, equation (3.16) is used.

$$\frac{T}{W} = \frac{\frac{1}{2}\rho V^2 C_{D0}}{\frac{W}{S}} + \frac{W}{S}\frac{K}{\frac{1}{2}\rho V^2} \tag{3.15}$$

$$T = \frac{1}{2}\rho V_{cruise}^2 C_{D,cruise} S \tag{3.16}$$

Fuel needed for the given range is computed from the Breguet range equation for propeller driven aircraft:

$$R = \frac{\eta_{pr}}{c}\frac{L}{D} ln\frac{W_i}{W_f} \tag{3.17}$$

In equation (3.17), c is specific fuel consumption of the engine and W_i and W_f are initial and final aircraft weight, respectively. Initial weight is the $MTOW$, while final weight is decreased for the amount of fuel burnt. Payload, which is the main parameter to be optimized during the design process, is computed by equation (3.18), where W_{struct} is the weight of the aircraft without fuel and payload.

$$W_{payload} = MTOW - W_{struct} - (W_i - W_f) \tag{3.18}$$

3.2. TWO-DIMENSIONAL AERODYNAMIC ANALYSIS

Airfoil analysis and design is the core activity of the high lift system design. In this section the airfoil geometry parametrization and the MSES code are described.

3.2.1. AIRFOIL PARAMETRIZATION

In order to generate different airfoil geometries within an optimization scheme, the airfoil was parametrized as shown in figures 3.1 and 3.2a. With flap retracted ($\delta_f = 0°$), the airfoil must keep the prescribed cruise shape that was fixed before the design of the new flap. The reference airfoil for all calculations was the one at 49% of the semispan of the aircraft's wing, representing approximately the midspan of the flap. The nose of the flap was formed by fitting a b-spline between points C_1 (top flap break) and C_2 (bottom flap break), see figure 3.2a. Hinge point position was controlled by parameters HP_X and HP_Y. The minimum thickness of the trailing edges of the main element was taken into account, hence the difference in distances between the flap breaks $(C_1 - C_2)$ and between the actual trailing edges of the main element $(C_1 - C_2)_{eff}$, see figure 3.2a. The final geometry is obtained by rotating the flap by the angle δ_f about the hinge point, with gap and overlap being the resulting and not the controlling parameters, see figure 3.3. All the parameters are summarized and described in detail in table 3.1. The cove shape for MSES calculation was simplified by fitting an arc between the main element trailing edges as shown in figure 3.2b by the black curve.

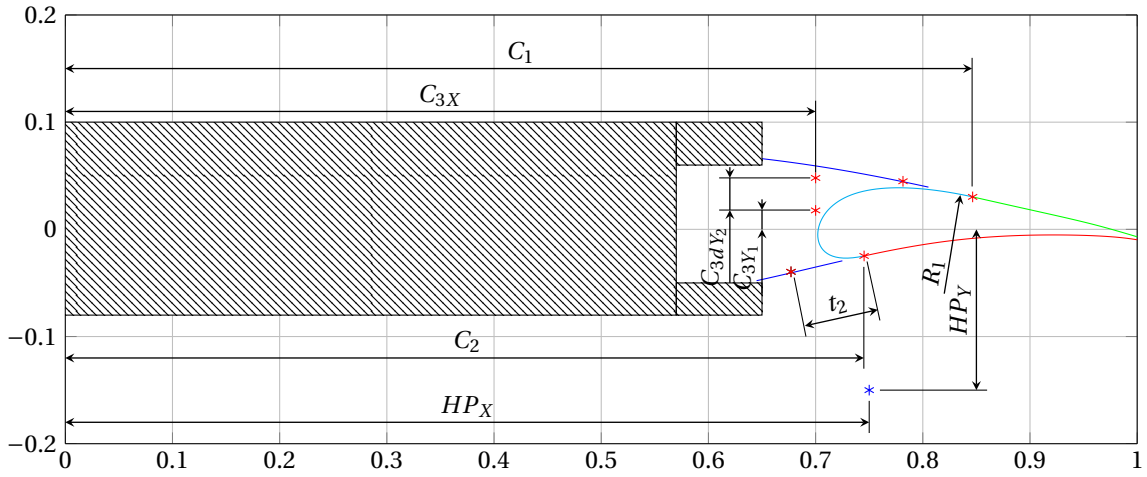

Figure 3.1: Exemplary flap defined by the clean airfoil (blue, green and red curves) and a b-spline (cyan curve) with 6 control points (red asterisks). The blue asterisk is the hinge point. Part of the airfoil masked due to NDA.

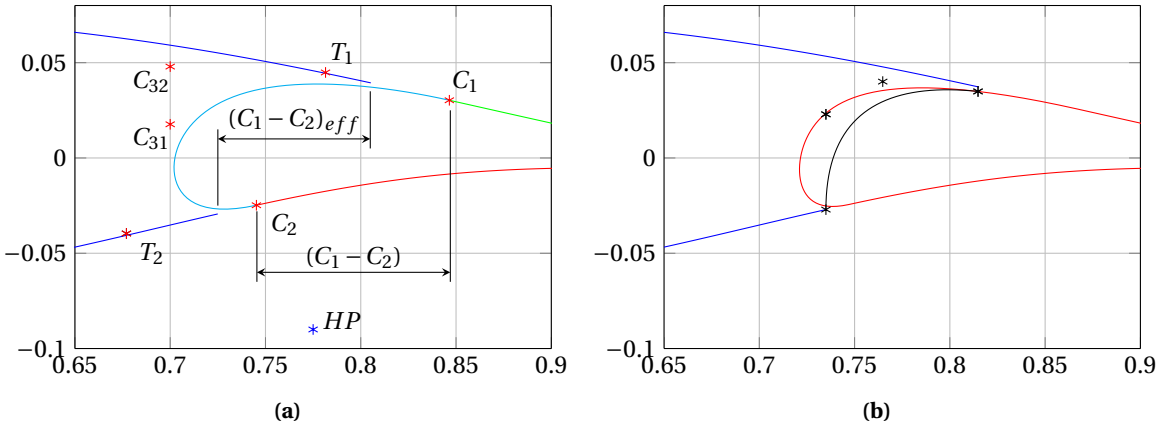

Figure 3.2: a) names of the control points and b) simplified cove shape for MSES runs.

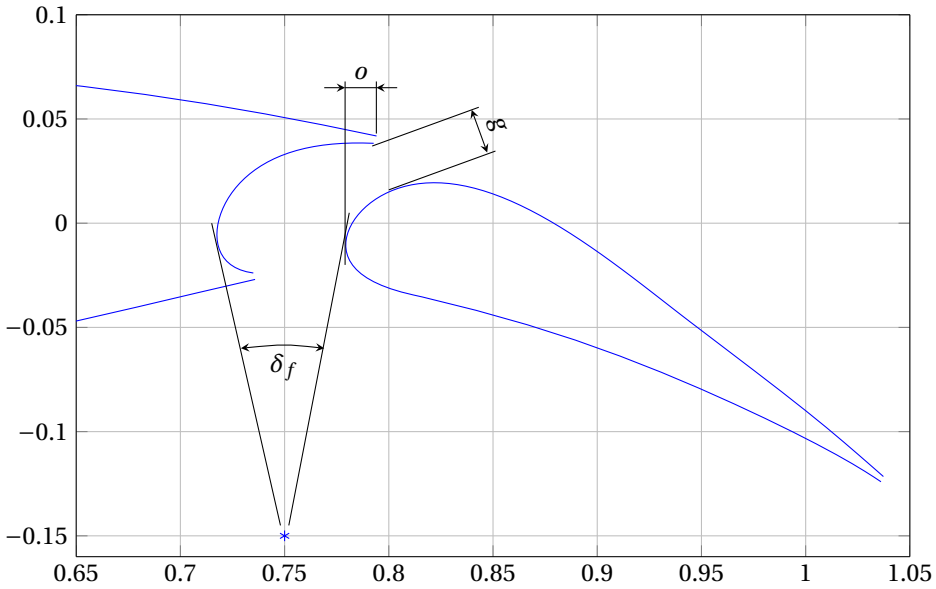

Figure 3.3: Definition of flap deflection angle (δ_f), gap (g) and overlap (o).

Parameter	Description	Type
$C_1 - C_2$	distance in x-direction between the top flap break (C_1) and the bottom flap break (C_2) (see figure 3.2a)	design variable
C_2	x-coordinate of the bottom flap break (C_2)	design variable
dR_1	increment in radius of the b-spline at the C_1 point, defines distance to the next control point (T_1)	design variable
t_2	distance from the bottom flap break (C_2) to the next control point (T_2) lying on the line tangential to the flap surface at C_2 point	design variable
C_{3Y_1}	y-coordinate of C_{31} point, x-coordinate fixed at C_{3x}	design variable
C_{3dY_2}	vertical distance from point C_{31} to point C_{32}	design variable
HP_Y	y-coordinate of the hinge point	design variable
dHP_X	decrement of HP_X applied after the most aft x-coordinate is calculated at which the flap can be deployed without clashing into the wing	design variable
δ_f	flap deployment angle	design variable
HP_X	x-coordinate of the hinge point	consequence of design variables
$(C_1 - C_2)_{eff}$	effective distance in x-direction between the trailing edges of the main element (see figure 3.2a)	consequence of design variables
R_1	radius of the b-spline at the top flap break (C_1) defined as $R_1 = R_{1_0} + dR_1$, where R_{1_0} was set to 0.1	consequence of design variables
g	gap	consequence of design variables
o	overlap	consequence of design variables
C_{3X}	x-coordinate of C_{31} and C_{32} points	constant

Table 3.1: Airfoil geometry parameters.

3.2.2. MSES - AIRFOIL ANALYSIS AND DESIGN SOFTWARE

MSES code [44], developed by Mark Drela, was chosen as the tool for two-dimensional aerodynamic analysis. It is a coupled inviscid-viscous code. For inviscid flow, the Euler equations are used, while viscous flow is

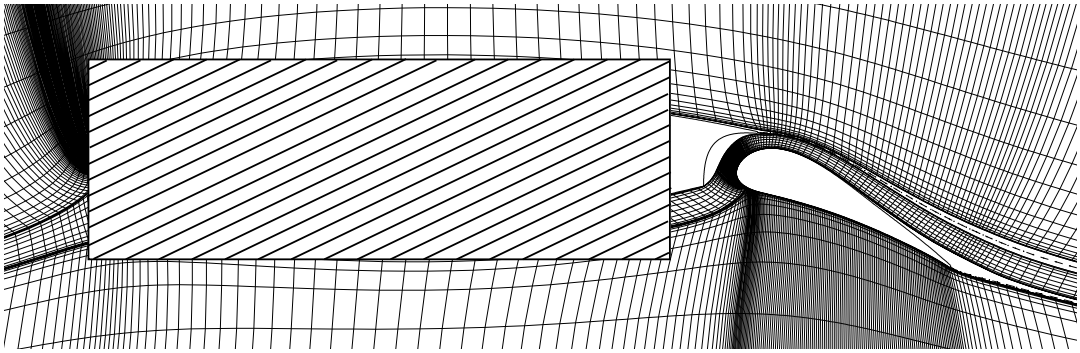

Figure 3.4: MSES grid about a two-element airfoil. Blank layers adjacent to the airfoil surface represent the boundary layer. Larger regions indicate seprated flow. In the wakes, the top and bottom surface boundary layers are merged. Part of the airfoil masked due to NDA.

solved for the boundary layers using the two-dimensional integral boundary layer equations. The grid on which the Euler equations are solved is formed automatically by intersecting the inviscid flow streamlines and curves emitting from the airfoil surface points (figure 3.4). The streamlines themselves are precomputed with a panel method. The number of streamlines and airfoil points to be used for grid generation is set by the user, as well as the outer boundaries of the grid. Contrary to many inviscid-viscous codes, the MSES does not iterate between the inviscid and viscous solutions, but rather couples both set of equations into a single non-linear system of equations that is then solved by the Newton-Raphson iterative method. Inviscid grid and boundary layer equations are coupled with the displacement of the streamline adjacent to the airfoil surface by the displacement thickness δ^*.

The reasons why MSES was chosen as the tool for the task of optimizing the two-element airfoil are:

- automatic meshing and short computation time;
- it is run from the terminal and can be fully automated with simple scripts;
- literature [44] [45] shows good correlation with wind tunnel tests at $C_{l_{max}}$ and it is also used by other authors for high lift analysis [46];
- higher fidelity codes such as three-dimensional RANS solvers offer no guarantees for better $C_{L_{max}}$ prediction [47] while demanding much longer meshing and solver time;
- it is available as an open source code for research purposes.

Although reference [44] provides promising validation data of the MSES code, reference [45] finds larger errors in prediction of maximum lift coefficient of two-element airfoils. Therefore some additional comparison with wind tunnel data has been performed as a part of this project in order to provide more insight in MSES accuracy. Grid density and size were also determined according to test runs and documentation.

Figure 3.5 shows a grid density study for a GA(W) airfoil with a single slotted flap from reference [2] at an angle of attack for maximum lift. Very little influence of the number of grid points on the airfoil surface can be seen between 90 and 130 points. At least 100 points per airfoil side were used in all runs within the optimization scheme.

Absolute grid size analysis is provided in MSES documentation and shows fairly low sensitivity to absolute grid size. This is because of the vortex + doublet farfield representation. The absolute grid size setting was left at default value computed by MSET (grid generation code for MSES). This resulted in an approximate value of parameter r/c of 2.75, with r defined in equation (3.19). A in equation (3.19) is the area of the grid. Such grid size gives an error of about 0.1% in prediction of C_l according to the MSES documentation.

$$r = \frac{\sqrt{A}}{2} \tag{3.19}$$

In order to quantify the error in prediction of aerodynamic coefficients, the MSES results were compared to wind tunnel tests from references [48], [49] and [45]. Table 3.2 summarizes the errors in prediction of

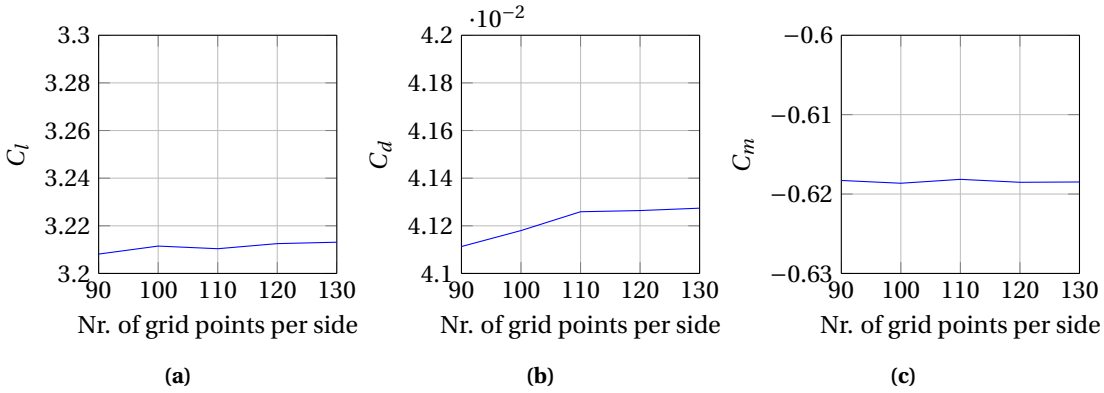

Figure 3.5: MSES grid convergence study for GA(W) airfoil at $\alpha = 8°$ and $\delta_f = 30°$.

lift coefficient both in the linear range and at maximum lift. There is no clear pattern emerging that would indicate that a correction factor could be used as the errors depend heavily on the airfoil geometry.

The error in computing the C_l in the linear range (see table 3.2) is mainly due to the inaccuracies in computing the flow between both elements, also known as the gap flow. This is shown in figure 3.6. The lift curve in the linear range is computed fairly accurately for a single element airfoil (figure 3.6b), while there is an overprediction of C_l for the two-element configuration (figure 3.6a) if the transition is determined by MSES. When transition on the flap is fixed to an earlier location, the lift is decreased. It is possible to find a transition location at which the computed curve matches the experimental curve. All the computed curves in figure 3.6a converge to the same values at $C_{l_{max}}$ because the transition happens very early on the flap leading edge at high angles of attack even if left free. This also explains lower errors in prediction of $C_{l_{max}}$ then in prediction of C_l in the linear range in table 3.2. An error in $C_{l_{max}}$ of about +/- 0.1 (+/- 3.3% for typical values of $C_{l_{max}}$ of about 3.0) for a two-element airfoil can therefore be expected in the design of a new high lift system.

Case	Average difference in C_l in linear range	Difference in $C_{l_{max}}$
NLF-MOD22(A), $\delta_f = 15°$[48]	+0.154	+0.11
NLF-MOD22(A), $\delta_f = 30°$[48]	+0.129	+0.01
NASA airfoil, $\delta_f = 30°$[49]	+0.217	+0.08
NASA airfoil, $\delta_f = 40°$[49]	+0.083	+0.03
WFA [45]	+0.07	-0.07
WFB [45]	+0.213	-0.09

Table 3.2: Summary of MSES C_l prediction in comparison to the wind tunnel tests (positive value is MSES overprediction).

Figure 3.7 shows a summary of C_d prediction. MSES is underpredicting the drag in all cases and the error can be up to 25%. Again no specific correction factor for C_d was implemented since for the aircraft in high lift configuration the profile drag is much lower than the induced drag. More detailed results of MSES validation can be found in appendix A.1, including the prediction of the moment coefficient C_m which was found to have similar errors as the prediction of C_l.

Table 3.3 summarizes the MSES settings used in the design of the high lift system. Reynolds and Mach number correspond to flow conditions at stall speed $VS0$ and at ground level. MSIS, a simplified solver within MSES, was used because it is suggested by the developer for computation of low Mach number cases [50]. The only simplification in MSIS is that the streamwise momentum (along the streamlines) is conserved, which is valid for low Mach number flows without shock waves.

A C-shell script for automating the MSES with the Linux terminal commands is presented in appendix A.6. This script is called by the Matlab optimization scheme to run the MSES.

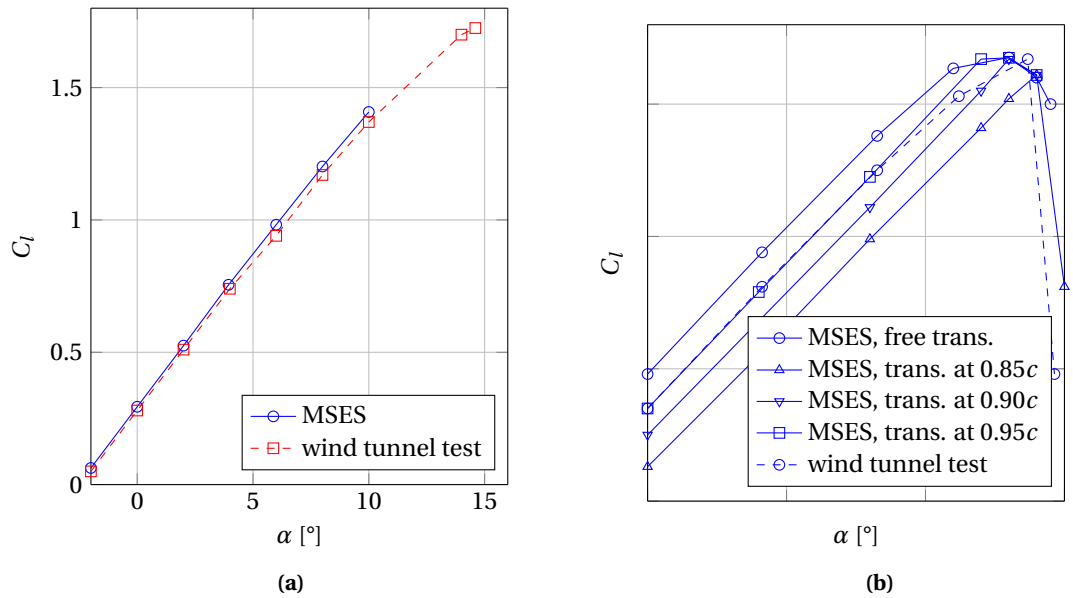

Figure 3.6: MSES validation: a) comparison of lift curves for NLF-MOD22(A) (δ_f = 30°, gap = 0.03c, overlap = 0.01c) with different transition locations (wind tunnel test from [48]), b) comparison of computed and measured lift curves for clean configuration airfoil from reference [49].

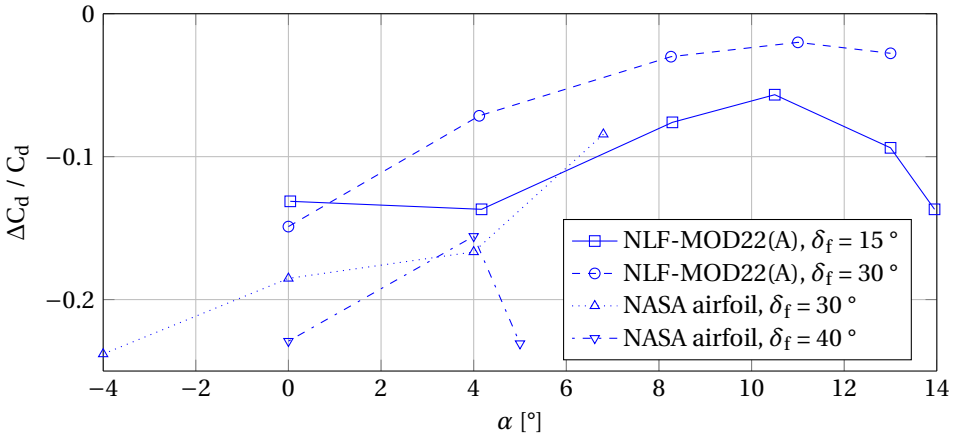

Figure 3.7: Summary of drag prediction errors. Negative values mean MSES underprediction.

Parameter	Value
Reynolds number	2.1e6
Mach number	0.09
Solver	MSIS (isentropic)
r	~ 2.75
Nr. of airfoil points	100 to 130 per side

Table 3.3: Summary of MSES settings used in the design process

3.2.3. A METHOD FOR DETECTION OF SEPARATED FLOW

Besides obtaining a high $C_{L_{max}}$, an important design objective for the new flap is also to avoid flow separation at lower angles of attack. This is due to two reasons:

- separated flow at low angles of attack, usually off the flap surface, and reattachment at higher angles of attack cause a jump in the lift curve which can be problematic for the pilot during landing maneuvers;
- separated flow over the flap increases the chance of hysteresis in the lift curve [23].

Separation over the flap at low angles of attack is a common problem in two-element high lift airfoils, because the high pressure peak on the leading edge of the flap is not suppressed enough until the downwash of the main element increases at higher angles of attack [20].

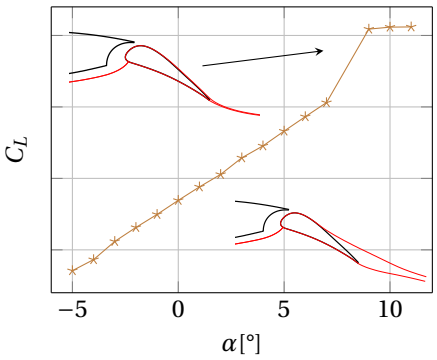

Figure 3.8: An exemplary lift curve with a jump between $\alpha = 7°$ and $\alpha = 9°$.

To keep computation time of the optimization (section 3.6) within feasible limits, it is not possible to evaluate each design throughout the whole angle of attack range. MSES package includes a program for quick computation of the lift curve (MPOLAR), but it often has difficulties converging for the desired range and could not be used reliably within the optimization. Three different angle of attack runs per design can be run with MSES to still achieve reasonable computation time, therefore a method is needed that would ensure attached flow over the whole angle of attack range based on three results.

The method had to detect separation and discard the designs with separated flow at any of the evaluated angles of attack. This was done through reading the value of displacement thickness δ^* in the wake of the flap, as shown in figure 3.9. If the maximum δ^* was higher than the specified limit, the design was discarded. δ^* on the main element could also be taken as a criteria, but separation always happened on the flap.

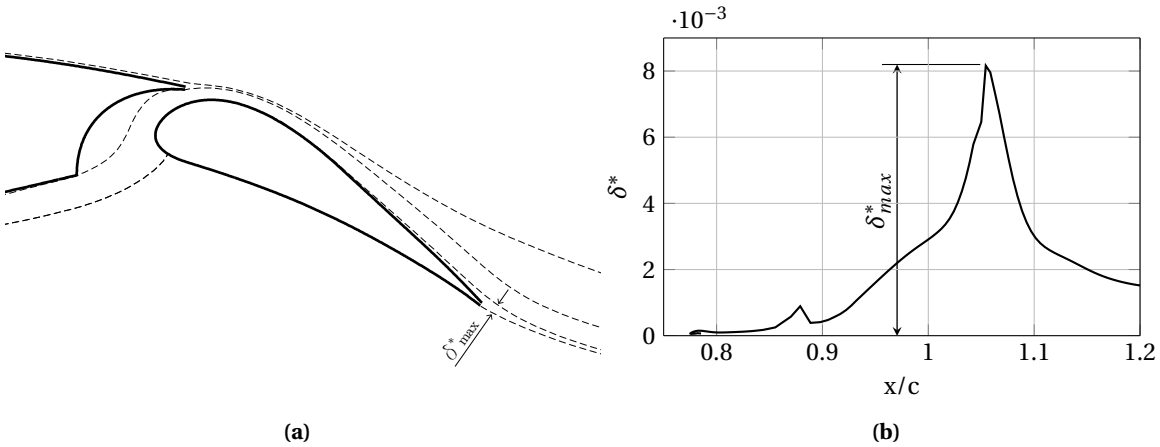

(a) **(b)**

Figure 3.9: Maximum displacement thickness δ^*_{max} of the flap wake.

The value of the δ^* limit had to be chosen appropriately since the flow separation that causes the jump in the lift curve is not clearly defined. Figure 3.10 shows the resulting lift curves of six optimization runs with different δ^* limits. $\delta^*_{max} = 0.02$ was chosen as the limit since the curve in figure 3.10 with this limit has the highest $C_{L_{max}}$ without any regions of increasing slope.

The angles of attack at which designs were evaluated are -5°, 8° and 12°. For the evaluation of $C_{l_{max}}$, the 12° angle of attack was chosen after preliminary runs showed that maximum lift coefficients were achieved at that angle if the flap deflection angle was in the range of 20° to 30°. Designs with higher flap deflection had $C_{l_{max}}$ at lower angle of attack, but were much more prone to separation at lower lift conditions while only offering marginally higher $C_{l_{max}}$ values. For the minimum angle of attack, -5° was chosen as the aircraft is not expected to fly at lower angles of attack with deployed flaps.

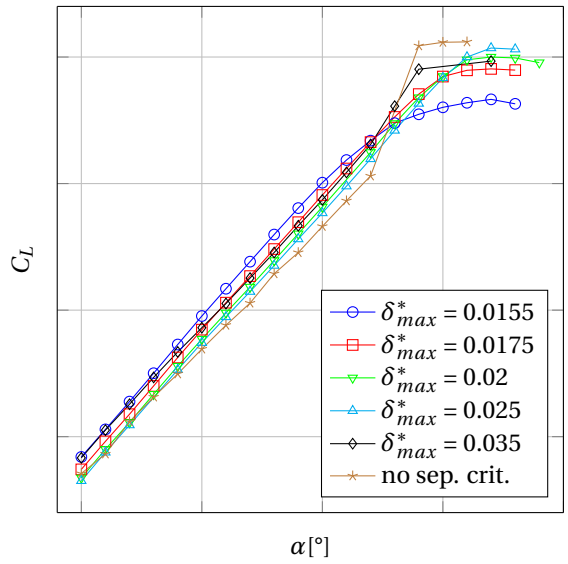

Figure 3.10: Lift curves of locally optimized designs for different δ^*_{max} limits.

It would be expected that if the flow is not separated at α = -5°, it would also not separate at any of the higher α. But when the optimization was run with only two angles of attack, designs emerged that satisfied attached flow criteria at both angles of attack, but had separated flow at some angles of attack between -5° and 12°. Thus the α = 8° was added as a control point and the following optimization runs successfully found designs without any jumps in the lift curve.

3.2.4. BOUNDARY LAYER TRIP ON THE FLAP

After running the MSES calculations with free transition, it emerged that the majority of promising designs developed laminar separation bubbles and turbulent reattachment on the upper surface of the flap. When the same design was analysed with a forced transition in front of the pressure recovery region on the flap upper surface, the turbulent boundary layer would separate at the chordwise location where in the free transition case it only transitioned from laminar to turbulent. Displacement thickness over the flap for both cases is shown in figure 3.11. Since turbulent boundary layer should be able to resist higher adverse pressure gradients before separation than laminar [10], it is questionable whether the free transition case is realistic. Therefore it was decided to trip the boundary layer on the flap before it reaches the suction peak, as this case represented less margin to separation for MSES. All the relevant design cases were analysed with this setting. Additional two reasons for forcing the transition were a) that the actual transition location may well be at the earlier point than what MSES predicts due to turbulence in the vicinity of the main element cove where the flow is separated and b) because in case of hysteresis being observed during wind tunnel testing of the final design, a zigzag tape might be fitted to the flap leading edge to force early transition [23].

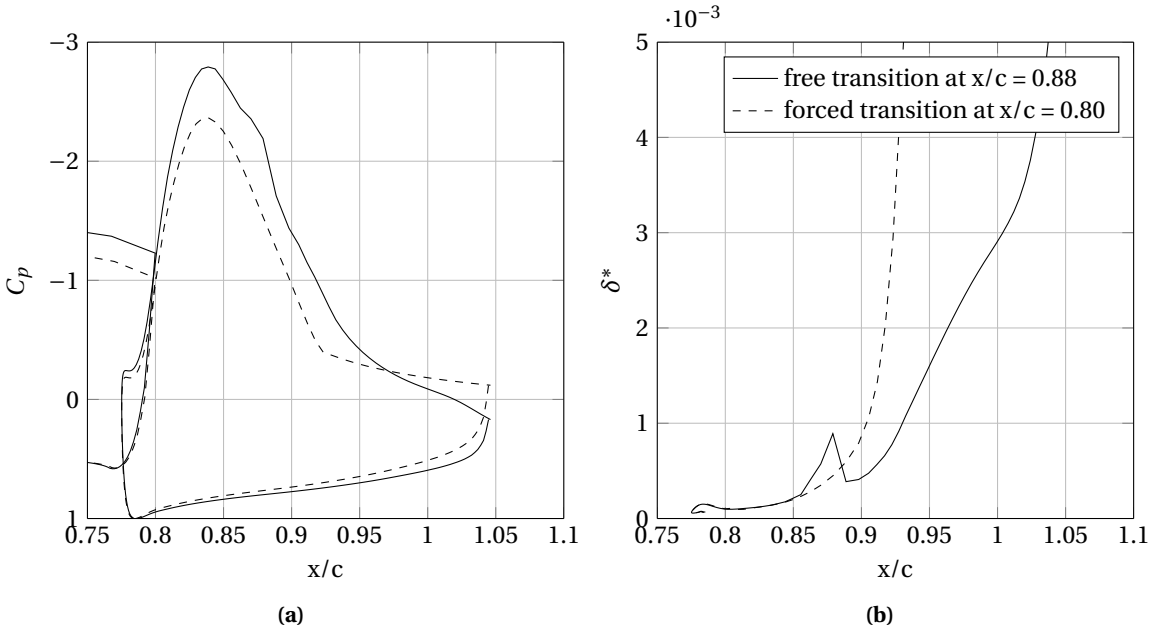

Figure 3.11: Pressure distributions (a) and boundary layer displacement thickness on the flap upper surface (b) for the same design with free and forced transition location ($Re = 2.1e6$).

3.3. THREE-DIMENSIONAL AERODYNAMIC ANALYSIS

In order to calculate the three-dimensional aerodynamic coefficients of the full aircraft, namely C_L, C_D and C_M, based on two-dimensional airfoil characteristics (obtained with MSES, see section 3.2), the wing planform and overall aircraft configuration, the following semi-empirical methods are used:

- ESDU 91014 [51] for estimation of $C_{L_{max}}$ based on $\Delta C_{l_{max}}$ at the midspan of the flap and wing planform, see subsection 3.3.1,
- ESDU 93019 [52] for estimation of C_L at low angles of attack based on ΔC_l at midspan of the flap and the clean configuration polar of the aircraft, see subsection 3.3.2,
- the method from reference [53] for estimation of induced drag of the wing with deployed flaps based on ΔC_L, the clean configuration polar and the wing planform, see subsection 3.3.3.

In addition, the VSAERO panel code, subsection 3.3.4, was used to validate the ESDU 93019 method and apply it to higher angles of attack and to validate the induced drag prediction method. Moreover, the VSAERO code was used to compute the wing-only polars and compare it to the flight-test results in order to estimate the drag of the fuselage and landing gear of the aircraft (see section 3.7).

3.3.1. ESTIMATION OF $C_{L_{max}}$

ESDU 91014 [51] outlines a semi-empirical method for estimation of the maximum lift coefficient of the finite wing with deployed part-span flaps. The ESDU 91014 document states the accuracy of predicting the $C_{L_{max}}$ for unswept wings to be +/-5% for 88% of the examples tested. $C_{L_{max}}$ is computed by first calculating the increment $\Delta C_{L_{max}}$ by equation 3.20 and then adding it to the clean wing $C_{L_{max}}$. Table 3.4 explains the meaning of the variables in equation 3.20. The values are calculated from additional equations and plots in ESDU 91014. The actual values used in the present project are derived in section 3.7. Note that the angle of attack at which the $C_{l_{max}}$ of the airfoil section is reached is not specifically taken into account in this method, but all of the designs during the optimization are compared at the same angle of attack.

$$\Delta C_{L_{max}} = K_f \, F_R \, \Delta \frac{\Delta C_{l_{max}}}{\mu_p} \, (\Phi_o - \Phi_i) \tag{3.20}$$

$\Delta C_{L_{max}}$	increment in $C_{L_{max}}$ of the finite wing due to deployment of part-span trailing-edge flaps
K_f	correction factor for type of flaps
F_R	correction factor for Reynolds number
$\Delta C_{l_{max}}$	increment in $C_{l_{max}}$ of the airfoil at the flap midspan due to deployment of a trailing-edge flap
μ_p	peak value of normalised local lift coefficient
Φ_i	spanwise position factor of inboard flap edge
Φ_o	spanwise position factor of outboard flap edge

Table 3.4: Meaning of variables in equation 3.20.

The decrease of $C_{L_{max}}$ due to downforce on the horizontal tail at trim condition is taken into account with equation (3.21). See figure 3.12 for the explanation of variables in equation (3.21).

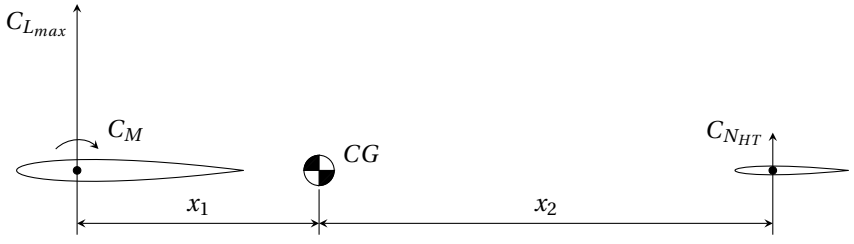

Figure 3.12: Force and moment diagram about the CG of the aircraft.

$$C_{L_{max,trim}} = C_{L_{max}} - \frac{C_{L_{max}} \cdot x_1 - C_M \cdot MAC}{x_2} \tag{3.21}$$

3.3.2. ESTIMATION OF C_L AT LOW ANGLES OF ATTACK

ESDU 93019 [52] describes a semi-empirical method for estimation of the finite wing lift coefficient due to deployment of part-span trailing-edge flaps at zero angle of attack. However, it was also used at higher angles of attack after this extension of the original scope was validated with VSAERO, see subsection 3.7.3. The variables in equation 3.20, which is found in the ESDU 93019, that are different to the ones in equation 3.20, are described in table 3.5 and the actual values are derived in section 3.7.

$$\Delta C_L = K_{f0}\, \Delta \frac{\Delta C_l}{a_{1_0}}\, a_1\, (\Phi_o - \Phi_i) \tag{3.22}$$

ΔC_L	increment in C_L of the finite wing due to deployment of part-span trailing-edge flaps
K_{f0}	correction factor for type of flaps
$\Delta C_{l_{max}}$	increment in C_l of the airfoil section due to deployment of a trailing-edge flap (airfoil at midspan of the flap was considered)
a_1	lift curve slope of the wing in clean configuration
a_{1_0}	lift curve slope of the airfoil section with deployed flaps

Table 3.5: Meaning of variables in equation 3.22.

3.3.3. CALCULATION OF THE AIRCRAFT C_D

To calculate the C_D of the aircraft in different configurations, the drag was broken down in standalone terms, see equation 3.23. Calculation of induced drag C_{D_i} and profile drag of the wing C_{D_p} are described in the remaining of this subsection. Drag coefficients of the fuselage, $C_{D_{fus}}$, and landing gear, $C_{D_{lg}}$, were derived from the flight test data (subsection 3.7.1) and kept constant throughout the design process.

$$C_D = C_{D_i} + C_{D_p} + C_{D_{fus}} + C_{D_{lg}} \tag{3.23}$$

Estimation of induced drag of the wing with part-span flaps

Reference [53] provides a method for calculating the induced drag of the wing with part-span trailing-edge flaps. The method is based on a lifting-line theory where the spanwise distribution of the circulation is expressed as a Fourier series. For a given flap spanwise location the Fourier coefficients are calculated and the induced drag follows. Precomputed values from reference [53] are used to find the coefficients for the wing in question. In equation 3.24 these coefficients are represented by K_f and K_A. C_L in equation 3.24 stands for the lift coefficient of the wing with flaps deployed, while the ΔC_L stands for the increment in lift coefficient of the wing due to deployment of the flaps, which can be calculated with equation 3.22. The actual values of the K_f and K_A are derived in section 3.7.

$$C_{D_i} = \frac{C_L^2}{\pi A}\left(1 + K_f K_A \frac{\Delta C_L^2}{C_L}\right) \tag{3.24}$$

Calculation of the profile drag of the wing

Profile drag of the wing (C_{D_p}) was calculated by integrating the sectional drag coefficients along the span of the wing using equation (3.25) that was discretized in the finite number of spanwise sections. The detailed calculation is presented in subsection 3.7.5. Pitching moment of the wing (C_M) is calculated in the same way.

$$C_{D_p} = \int_0^{b/2} C_D(y)\, \frac{c(y)}{c_{ref}}\, dy \tag{3.25}$$

3.3.4. VSAERO - 3D PANEL CODE WITH BOUNDARY LAYER METHOD

VSAERO [54] is a program developed by Analytical Methods that is capable of computing potential flow about arbitrary three-dimensional bodies and coupling the inviscid solution with the boundary layer equations in the vicinity of the body surface. The geometry has to be presented to VSAERO in the form of body and wake panels. Surface panel mesh is shown in figures 3.13a and 3.13b.

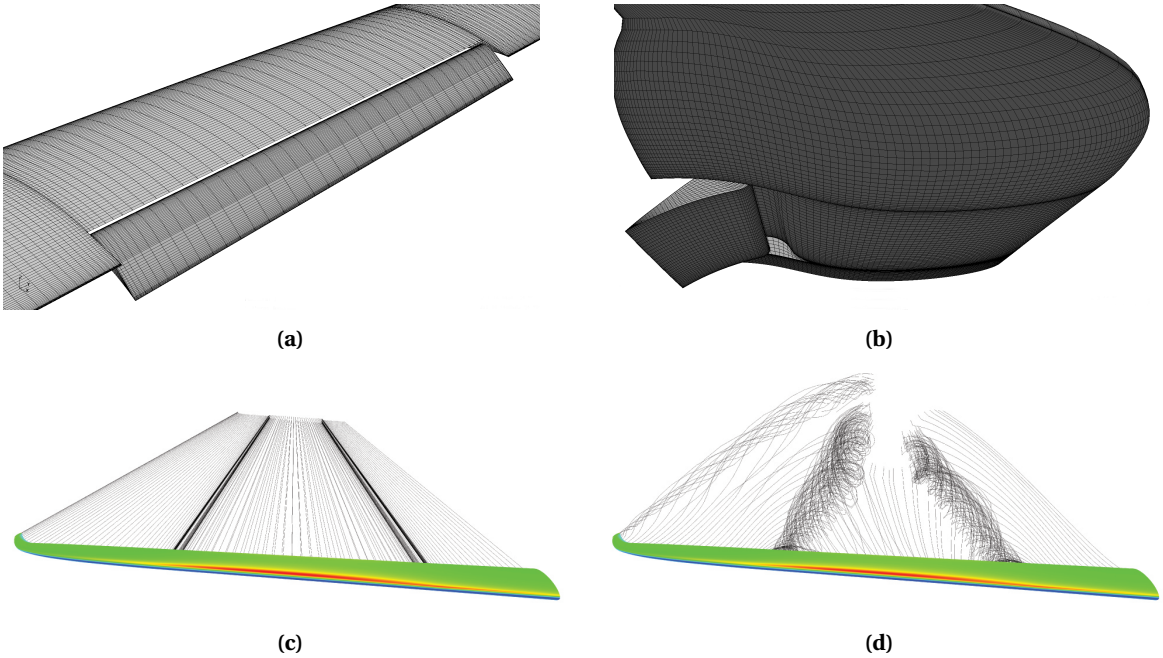

Figure 3.13: VSAERO surface mesh of the wing with part-span single-slotted flap (a and b) and wake in initial (c) and converged (d) form.

VSAERO performs iterative calculation during which the wake shape is changing until convergence (figures 3.13c and 3.13d). After wake iterations, inviscid-viscous iterations are performed to calculate the boundary layer characteristics and corrected inviscid pressure distributions over the wing, while wake geometry stays constant. VSAERO can detect boundary layer separation, but does not alter the calculation according to the separated flow since the separation is always assumed where the user prescribes the wakes. It is possible to change the wake separation position to the detected boundary layer separation and run the calculation again, but the process is time consuming and it is difficult to judge its accuracy. In case of flap designs that are the subject of this project, the lift limiting phenomena at high angles of attack is not boundary layer separation off the surface but rather wake bursting, which is impossible to account for in VSAERO. It is therefore expected that VSAERO overpredicts $C_{L_{max}}$, but can still be used for lift, drag and pitching moment calculations at lower angles of attack. The use of VSAERO for validating the semi-empirical methods and estimating the drag of the fuselage and landing gear is described in section 3.7.

3.4. DESIGN OF FLAP SUPPORT MECHANISM

When redesigning the plain flap high lift system into a single-slotted flap system the design of the flap deployment mechanism has an important impact on the overall performance of the aircraft because of its weight and drag. As described in section 3.2, the hinge point location was one of the design variables in the optimization routine. Based on the hinge point location and the calculated loads on the flap (subsection 3.4.1), the mechanism brackets were sized automatically in each iteration to estimate their weight (subsection 3.4.4). Afterwards, the drag of the fairings enclosing the bracket could be estimated (subsection 3.4.3).

3.4.1. CALCULATION OF FLAP LOADS

The flap has three spanwise supports - one on each end and one at midspan, see figure 3.14a. For calculating the loads in each of the supports the flap was treated as a simple beam in bending. Because three supports make the beam statically indeterminate and because the spanwise loading is in general an arbitrary function, a finite element method was used to calculate the reaction forces in each of the supports. The process of obtaining the loads in the supports has the following steps:

- read 2D flap force coefficients C_x and C_y from MSES calculation,
- calculate the normal force coefficient C_n,
- assume elliptical distribution of C_n along the span of the flap and calculate the actual load distribution (figure 3.14b),
- compute the second moment of area about the neutral plane of the flap for sufficient number of spanwise sections (figure 3.15),
- use finite element method to calculate the displacements of the flap along the span and reaction loads in each of the supports.

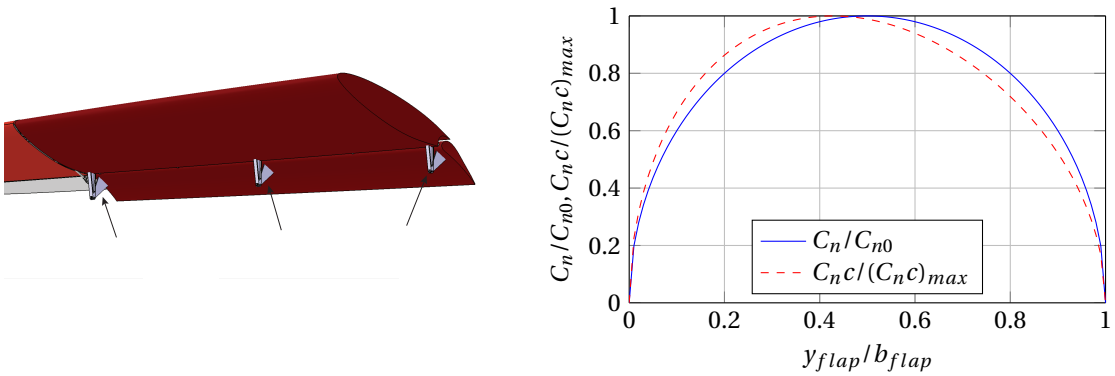

(a) **(b)**

Figure 3.14: Three flap supports indicated by arrows (a) and the elliptical C_n distribution along the flap (b).

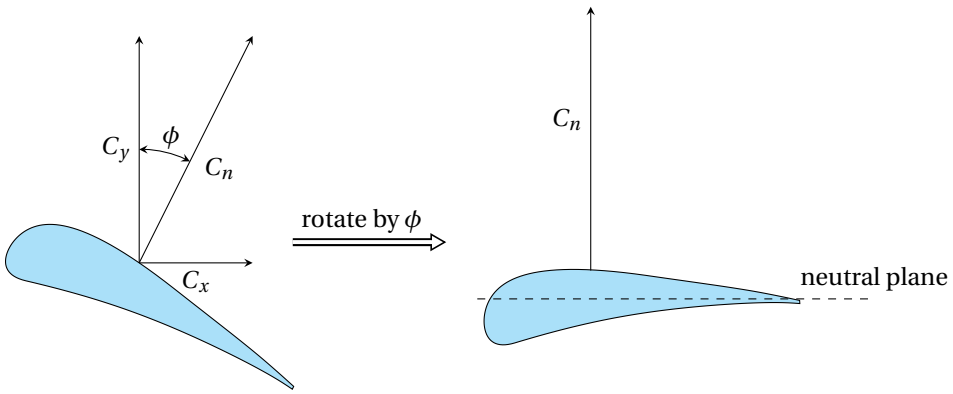

Figure 3.15: To calculate the second moment of area of the section, the neutral plane is assumed perpendicular to the C_n.

Assuming the elliptical distribution of C_n over the flap span is an approximation but it is sufficiently accurate for load calculation and it was also implemented in the design method of reference [5]. Figure 3.16a shows the flap as a beam constrained by three supports. The beam is divided into a sufficient number of beam elements along its span. The beam finite elements support shear and bending. The relation between single element displacements (displacement, rotation) and loads (shear force, bending moment) is given in equation (3.26)

from reference [55]. After the global matrix is solved for displacements and rotations, the reaction forces are also known. Typical result of the calculation is plotted in figure 3.16b.

$$\begin{bmatrix} F_i \\ M_i \\ F_j \\ M_j \end{bmatrix} = \begin{bmatrix} 12/L^3 & -6/L^2 & -12/L^3 & -6/L^2 \\ -6/L^2 & 4/L & 6/L^2 & 2/L \\ -12/L^3 & 6/L^2 & 12/L^3 & -6/L^2 \\ -6/L^2 & 2/L & 6/L^2 & 4/L \end{bmatrix} \begin{bmatrix} v_i \\ \theta_i \\ v_j \\ \theta_j \end{bmatrix} \tag{3.26}$$

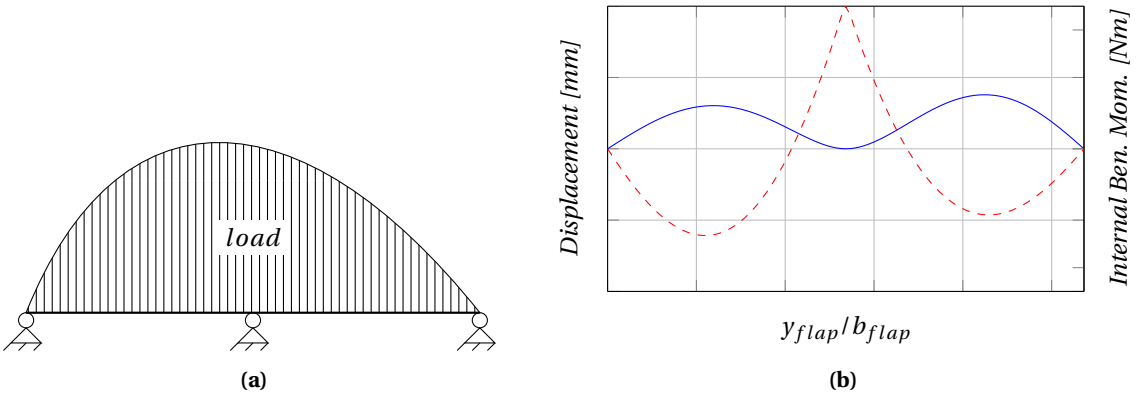

Figure 3.16: Beam model of the flap (a) and an exemplary result of the FEM calculation (b).

3.4.2. SIZING OF THE BRACKETS

A typical bracket that would be suitable for carrying the flap loads was designed and parametrized to allow rapid sizing in each iteration of the optimization routine. Figure 3.17 shows the bracket in three views and outlines the important dimensions. Parameters a, b and g are kept constant, parameters c, h and f are defined with the position of the hinge point, parameter e is proportional to the flap chord length and parameter d is sized depending on the bending load in the bracket that is modelled as a beam. Figure 3.18 shows the load case of the bracket. The reaction force F_R that is the result of aerodynamic force on the flap and is calculated with the finite element method described in 3.4.1, can be decomposed into forces perpendicular (F_P) and parallel (F_A) to the axis of the bracket. Force F_P causes a bending moment on the bracket that is increasing towards the root of the bracket. The most loaded section is indicated in figure 3.18, the bending moment on that section is given by equation (3.27). While dimensions g, t_1 and t_2 are constant, the dimension d is adjusted in order to give high enough second moment of area of the section for the stress not to exceed the maximum allowed value. The value of d is found as follows:

- calculate the bending moment at the critical section (equation (3.27)),
- calculate the second moment of area (I_x) and the cross sectional area (A) of the critical section (both dependent on d),
- calculate the normal (equation (3.28)) and shear (equation (3.29)) stress in the critical cross section,
- calculate Von Mises stress in the critical section (equation (3.30)),
- compare the calculated stress to the maximum allowed stress (equation (3.31)),
- adjust d accordingly for the $\sigma_{von\,mises}$ to be within a certain tolerance of $\sigma_{allowed}$ to get the optimal design.

In addition, force F_A causes a compressive stress in the bracket and force F_P also causes shear - both are accounted for in the calculation of Von Mises stress, but are almost negligible compared to the bending load.

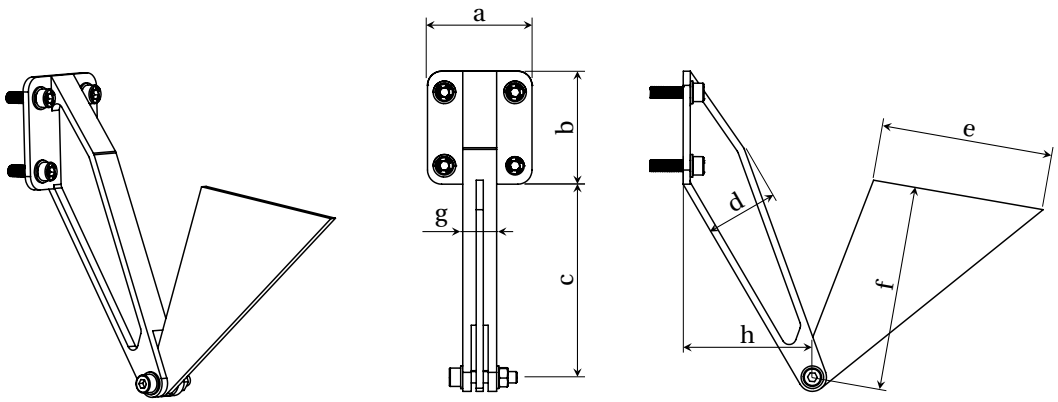

Figure 3.17: Parametrization of the flap support bracket.

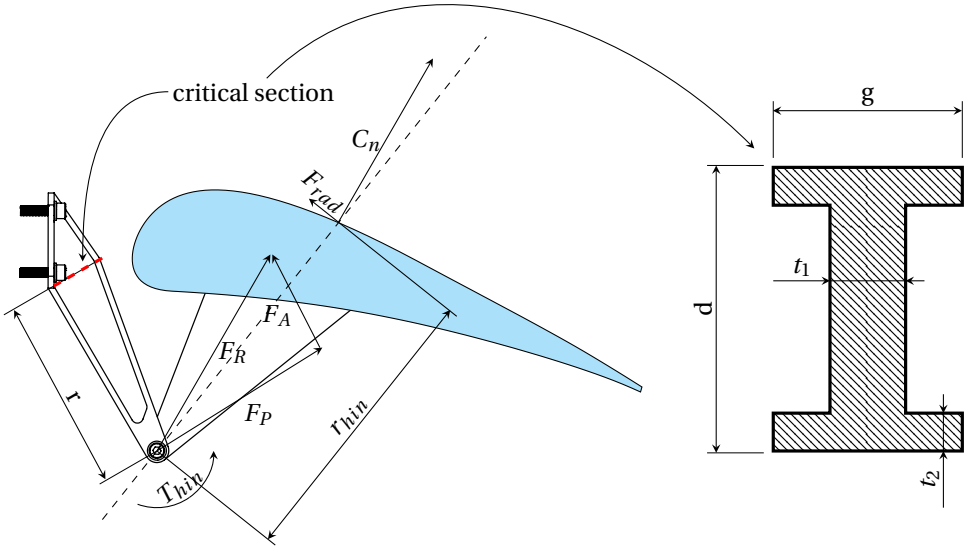

Figure 3.18: Loads acting on the flap bracket and the definition of the most loaded section.

$$M_b = F_P \cdot r \tag{3.27}$$

$$\sigma_{max} = \frac{M_b d/2}{I_x} + \frac{F_A}{A} \tag{3.28}$$

$$\tau = \frac{F_P}{A} \tag{3.29}$$

$$\sigma_{von\,mises} = \sqrt{\sigma_{max}^2 + 3\tau^2} \tag{3.30}$$

$$\sigma_{von\,mises} < \sigma_{allowed} \tag{3.31}$$

Although there are three brackets per flap, the above calculation procedure is only performed for the bracket at the midspan of the flap. The weight of the single bracket is multiplied by six to get the total weight of the

six brackets. This is a slight simplification, but is reasonably accurate since the size of the middle bracket is approximately the average of the sizes of the outer and inner flap edge brackets, because the bracket size is proportional to the wing chord at its spanwise location and the chord is decreasing linearly with span.

3.4.3. DRAG OF THE MECHANISM FAIRINGS

After the mechanism brackets have been sized, it is assumed that an airfoil shaped fairings with blunt trailing edge are fitted to enclose the dropped hinge brackets, see figure 3.19a. Blunt trailing edge is assumed so that the fairing can be a simple one piece shell fitted around the bracket with an open slot at the back end that allows the deflection of the flap fitting. Reference [56] proposes an estimation method based on experimental data to calculate two-dimensional drag coefficient of airfoils with blunt trailing edges based on the area of the base S_b (length h in figure 3.19b for two-dimensional case).

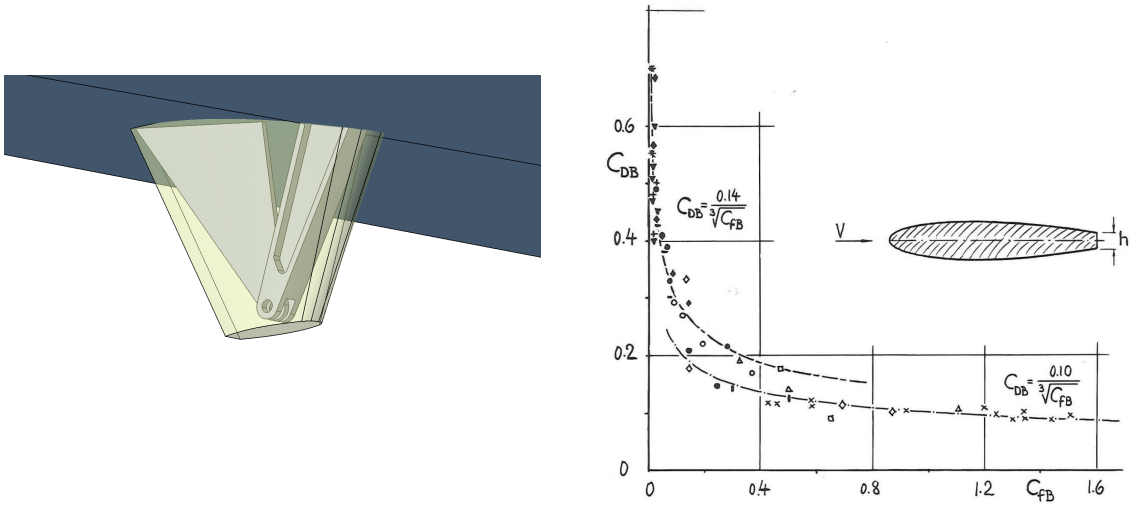

(a) **(b)**

Figure 3.19: Airfoil shaped bracket fairing with blunt trailing edge (a), drag of an airfoil section with blunt trailing edge (from [56]) used for bracket fairing drag estimation.

Base drag coefficient C_{BD} is given as a function of coefficient C_{FB} which is calculated with equation (3.32), where C_f is a skin friction coefficient of the airfoil and S_{wet} is the wetted area (or arc length for a two-dimensional case). To calculate the drag coefficient of the fairing, first an average C_{DB} along its span is calculated with equation (3.32), using the wetted area of the whole fairing and the area of the trailing edge slot. Then equation (3.33) is used to calculate the base drag coefficient and finally equation (3.34) gives the drag coefficient of the fairing normalized with respect to the aircraft wing area S. As there are six fairings on the aircraft and the described calculation is performed with the data of the fairing at the midspan of the flap that has an approximately average size of all the brackets, the value from equation (3.34) is multiplied by the number of fairings to get the total fairing drag. Note that figure 3.19b lists two equations for C_{DB}. Equation 3.33 was used because it has a better fit for low values of C_{FB} that were encountered in the case considered.

$$C_{FB} = C_f \, S_{wet} \, S_b \tag{3.32}$$

$$C_{DB} = \frac{0.14}{C_{FB}^{\frac{1}{3}}} \tag{3.33}$$

$$C_{D,fairing} = C_{DB} \frac{S_b}{S} \tag{3.34}$$

3.4.4. SIZING OF THE FLAP

FAR 23 [43] states that the flap should be sized to withstand a load factor of 2.2 in deployed position and a load factor of 4.4 in retracted position. Preliminary calculations of flap loads indicated that the worst load case for the flap is during maneuvering with the load factor of 4.4 in retracted position, see appendix A.3. Since the loads in clean configuration are independent of the flap design and similar to the loads on the plain flap, the weight of the slotted flap itself was assumed to stay the same as the weight of the original plain flap.

3.4.5. ACTUATOR SIZING

The actuation force, denoted F_{act} in figure A.23 in appendix A.7, is calculated with equation (3.36). F_{dln} stands for the force on top of the link that creates a moment about the torque tube (see figure A.23) and is approximately equal to the F_{rad} in figure 3.18, see equation (3.35). For realistically possible dimensions r_{dln} and r_{act}, and the expected values of F_{rad}, the maximum actuator force does not exceed 6000 N. As mentioned in subsection 2.3.3, the weight of the actuator appropriate for such loads is low compared to the expected increase in the $MTOW$ because of the new high lift system. Therefore the actuator sizing and its weight estimation was excluded from the optimization scheme. In table 4.2 the moment about the hinge axis (T_{hin} in figure 3.18), that is a good representation of the loads on the actuator, is presented for the optimized designs.

$$F_{dln} \approx F_{rad} \tag{3.35}$$

$$F_{act} = 2F_{dln}\frac{r_{dln}}{r_{act}} \tag{3.36}$$

3.5. WING AND LANDING GEAR WEIGHT ESTIMATION

The weight of the wing and the landing gear increases as a consequence of the new flap design because the $MTOW$ is increased. Wing and landing gear weights are not negligible, but have rather large contributions - both weights summed up are expected to be comparable to the additional weight of the fuel (section 3.1.3) and thus have a substantially larger effect on overall aircraft performance than the weight of the brackets (section 3.4.4). Despite their considerable effects, the detailed design of the wing and landing gear is out of the scope of this thesis. Therefore, methods suitable for preliminary weight estimation were used. They are presented in subsections 3.5.1 and 3.5.2. The actual values of aircraft specific coefficient that were used in this project are given in subsection 3.7.6.

3.5.1. WING WEIGHT

Reference [41] proposes equation (3.37) for quick wing weight estimation. Reference span, b_{ref}, is 1.905 m and proportionality factor, k_w, is 0.0049. b_s is structural span that is equivalent to the span b for the unswept wing. t_r is the maximum wing thickness at the root and n_{ult} is the ultimate load factor.

$$\frac{W_{wing}}{MTOW} = k_w b_s^{0.75}\left(\sqrt{\frac{b_{ref}}{b_s}}\right)n_{ult}^{0.55}\left(\frac{b_s/t_r}{MTOM/S}\right)^{0.3} \tag{3.37}$$

3.5.2. LANDING GEAR WEIGHT

For landing gear weight prediction the model from reference [41] is used. It is based on statistical data and separately determines the weight of the nose and main landing gear. Equation (3.38) is used where coefficients A, B, C and D are determined based on aircraft and landing gear type. $i = 1$ is used for the main gear and $i = 2$ for the nose gear.

$$m_i = A_i + B_i \cdot MTOM^{\frac{3}{4}} + C_i \cdot MTOM + D_i \cdot MTOM^{\frac{3}{2}} \tag{3.38}$$

3.6. OPTIMIZATION SCHEME

After the design of the high lift system has been selected down to the type of the flap (single-slotted) and mechanism (dropped hinge) as described in section 2.4, optimization algorithms were used to find the optimum combination of design variables (section 3.2.1) that define the flap geometry, hinge position and flap deflection angle. Since the goal is to maximize the payload, the objective function to be minimized is formally given with equation 3.39.

$$obj(C_1 - C_2, C_2, dR_1, t_2, C_{3Y_1}, C_{3dY_2}, HP_Y, dHP_X, \delta_f) = -W_{payload} \tag{3.39}$$

Figure 3.20 shows the work flow diagram for the computation of the objective function. The methods used in the individual steps are described in sections 3.2 to 3.5. The optimization problem itself is an unconstrained one, but the objective function includes two tests for discarding the designs. Firstly, if MSES calculation cannot converge, the objective (payload) is set to 0 and further calculations are not performed. Secondly, if the δ^* is not within the prescribed limit, the objective is set to 0 as well.

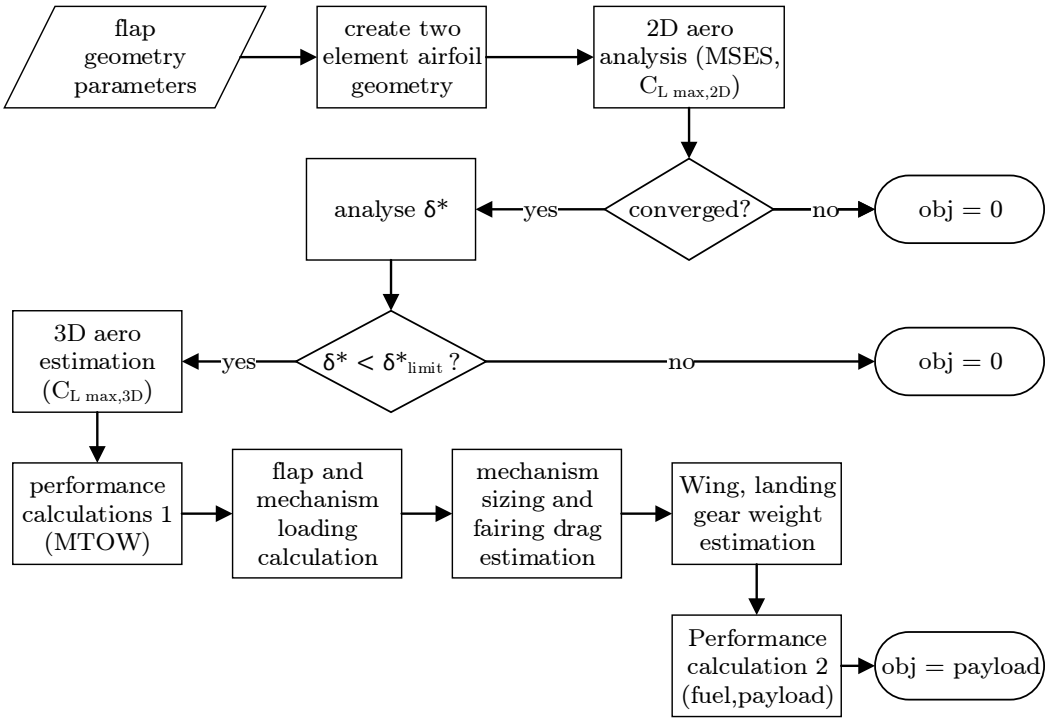

Figure 3.20: Work flow to compute the objective function that is performed in each iteration of the optimization.

The objective function does not have a solution for each combination of design variables within the desired design space, mainly because the MSES code has problems with convergence for certain geometries. Therefore the gradient based optimization algorithms are no suitable for this application. The problem of optimizing the flap geometry is also highly global. For example, the same gap and overlap of the flap can be obtained with different combinations of flap geometry, hinge position and deployment angle. Thus a global algorithm had to be used.

Matlab's genetic algorithm was used to initiate the optimization, but could not be run until convergence because of the long computation time. After a certain number of iterations when a promising design has emerged and all individuals started to converge towards it, the genetic algorithm was stopped. The best

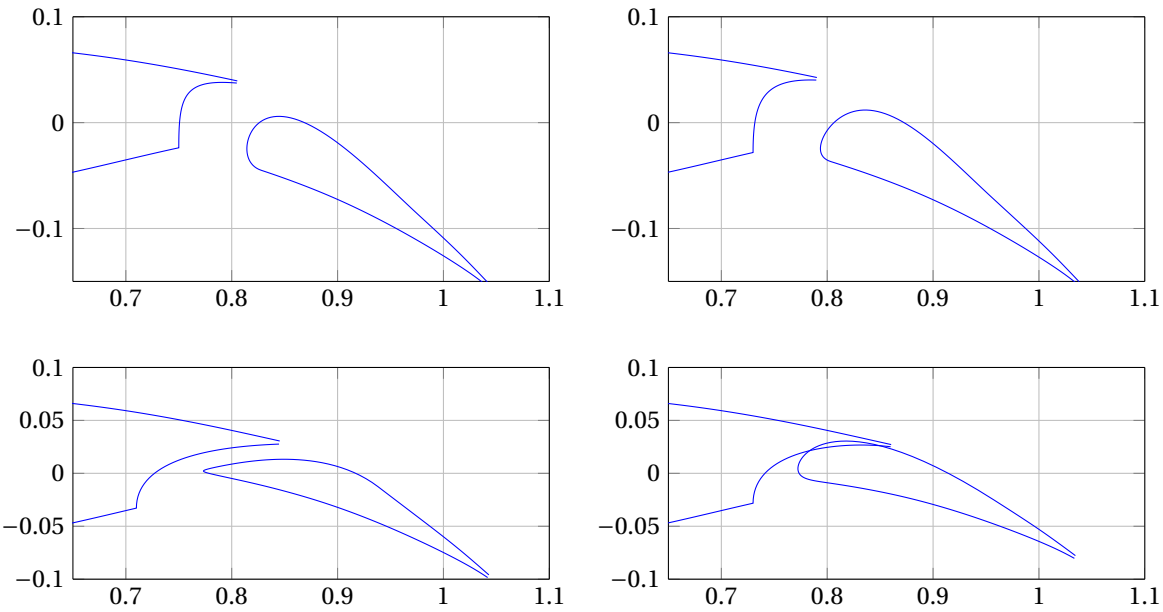

Figure 3.21: Examples of flap geometries that are possible within the design space, but do not converge in MSES.

design was selected as the initial design for Matlab's pattern search algorithm which found the local minimum around that point.

Genetic algorithm run itself had to be divided into two stages. Randomly generated designs of the initial generation produced only about 10% of feasible geometries with the objective value not equal to 0. Despite the upper and lower bounds placed on the design variables, designs emerged that had no convergence in MSES, some such examples are shown in figure 3.21. Moreover, some designs converged in MSES, but had separated flow at at least one of the evaluated angles of attack.

The solution to this problem was to run a population large enough that the number of feasible designs was at least 10 times the number of design variables (9). That meant having an initial population of 1000, but the size could not be decreased for the subsequent generations. Thus only one generation of the genetic algorithm with population size of 1000 was run. Then the algorithm was stopped and the best 100 designs were used as an initial population for the second stage genetic algorithm which continued for 10 to 20 generations before it was stopped and the pattern search algorithm started. The optimization process is summarized in figure 3.22. Typical computation times for the complete optimizations were from one to two days on a processor with 8 threads.

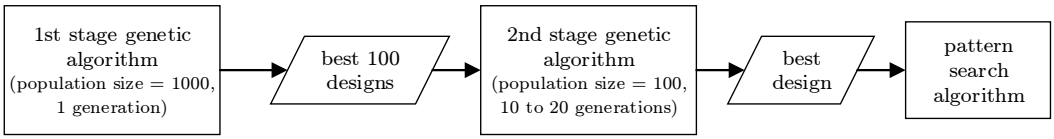

Figure 3.22: Optimization process flow diagram.

A note on take-off configuration

The flow chart in figure 3.22 does not include the evaluation of the high lift system in take-off configuration. The take-off flap deflection angle was found after the optimization finished and the optimum flap for landing configuration was found. δ_f was then decreased in steps of 1° to find the setting which had the highest value of (three-dimensional) L/D for a given payload.

3.7. METHODOLOGY DATA

In previous sections describing the methodology the actual values of numerous parameters were omitted. It is the purpose of the present section to derive all the values to be used in the design process.

3.7.1. FLIGHT TEST DATA

Subsection removed from the public version of the thesis report due to confidentiality reasons.

3.7.2. ESDU 91014 DATA

Subsection removed from the public version of the thesis report due to confidentiality reasons.

3.7.3. ESDU 93019 DATA

Subsection removed from the public version of the thesis report due to confidentiality reasons.

3.7.4. DATA FOR PREDICTION OF INDUCED DRAG

Subsection removed from the public version of the thesis report due to confidentiality reasons.

3.7.5. DATA FOR PREDICTION OF C_{D_p} AND C_M

Subsection removed from the public version of the thesis report due to confidentiality reasons.

3.7.6. WING AND LANDING GEAR WEIGHT PREDICTION DATA

Subsection removed from the public version of the thesis report due to confidentiality reasons.

4

RESULTS AND CONCLUSIONS

Preliminary design decisions were discussed in subsection 2.4, where it was decided that a slotted flap with a dropped hinge mechanism will be optimized in detail. The disciplines evaluated within the optimization were presented in chapter 3. The present chapter presents the results of the aforementioned optimization process, using the objective function from figure 3.20. Presentation and discussion of results are merged into a single section (section 4.1), while the last section summarizes the conclusions and recommendations (section 4.2).

4.1. DISCUSSION OF RESULTS

Four different optimization runs are discussed, differing in slight changes in design space, as shown in table 4.1. The detailed meaning of the design variables is presented in section 3.2.1. The runs are referred to by names indicating the date of running (Jun10, Jun12, Jun13 and Jun15). A blank field in table 4.1 means that the value from the preceding run was used. The results for the best designs of each optimization run are shown in table 4.2. See appendix A.4 for the histories of the objective function value throughout the runs.

Variable	**Jun10**	**Jun12**	**Jun13**	**Jun15**
$C_1 - C_2$	0.12 to 0.15			
C_2	0.72 to 0.75		0.74 to 0.77	
dR_1	0.00 to 0.60			
t_2	0.03 to 0.08			
C_{3Y_1}	-0.03 to 0.02			-0.03 to 0.01
C_{3dY_2}	0.005 to 0.05			0.005 to 0.04
HP_Y	-0.30 to -0.14	-0.16 to -0.14		
dHP_X	0.00 to 0.03			
δ_f	20.0°to 30°			
C_3x	0.70		0.72	
flap l.e. limit	no explicit limit		0.71	0.72

Table 4.1: Design space for the four optimization runs; blank field means the value is unchanged from the preceding run.

First, some general observations are discussed. Figure 4.1 plots payload with respect to $C_{l_{max}}$ for all the designs during an exemplary optimization run that returned the $C_{l_{max}}$ higher than 2.4. It can be seen that payload depends predominantly on $C_{l_{max}}$. For the same $C_{l_{max}}$ there is not much variation in payload between different flap designs: about 10 kg for lift coefficients of about 2.4 and only about 2 kg for the highest lift coefficients. This indicates that when the design is selected down to the type of the high lift system and con-

strained with clean configuration and spanwise position, the optimization process is more an aerodynamic optimization than a highly coupled multidisciplinary optimization.

Variable	**Jun10**	**Jun12**	**Jun13**	**Jun15**
$C_{l_{max}}/C_{l_{max,plain}}$ []	1.265	1.26	1.27	1.21
$C_{L_{max,trim}}/C_{L_{max,trim,plain}}$ []	1.12	1.125	1.13	1.1
$Payload$ [kg]	480	486	489	459
$MTOM$ [kg]	1480	1483	1486	1447
$\Delta W_{payload}/\Delta MTOW$ []	0.818	0.839	0.842	0.864
HP_Y []	-0.298	-0.157	-0.150	-0.151
$C_{D,fairings}$ []	0.0018	0.0010	0.0010	0.0010
$\Delta m_{fuel,fairing}$ [kg]	7.3	4.1	4.1	4.1
Δm_{fuel} [kg]	22	19	19	15
Δm_{wing} [kg]	13	13.5	14	10.5
$\Delta m_{landing\,gear}$ [kg]	7	7	7.5	5.5
$m_{mechanism}$ [kg]	3.7	2.6	2.5	2.5
flap l.e. x-coord. []	0.702	0.692	0.718	0.721
$(C1_X - C2_X)_{eff}$ []	0.110	0.075	0.065	0.079
gap []	0.029	0.021	0.02	0.02
$overlap$ []	0.010	0.033	0.025	0.031
$\delta_{f,landing}$ [°]	24.5	23.6	24.7	25.5
$\delta_{f,T-O}$ [°]	15.5	14.6	16.7	14.5
$\gamma_{@MTOW}$ [°]	5.1	5.1	5.0	5.4
s_{T-O} [m]	604	606	608	591
$s_{landing}$ [m]	661	662	664	651
T_{hin} [Nm]	332	342	297	267

Table 4.2: Optimization results for design spaces from table 4.1.

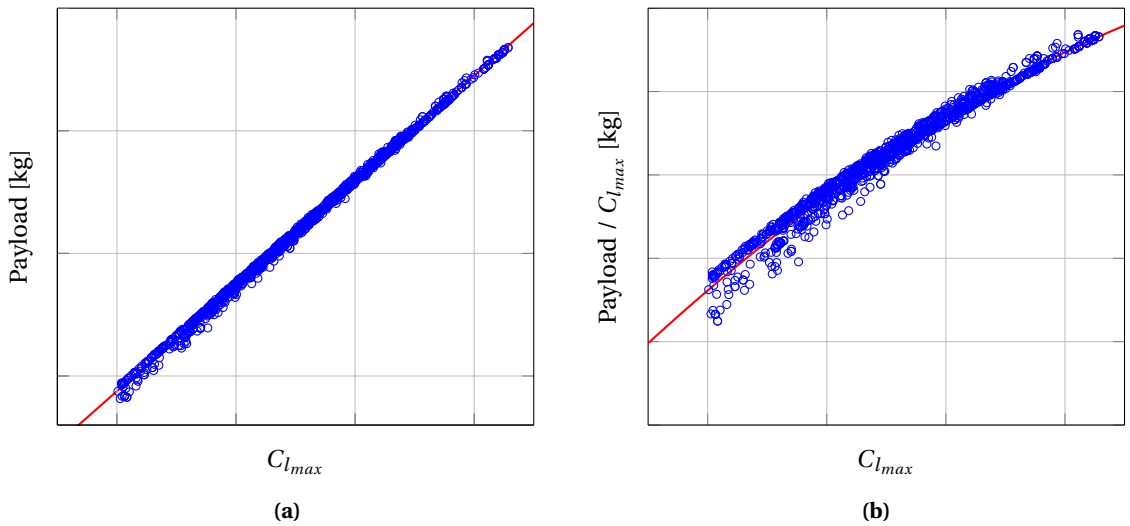

(a) **(b)**

Figure 4.1: Payload with respect to $C_{l_{max}}$ for all iterations of an exemplary optimization that returned $C_{l_{max}}$ higher than 2.4.

The method of limiting the maximum displacement thickness of the flap wake (as described in subsection 3.2.3) proved to be very reliable since none of the optimized designs suffered from separation when they were analysed over the whole angle of attack range after the optimization finished. 2D and 3D lift curves can be seen in figure 4.2a.

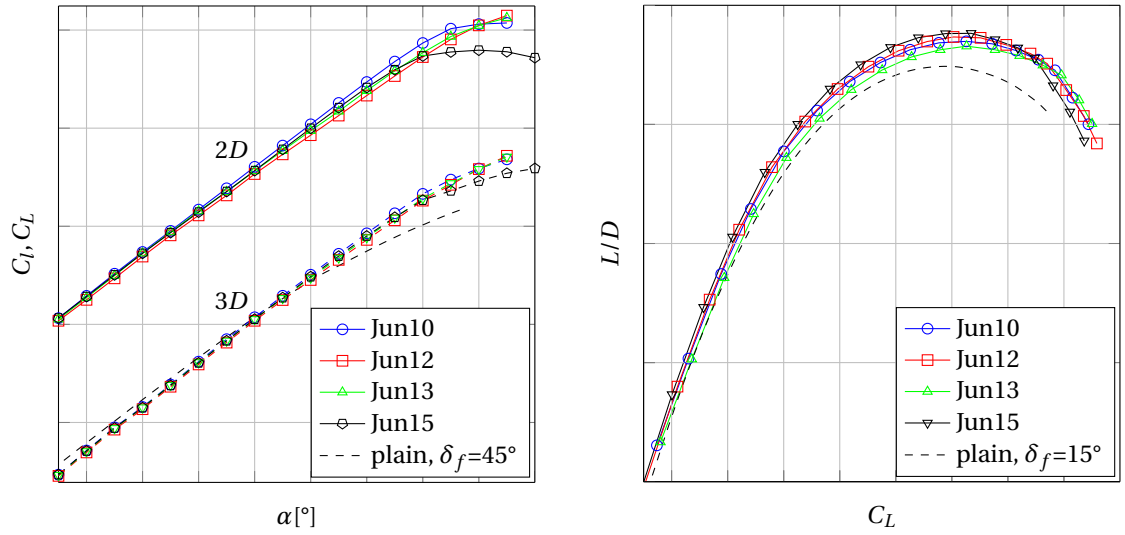

Figure 4.2: a) 2D (solid line) and 3D (dotted line) lift curves in landing configuration, b) 3D L/D curves in take-off configuration. Curves for the aircraft with plain flaps also shown, denoted $plain$.

The achieved maximum sectional lift coefficients were about 27% higher than for the aircraft with plain flaps, which is a typical improvement for single slotted flap configurations [18], [3]. The limiting factor in determining the maximum lift was not flow separation off the airfoil surface, but rather the bursting of main element's wake. As shown in figure 4.3, the wake of the main element widens extremely when it is close enough to the flap surface and therefore the positive pressure gradient at the flap surface is imposed on it [10]. A wide wake can be seen as a large displacement body that prevents the flow from following the flap surface, causing a decambering effect and thus reducing the circulation on the flap, which in turn reduces the circulation on the main element.

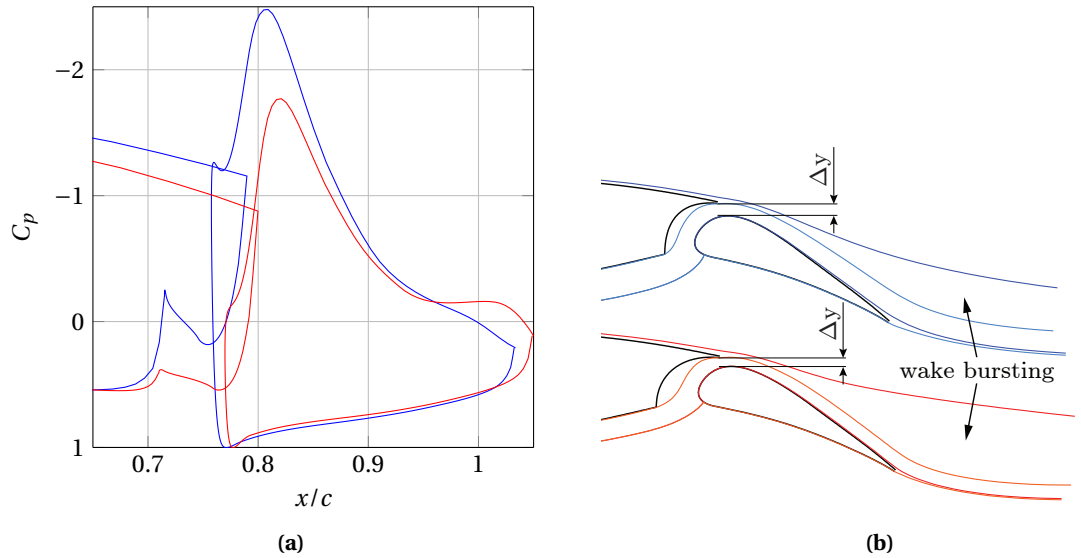

Figure 4.3: Effect of flap position on wake bursting.

Minimizing wake bursting turned out to be the key to achieving high lift coefficients. Amount of wake bursting is mainly determined by δ^* at the main element's trailing edge and the positive pressure gradient on the flap upper surface. Since the main element geometry can not be changed, there is not much that can be done about the δ^* as it is mainly determined by the pressure recovery region from the flap leading edge towards the trailing edge. Pressure gradient on the flap will as well have to be on the limit of separation if the configuration is to carry the maximum amount of lift. The most effective way of minimizing wake bursting was to position the flap further away from the main element's wake in order to reduce the pressure gradient experienced by the wake, while still maintaining small enough gap that maximizes the circulation effect of the two elements on each other. This effect can be seen in figure 4.3, where the vertical gap is denoted by Δy. The downward shift of the flap at constant δ_f is achieved with a forward shift of the hinge point, dHP_X. All the optimized designs have a relatively high value of this parameter, as seen in figure 4.4. Note that Δy does not represent the absolute gap between the elements, only the vertical projection.

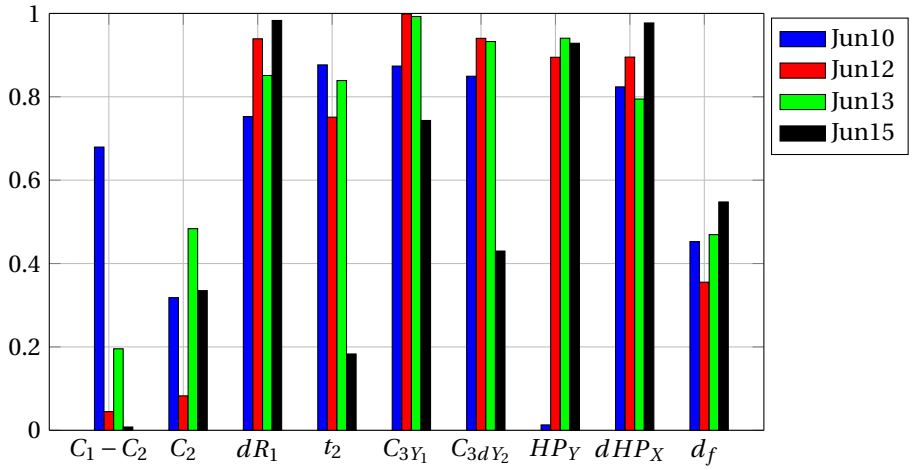

Figure 4.4: Design parameters for optimized designs, nondim. w.r.t. the Jun10 optimization design space.

From results in table 4.2 and the optimized flap geometries in figure 4.5, it is observed that, at least for Jun10, Jun12 and Jun13 cases, slight changes in initial design space return considerably different designs, but obtain similar values of payload. It can also be seen that the optimization does not return a true global minimum, since the final Jun12 design gives slightly higher payload than the Jun10, but is also feasible under Jun10 design space.

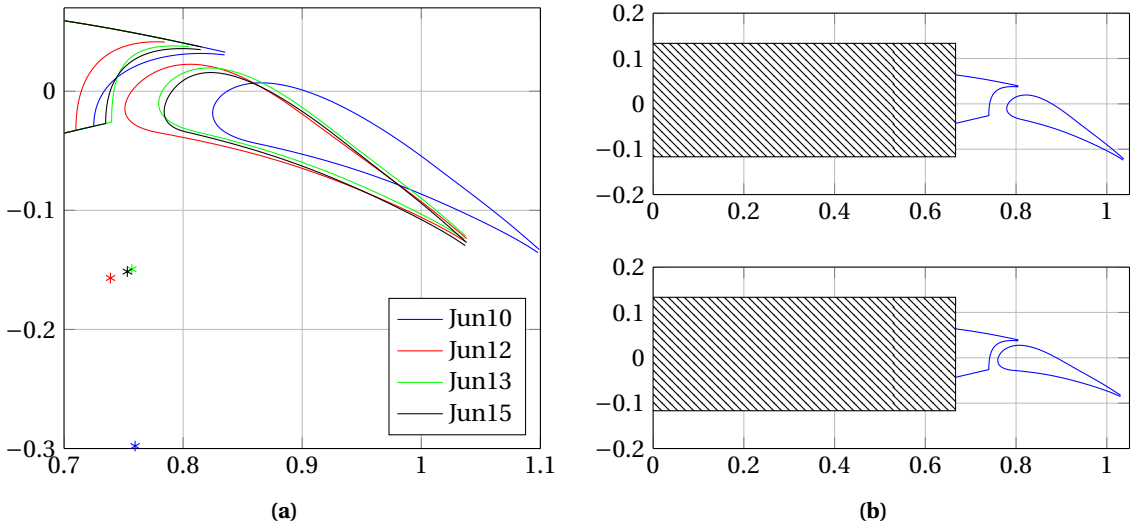

(a) **(b)**

Figure 4.5: Optimized flaps (a) and Jun13 in landing (b, top) and take-off (b, bottom) configuration. Part of the airfoil masked due to NDA.

Jun10 design space allows for very deep hinge point location that is in general favourable in achieving high lift coefficients, but also has higher drag in cruise condition. Indeed the Jun10 design needs about 3 kg of fuel more because of the hinge fairing than the Jun13 design for the same range of 1000 nm (see $\Delta m_{fuel,fairing}$ in table 4.2). For the Jun12, Jun13 and Jun15 optimizations, the hinge point location was limited between -0.14c and -0.16c, because it was felt that similar lift coefficients are possible with higher hinge positions, which was proven by Jun12 and Jun13 designs. The downside of the Jun12 design is the most forward point of the flap in clean configuration at 0.692c, which would need a slight forward shift of the rear spar.

For the Jun13 case, the flap leading edge position was limited definitely, not only with the x-coordinate of the b-spline control points (C_{3X}). This did not prove to be problematic in terms of high lift, since the Jun13 design even has a marginally higher lift than the Jun12 design. Because the Jun13 design has the lowest effective distance between lower and upper flap breaks ($(C1_X - C2_X)_{eff}$, see figure 3.2a), this resulted in the worst take-off performance of all designs (see table 4.2), because a short $(C1_X - C2_X)_{eff}$ generally allows lower range of usable flap deflections. Table 4.2 shows that the difference between landing and take-off flap deflection angle is 1° less for the Jun13 design than for the others.

	Jun10	Jun12	Jun13	Jun15
+	high $C_{l_{max}}$	high payload good T-O perf.	high payload	good T-O perf.
-	large fairing	flap l.e. too forward	moderate T-O perf.	low payload

Table 4.3: Advantages and disadvantages of the optimized designs.

To overcome the take-off performance deficit, another optimization was run, the Jun15, which had more limits on the b-spline control points location which increased the $(C1_X - C2_X)_{eff}$ by 20% with respect to the Jun13 case, but was the only design that had considerably lower maximum lift coefficient and payload. Realizing that the take-off performance deficit of the Jun13 result is small, the author feels that this design is the most suitable for implementation on the Panthera aircraft. The advantages and disadvantages of the four designs are summarized in table 4.3. C_P distributions over the Jun13 airfoil are available in appendix A.2

Looking again at the bar chart in figure 4.4, some patterns emerge. All of the designs have similar δ_f values approximately in the middle of the design window. This is a compromise between higher circulation at high angles of attack and flow separation at lower angles of attack. All of the designs have relatively high $dR1$ value, which represents the radius close to the C_2 point (see figure 3.2a). High radius will offer more margin against separation at that point. Another observations is that the $C_1 - C_2$ parameter can only be large if the hinge is long (low HP_Y, Jun10), otherwise the flap does not deploy far enough out of the cove with the same δ_f.

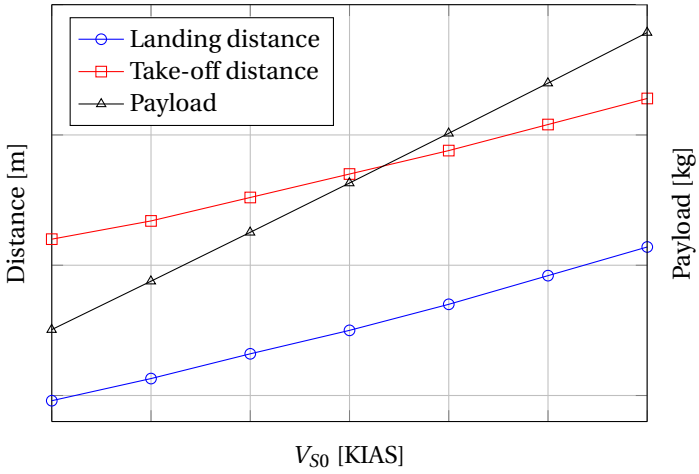

Figure 4.6: Payload and field length dependency on stall speed V_{S0}.

Panthera's take-off and landing distance with plain flaps are 540 m and 570 m respectively, but they increase considerably when the $MTOW$ is increased (see s_{T-O} and $s_{landing}$ in table 4.2) due to new high lift system while the stall speed V_{S0} is kept constant. It is possible to sacrifice some of the $MTOW$ (and thus payload) by decreasing the V_{S0} to decrease the field length, as shown in figure 4.6. This analysis takes into account the decrease in weights of fuel, wing and landing gear as a function of $MTOW$.

The final three-dimensional flap geometry is obtained by applying the same parametrization to the airfoils at the inboard and outboard flap edge respectively. The flap and main element are then generated as a loft of the three spanwise two-element airfoils, see figure 4.7.

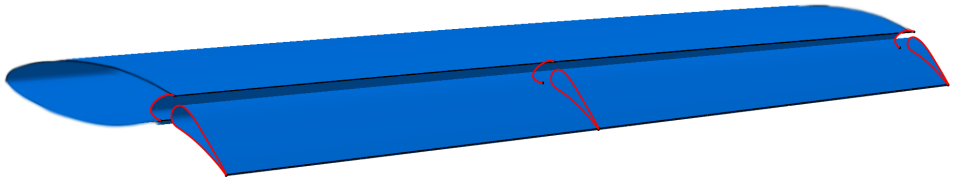

Figure 4.7: Final three-dimensional geometry of the flap and main element. Part of the figure masked due to NDA.

4.2. CONCLUSIONS AND RECOMMENDATIONS

From the discussion of the optimization results in section 4.1, as well as from the whole design process, the following conclusions can be made.

- A simple dropped hinge mechanism can be used to achieve sufficient high lift performance to increase the maximum lift coefficient of the aircraft by 13% with respect to a plain flap high lift system.
- If the stall speed and range are kept constant, the $MTOW$ increases by 13% and the payload increases by 42%. Take-off distance increases by 12.5% and landing distance by 16.5%, but can be traded off with a decrease in payload if the stall speed is decreased.
- The additional cruise drag due to hinge fairings increases the fuel weight for the range of 1000 nm by 3% for a hinge position of $0.15c$ below the chord line and three supports per flap.
- Limiting phenomena in determining the highest lift coefficient is the bursting of main element's wake, rather than flow separation off the surface.
- When it is not feasible to compute the whole angle of attack range in each iteration during an optimization, three angles of attack (-5°, 8° and 12°)are enough to avoid jumps in the lift curve if a limit on boundary layer displacement thickness at the flap trailing edge is used as a constraint.

Asking the original research question, what is the optimal high lift system design for a highly efficient 4-seater general aviation aircraft for improved payload, it can be concluded that a single slotted flap with a simple dropped hinge is the best compromise between complexity and performance for such an application.

During the project, the following recommendations for further research came to the author's attention.

- The model for prediction of fairing drag might be underpredicting the actual drag, therefore a CFD simulation of such fairings in combination with the wing should be performed for validation.
- The present optimization scheme would only need a minor extension to allow the analysis of more complex flap mechanisms such as a four bar linkage. This could be implemented in future to analyse the benefits of such a system, if a designer is willing to implement a more complex solution.
- It should be investigated why the MSES convergence is dependent on slight changes in mesh size for the same case, while the meshes that do converge give almost identical results. If convergence on any mesh size (within a certain range) could be achieved, the computation time could be reduced by a factor of about 4.
- Before flight-testing the designed single-slotted flap, wind tunnel tests should be performed, especially to investigate the possibility of stall hysteresis.

BIBLIOGRAPHY

[1] J. Roskam. *New airfoils and higher wing loadings: a new look at general aviation airplane design.* TU Delft, 1974.

[2] W. H. Jr. Wentz and H. C. Seetharam. Development of a fowler flap system for a high performance general aviation airfoil. Technical Report CR-2443, NASA, 1974.

[3] B. Eggleston, W.D. McKinney, J. Banaszek, N.S. Choi, G. Krolikowski, F. Lebrun, J. Thompson, D.W. Zingg, M. Nemec, and S. De Rango. Development of a new flap for a light utility transport aircraft. *Canadian Aeronautics and Space Journal*, 48(4):233–238, 2002.

[4] D. Zaccai. Design framework for trailing edge high-lift systems, a knowledge based engineering application. Master's thesis, TU Delft, Faculty of aerospace engineering, 2014.

[5] F.G.A. Bertels. Design framework for flap system kinematics, a knowledge based engineering application. Master's thesis, TU Delft, Faculty of aerospace engineering, 2012.

[6] E. Moerlands. Development of an aeroelastic analysis tool for structural sizing of high-lift devices during preliminary design. Master's thesis, TU Delft, Faculty of aerospace engineering, 2011.

[7] T. van den Berg. Parametric modeling and aerodynamic analysis of multi-element wing configurations. Master's thesis, TU Delft, Faculty of aerospace engineering, 2009.

[8] A.R. Hoogendijk. Knowledge engineering in high lift design. Master's thesis, TU Delft, Faculty of aerospace engineering, 2004.

[9] Robert H. Liebeck. Design of subsonic airfoils for high lift. *AIAA Journal*, 15(9):547–561, 1978.

[10] A.M.O. Smith. High-lift aerodynamics. *AIAA Journal*, 12(6):501–530, 1975.

[11] John D. Anderson. *Aircraft performance and design.* WCB/McGraw-Hill, 1999.

[12] B.S. Stratford. The prediction of separation of the turbulent boundary layer. *Journal of Fluid Mechanics*, 5(1):1–16, 1959.

[13] M.J. Lighthill. A new method of two-dimensional aerodynamic design. *Aeronautical Research Council*, 1945.

[14] Carl J. Wenzinger and Thomas A. Harris. Wind-tunnel investigation of an NACA 23012 airfoil with various arrangements of slotted flaps. Technical Report 664, NACA, 1939.

[15] P.K.C. Rudolph. High-lift systems on commercial subsonic airliners. Technical Report CR-4746, 1996.

[16] Daniel P. Raymer. *Aircraft Design: A Conceptual Approach.* AIAA Education Series, 5th edition, 2012.

[17] Snorri Gudmundsson. *General aviation aircraft design.* Butterworth-Heinemann, 2013.

[18] Jones F. Cahill. Summary of section data on trailing-edge high-lift devices. Technical Report 938, NACA, 1949.

[19] W.O. Valarezo, D.J. Chet, and R.J. McGhee. Multielement airfoil performance due to reynolds and mach number variations. *AIAA Journal*, 30(5):689–694, 1993.

[20] J. Wild. Mach and reynolds number dependencies of the stall behaviour of high-lift wing-sections. *AIAA Journal*, 50(4):1202–1216, 2013.

[21] W.O. Valarezo, D.J. Chet, R.J. McGhee, W.L. Goodman, and K.B. Paschal. Multielement airfoil optimization for maximum lift at high reynolds numbers. 9th AIAA Applied Aerodynamics Conference, pages 969–976, Baltimore, MD, U.S.A., September 1991.

[22] K. Biber. Stall hysteresis of an airfoil with slotted flap. *Journal of aircraft*, 42(6):1462–1470, 2005.

[23] M. Baragona, L.M.M. Boermans, M.J.L. van Tooren, H. Bijl, and A. Beukers. Bubble bursting and stall hysteresis on single-slotted flap high-lift configuration. *AIAA Journal*, 41(7):1230–1237, 2003.

[24] IB. Photo from www.flythenw.com. Accessed 30th September 2014.

[25] J. Mac McClellan. Why the skylane endures - http://www.flyingmag.com/pilot-technique/new-pilots/why-skylane-endures, 2014, accessed 9th September 2014.

[26] PetrolHead. Photo from www.modelbouwforum.nl, 2012. Accessed 30th September 2014.

[27] G.T. Palecek. Photo from www.weekendcfii.com, 2008. Accessed 30th September 2014.

[28] M. Danko. Photo from www.aviationlawmonitor.com, 2010. Accessed 30th September 2014.

[29] ROSSR. Photo from http://pilotlove.com, 2013. Accessed 30th September 2014.

[30] Photo from www.cessna.com. Accessed 30th September 2014.

[31] Pipistrel panthera technical data - http://www.panthera-aircraft.com/technical-data, accessed 30th September 2014.

[32] Diamond technical data - http://www.diamondaircraft.com/, accessed 30th September 2014.

[33] Cirrus technical data - http://cirrusaircraft.com/, accessed 30th September 2014.

[34] Piper technical data - http://www.piper.com/, accessed 30th September 2014.

[35] Beechcraft technical data - http://www.beechcraft.com/, accessed 30th September 2014.

[36] P.K.C. Rudolph. Mechanical design of high lift systems for high aspect ratio swept wings. Technical Report CR-196709, 1998.

[37] S.P. Schoensleben. Integrated trailing edge flap track mechanism for commercial aircraft. Master's thesis, Swiss Federal Institute of Technology Zurich, 2006.

[38] Cirrus illustrated parts catalog - http://servicecenters.cirrusdesign.com/techpubs/pdf/ipc/sr20/html/ipcmain.asp, accessed 30th September 2014.

[39] Beech Aircraft Corporation. *Parts Catalog - Bonanza model 35 through G35*, 1962.

[40] SKF. Linear actuators product range - http://www.skf.com/group/products/actuation-systems/linear-actuators/, accessed 11th June 2015.

[41] E. Torenbeek. *Synthesis of subsonic airplane design*. Delft university press, 1982.

[42] G. Seljak. Preizkus numericnih metod v programu openfoam za obravnavo sistemov visokega vzgona. Master's thesis, Univerza v Ljubljani, Fakulteta za matematiko in fiziko, 2013.

[43] *Federal Aviation Regulations, Part 23*. Federal Aviation Administration, 2014.

[44] Mark Drela. Newton solution of coupled viscous/inviscid multielement airfoil flows. AIAA 21st Fluid Dynamics, Plasma Dynamics and Lasers Conference, Seattle, WA, U.S.A, June 1990. AIAA.

[45] Borre W. Lokenhagen. Evaluation of the mses code version 2.9 - comparison with experimental results. Master's thesis, TU Delft, Faculty of aerospace engineering, 1996.

[46] R.S. Pepper, C.P. van Dam, and P.A. Gelhausen. Design methodology for high-lift systems on subsonic transport aircraft. 6th AIAA, NASA, and ISSMO Symposium on Multidisciplinary Analysis and Optimization, Belleuve, WA, U.S.A., September 1996.

[47] C.L. Rumsey and J.P. Slotnick. Overview and summary of the second AIAA high lift prediction workshop (invited). 52nd Aerospace Sciences Meeting, Maryland, U.S.A., January 2014.

[48] Rutten P.B. Boermans, L.M.M. Two-dimensional aerodynamic characteristics of airfoil NLF-MOD22 with fowler flap. Technical report, Delft University of Technology, 1995.

[49] E. Omar, T. Zierten, M. Hahn, E. Szpiro, and A. Mahal. Two-dimensional wind-tunnel tests of a NASA supercritical airfoil with various high-lift systems. Technical Report CR-2215, NASA, 1973.

[50] Mark Drela. *A Users's Guide to MSES 3.05*, 2007.

[51] Anon. ESDU 91014: Maximum lift of with trailing-edge flaps at low speeds. Technical report, ESDU.

[52] Anon. ESDU 93019: Wing lift coefficient increment at zero angle of attack due to deployment of single-slotted flaps at low speeds. Technical report, ESDU.

[53] A.D. Young. The induced drag of flapped elliptic wings with cut-out and with flaps that extend the local chord. Technical report, Aeronautical Research Council, 1951.

[54] B. Maskew. Program VSAERO theory document - a computer program for calculating nonlinear aerodynamic characteristics of arbitrary configurations. Technical report, NASA, 1987.

[55] T.H.G. Megson. *Aircraft Structures For Engineering Students*. Elsevier, 4th edition, 2007.

[56] Sighard F. Hoerner. *Fluid-dynamic drag*. Hoerner Fluid Dynamics, 1965.

[57] E.F. Zaparka. Airplane control apparatus, February 14 1939. US Patent 2,147,360.

[58] D.R.M. Jeffrey and D.W. Hurst. Aerodynamics of the gurney flap. 14th AIAA Applied Aerodynamics Conference, New Orleans, LA, U.S.A., June 1996.

[59] J.J. Wang, Y.C. Lia, and Choi K.-S. Gurney flap - lift enhancement, mechanisms and applications. *Progress in Aerospace Sciences*, 44(1):22–47, 2008.

[60] M. Papadakis, Wong S.C., Yeong H.W., and D. Ellis. Aerodynamic performance of an innovative flap design. 37th Aerospace Sciences Meeting, Reno, NV, U.S.A., January 1999. AIAA.

[61] R.A. Nahas. Auxiliary wing and flap assembly for an aircraft, June 22 2010. US Patent 7,740,205.

[62] S.Z. Zhu and Y. Qiu. Studies in application of zhu's flap to high lift system for aircrafts. AIAA Atmospheric Flight Mechanics Conference and Exhibit, San Francisco, CA, U.S.A., August 2005.

A

APPENDIX

A.1. MSES VALIDATION

The following figures show computational results obtained with MSES code in comparison to experimental results obtained in two series of wind tunnel tests. Figures A.1 to A.11 show comparison with experimental results from Boeing Research Wind Tunnel, reference [49]. The airfoil tested is shown in figure A.1 in clean configuration and in figure A.4 in configuration with a single slotted flap. Figures A.12 to A.15 present comparison with experimental results from Delft University of Technology Low Speed Wind Tunnel, reference [48]. The airfoil tested is shown in figure A.12.

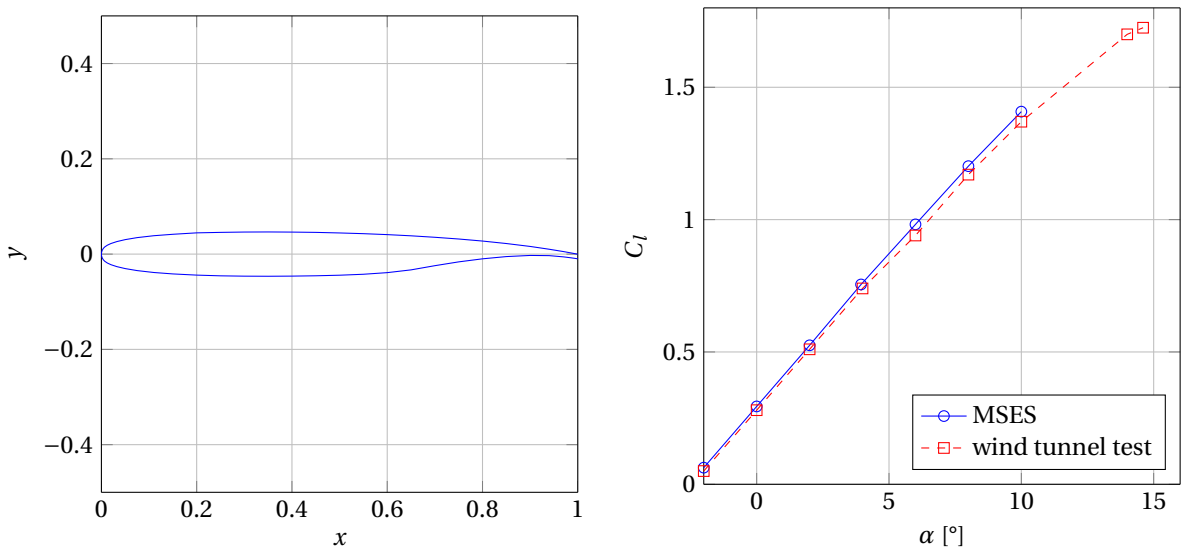

(a) **(b)**

Figure A.1: Clean airfoil from [49] (a) and its lift curve (b).

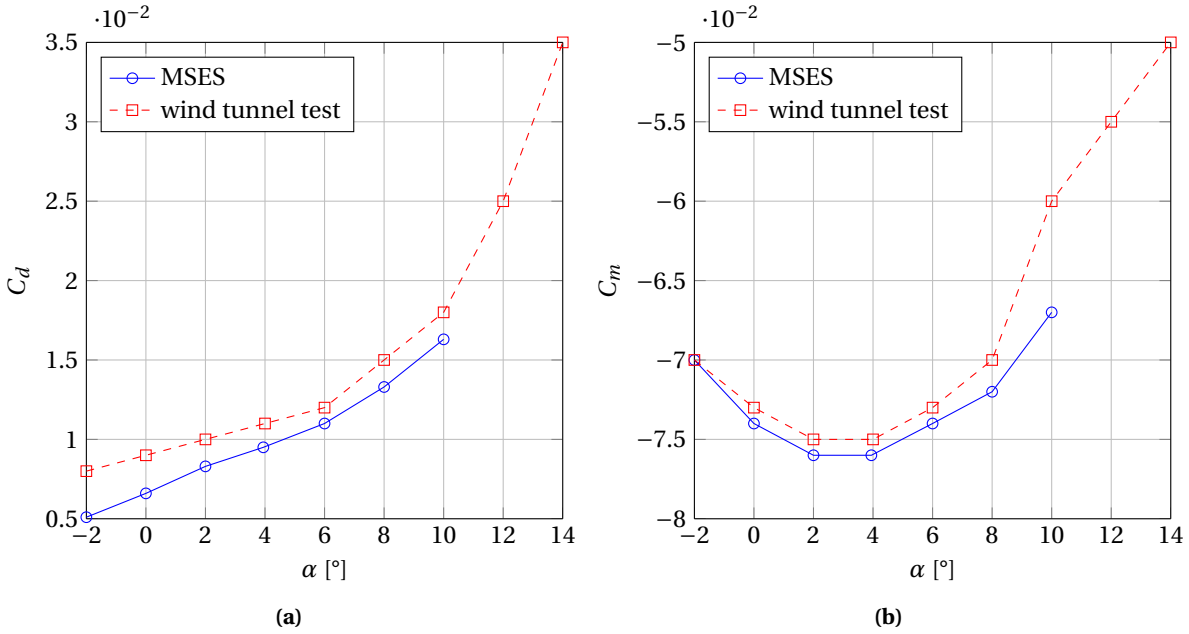

Figure A.2: C_d (a) and C_m (b) for clean airfoil from [49].

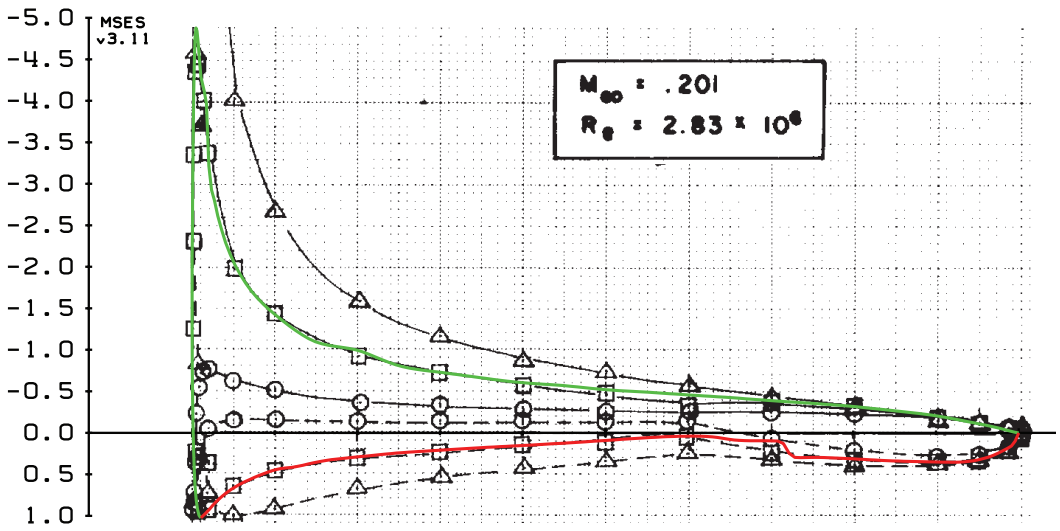

Figure A.3: Comparison of computed and measured C_p over a clean airfoil from [49] at $\alpha = 6.1°$.

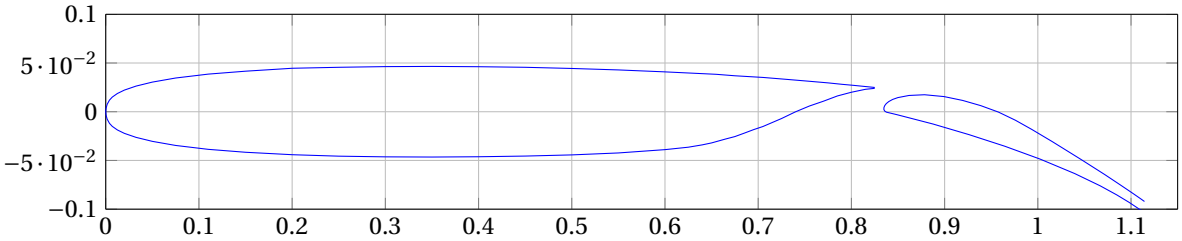

Figure A.4: Airfoil from [49], here shown in the following configuration: $\delta_f = 20°$, gap = $0.02c$, overlap = $0.01c$.

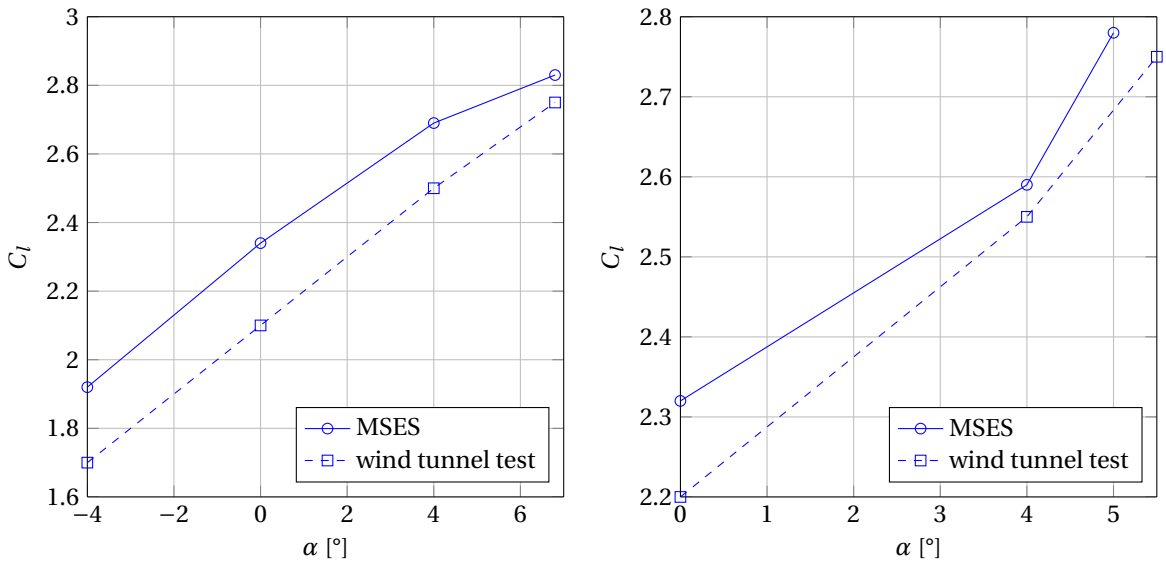

(a) $\delta_f = 30°$ **(b)** $\delta_f = 40°$

Figure A.5: Lift coefficient at different flap deflection angles. Solid line is computation (MSES), dashed line is wind-tunnel test from [49]

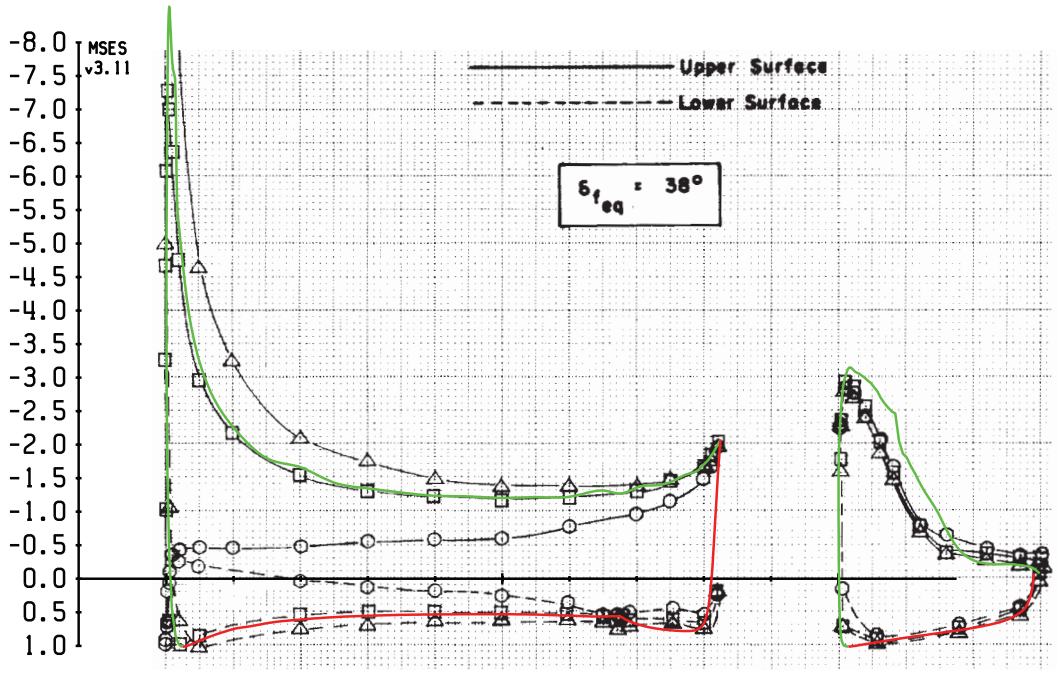

Figure A.6: Comparison of computed and measured C_p over the airfoil from [49] with $\delta_f = 40°$ at $\alpha = 0$ °.

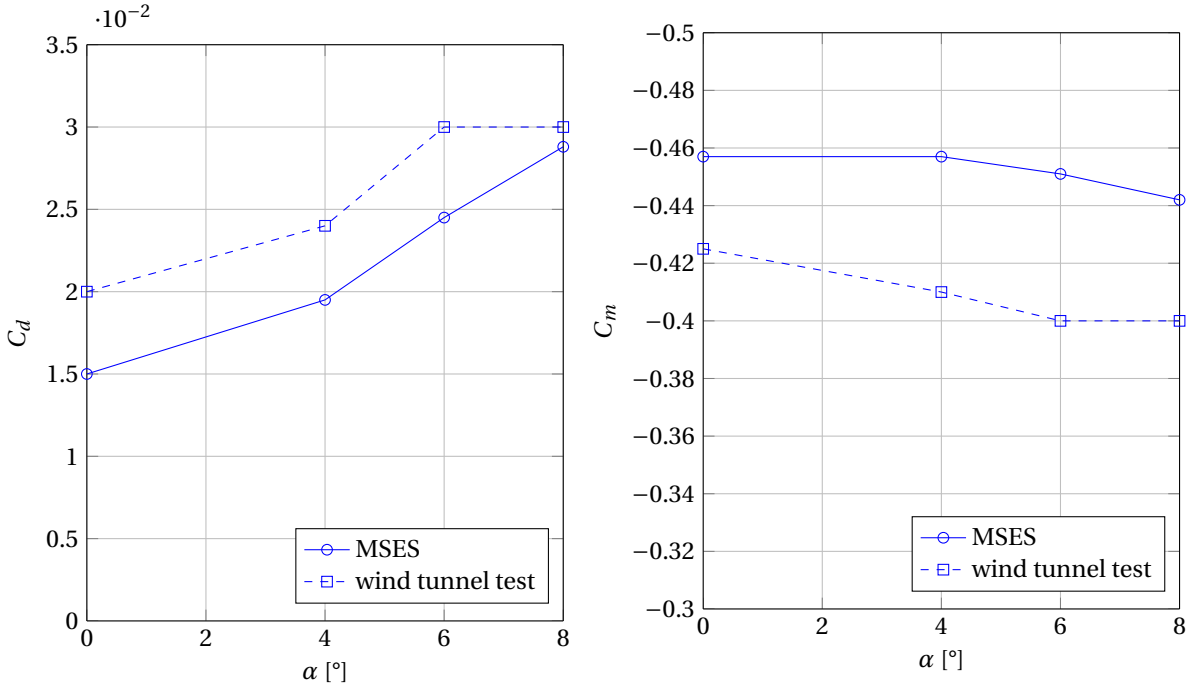

(a) Drag coefficient

(b) Pitching moment coefficient

Figure A.7: Comparison of drag and pitching moment coefficient prediction for $\delta_f = 20°$ (wind tunnel test from [49])

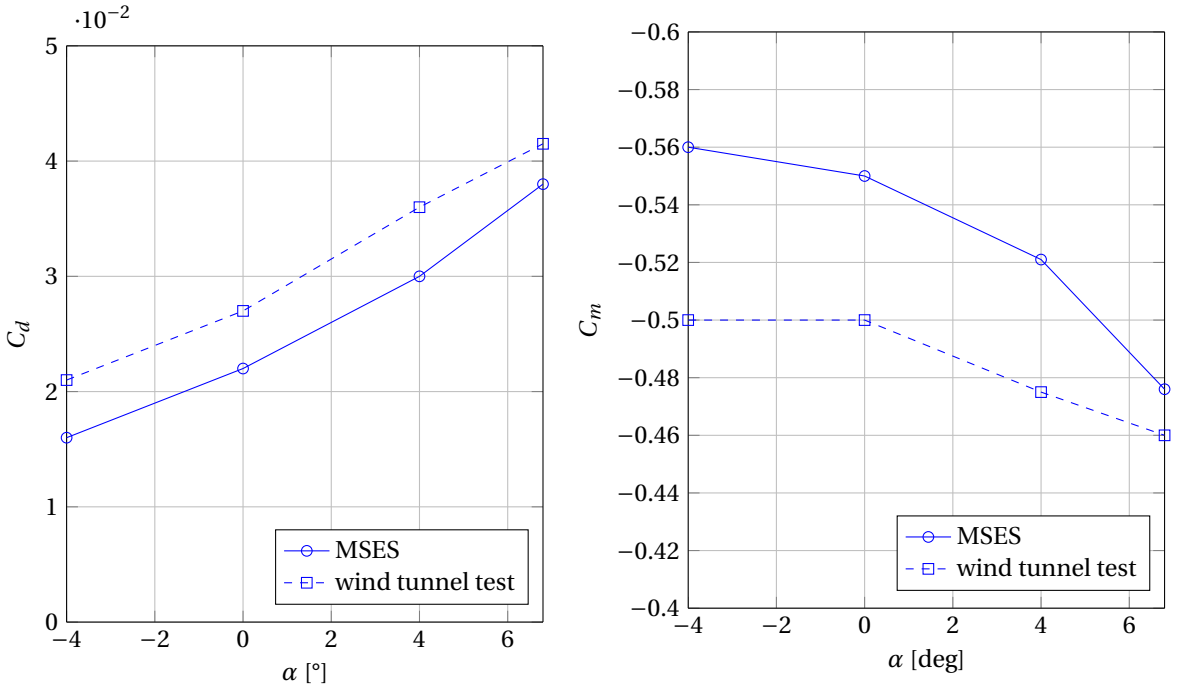

(a) Drag coefficient

(b) Pitching moment coefficient

Figure A.8: Comparison of drag and pitching moment coefficient prediction for $\delta_f = 30°$ (wind tunnel test from [49])

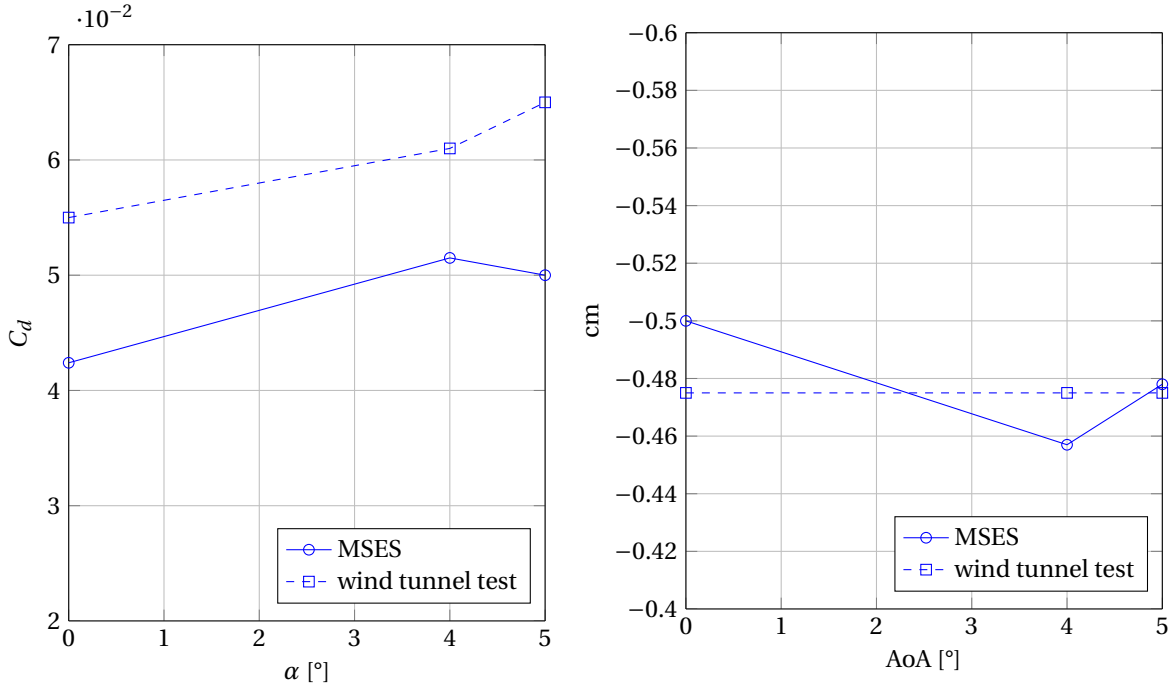

(a) Drag coefficient

(b) Pitching moment coefficient

Figure A.9: Comparison of drag and pitching moment coefficient prediction for $\delta_f = 40°$ (wind tunnel test from [49])

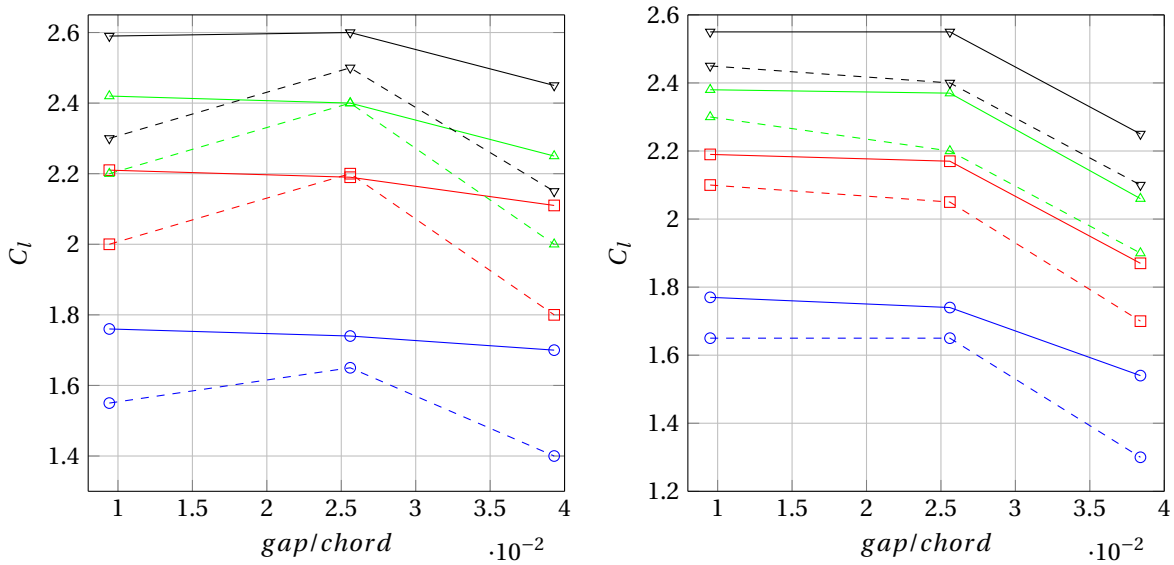

(a)

(b)

Figure A.10: Lift coefficient w.r.t. gap size for $\alpha = 0°$, 4°, 6° and 8° at constant overlap of 0 (a) and $0.025c$ (b) and flap deflection angle of 20°. Solid line is computation (MSES), dashed line is wind tunnel test from [49].

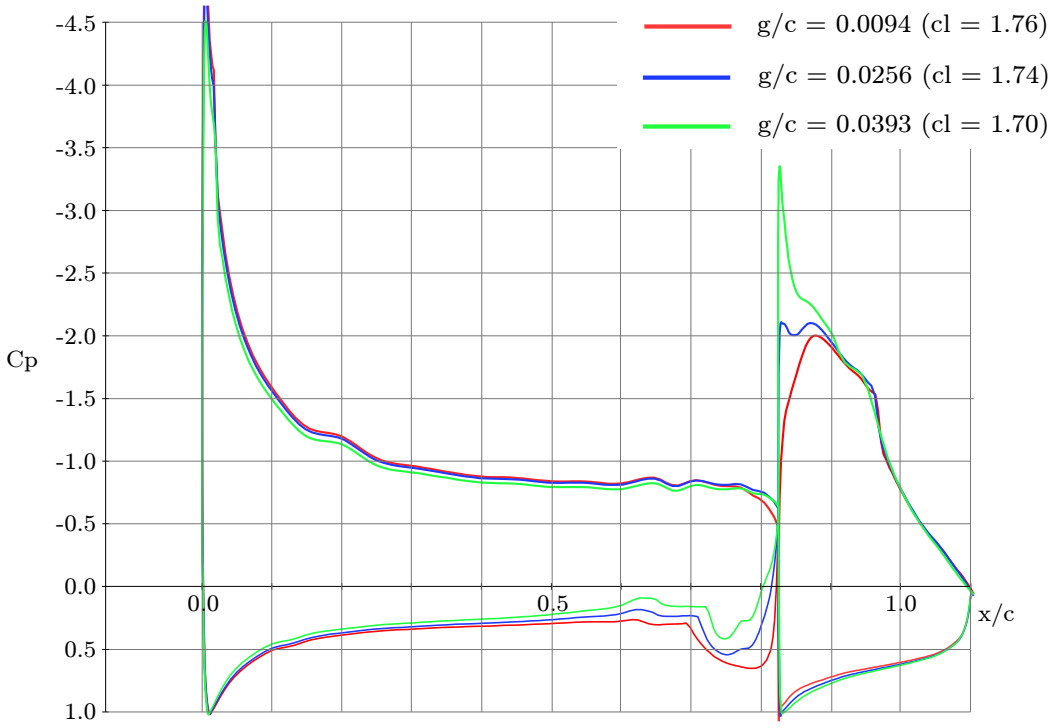

Figure A.11: Computed C_p distributions for different gaps at $\alpha = 0$ and $\delta_f = 20°$.

Figure removed from public version of the thesis report due to confidentiality reasons.

Figure A.12: Airfoil from [48], here shown in the following configuration: $\delta_f = 15°$, gap = $0.02c$, overlap = $0.08c$.

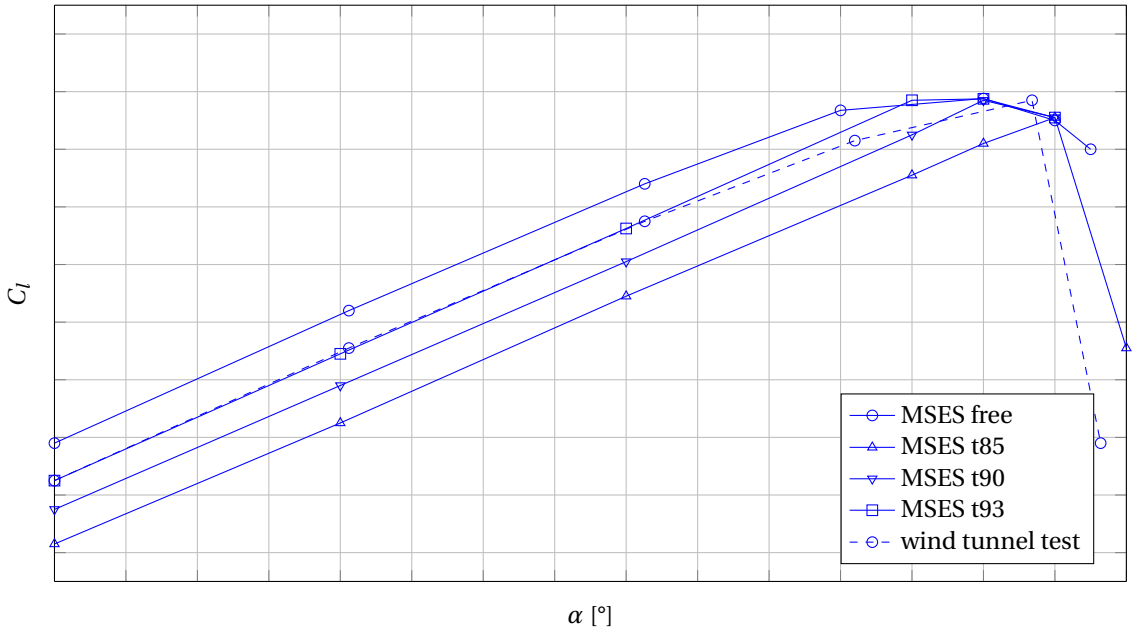

Figure A.13: Comparison of lift curves for NLF-MOD22(A), δ_f = 30°, gap = 0.03c, overlap = 0.01c (wind tunnel test from [48])

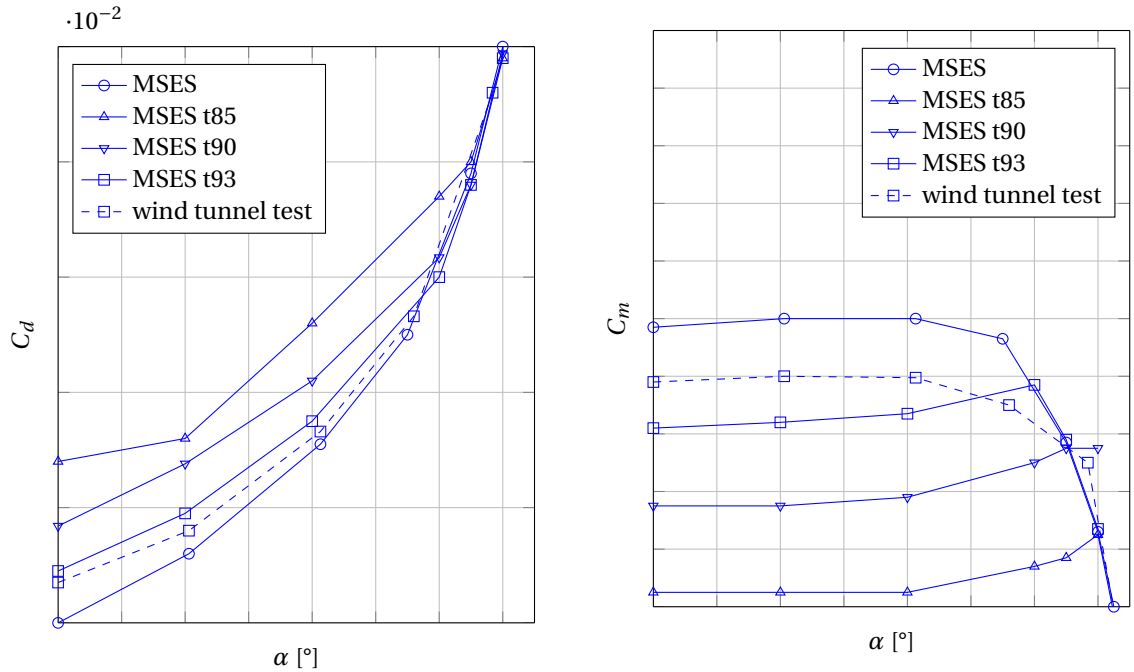

(a) Drag coefficient

(b) Pitching moment coefficient

Figure A.14: Comparison of drag and pitching moment coefficient prediction for δ_f = 30°, gap = 0.03c, overlap = 0.01c (wind tunnel test from [48])

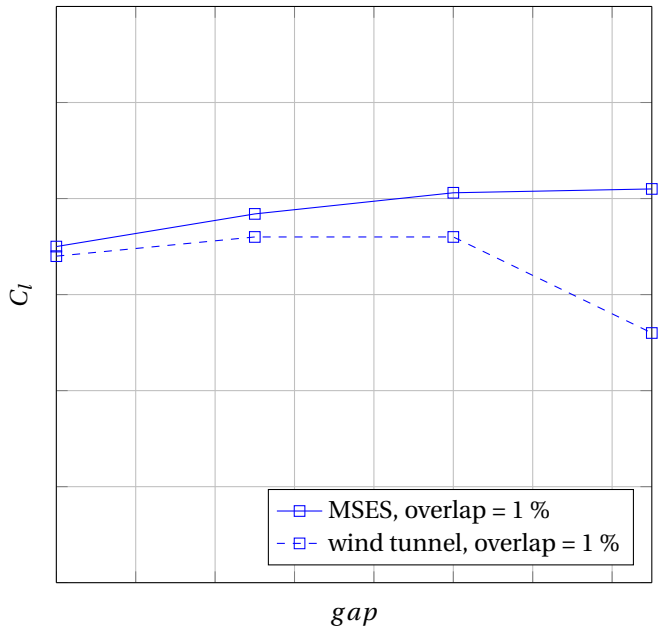

Figure A.15: Lift coefficient w.r.t. gap size for NLF-MOD22(A) with $\delta_f = 30\,°$

A.2. PRESSURE DISTRIBUTIONS

Section removed from the public version of the thesis report due to confidentiality reasons.

A.3. FLAP LOADS IN RETRACTED AND DEPLOYED POSITION

To compare the loads on the flap in retracted and deployed configuration, the FAR 23 [43] load factors need to be considered. Appendix A of the FAR 23 provides simplified design load criteria. Table 1 in section A23.13 of the FAR 23 states that the ultimate load factor of the utility category aircraft is 4.4 with flaps retracted and 2.2 with flaps deployed. Figure A.16 shows the flight envelopes for the aircraft with flaps retracted and deployed (landing position). The envelopes are limited with minimum and maximum velocities: the minimum velocity is 30 m/s (59 KIAS) and the maximum is 104 m/s. The maximum velocity with flaps deployed is limited to 45 m/s, also known as the flap Placard speed.

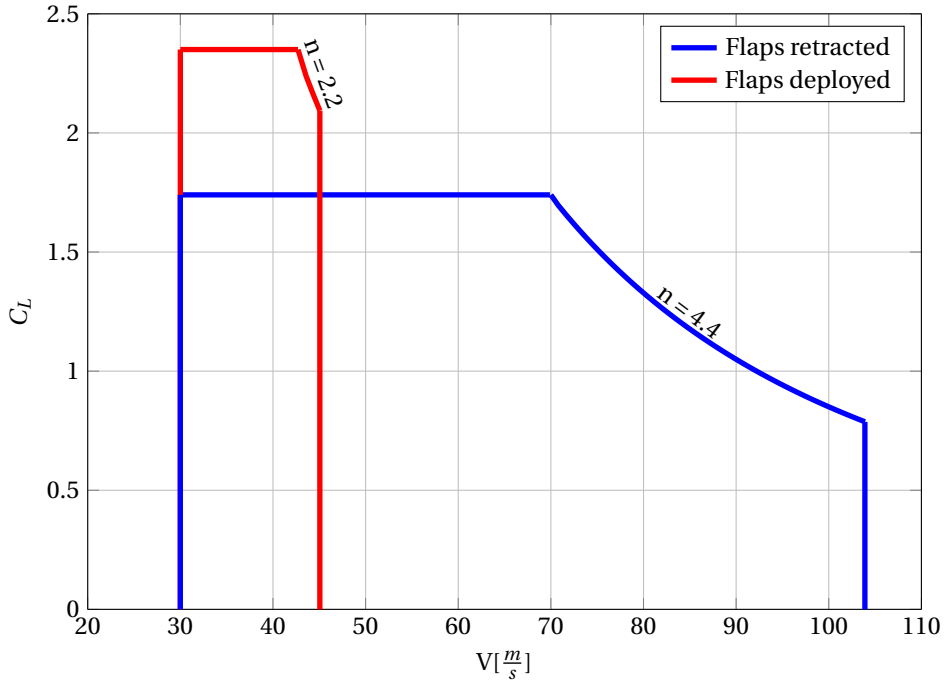

Figure A.16: Flight envelope.

Figure A.17 shows the pressure distributions on the clean airfoil at two angles of attack. It can be seen that the C_n on the flap (bold portions of the curves) is approximately the same for small and high angles of attack. This indicates that the highest loading on the flap, calculated with equation (A.1), will be at low lift coefficient and maximum speed. $C_{n_{flap}}$ in equation (A.1) can be seen as the averaged sectional $C_{n_{flap}}$ along the span of the flap. Therefore, the critical load cases to be compared are the V = 104 m/s for the flap retracted and V = 45 m/s for the flap deployed. To compared the loadings, only the $C_{n_{flap}} \cdot V^2$ can be compared as the other values from equation A.1 are constant for both cases. Table A.1 lists the results of the comparison, showing that the flap is loaded more in retracted than in deployed position. $C_{n_{flap}}$ in deployed configuration is calculated from pressure distributions in appendix A.2.

$$F_{flap} = \frac{1}{2}\rho V^2 S_{flap} C_{n_{flap}} \tag{A.1}$$

Configuration	n	V	C_L	α	$C_{n_{flap}}$	$C_{n_{flap}} \cdot V^2$
flap retracted	4.4	104 $\frac{m}{s}$	0.78	3 °	0.093	1005 $\frac{m^2}{s^2}$
flap deployed	2.2	45 $\frac{m}{s}$	2.1	9 °	0.46	931.5 $\frac{m^2}{s^2}$

Table A.1: Loads on the flap in retracted and deployed position.

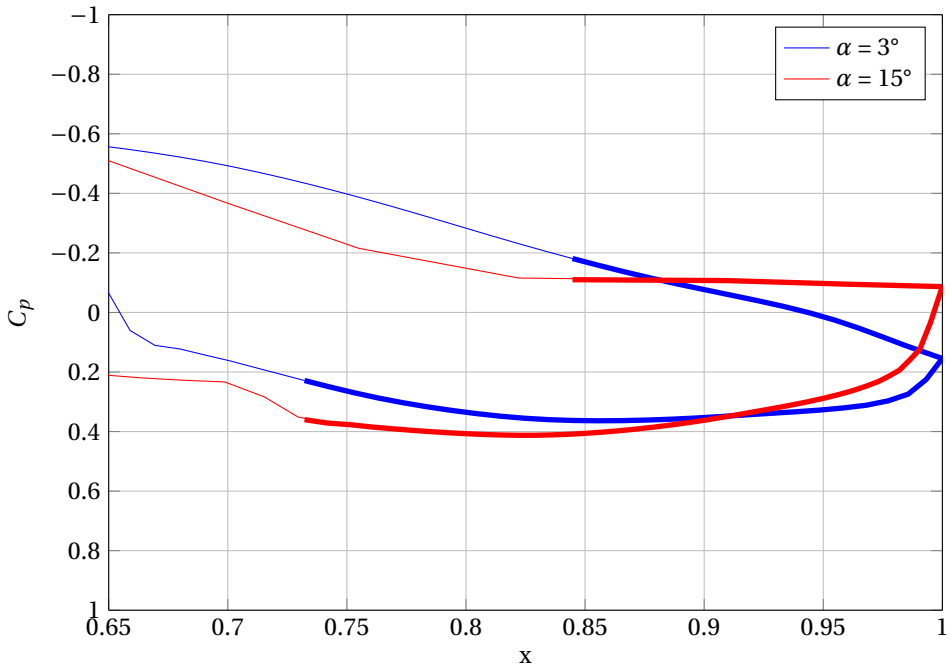

Figure A.17: Pressure distributions over the clean airfoil at two angles of attack. Bold curves indicate the pressure coefficient on the flap surface that is wetted by the flow in retracted position.

A.4. OBJECTIVE FUNCTION HISTORY

Figure A.18 shows the history of objective function for the optimization runs discussed in section 4. All the optimizations start with a relatively low objective value because a preliminary generation with the population size of 1000 was run prior to each run that yielded 100 initial designs for the runs showed in figure A.18.

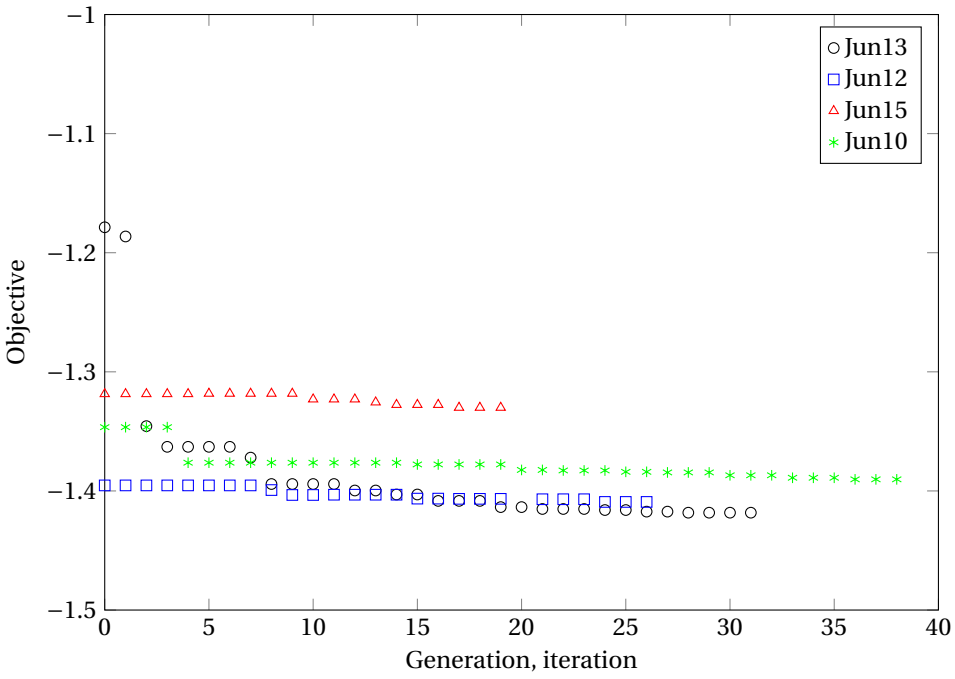

Figure A.18: Objective function value during optimization runs.

A.5. UNCONVENTIONAL HIGH LIFT DEVICES

In section 2.1.2 the high lift devices that are in common use in general aviation aircraft have been presented and they are the most likely candidates for the improved design of Pipistrel Panthera. There are numerous other concepts of high lift devices that have been proposed, but are not in use due to various reasons, most commonly the complexity of the design. Although this section is called Unconventional high lift devices, some of them have been used in the past or are still in use in some examples.

Zap flap

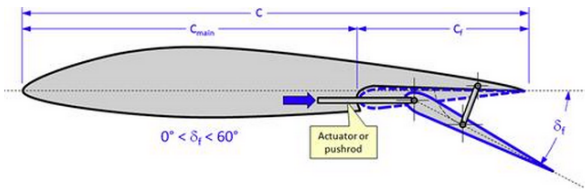

Figure A.19: Zap flap (from [17])

Zap flap was patented in 1933 [57]. It can be explained as a split flap with additional Fowler motion. There are no external supports needed for the Zap flap. A screw drive can be used as a pushrod, while the aft support is just a simple link, hinged on both ends. However, the pushrod must extend into the main wing, possibly penetrate the rear spar, when in stowed position. The aft link could be mounted on an external bracket on the flap in order to keep the upper surface of the flap closed.

Gurney flap

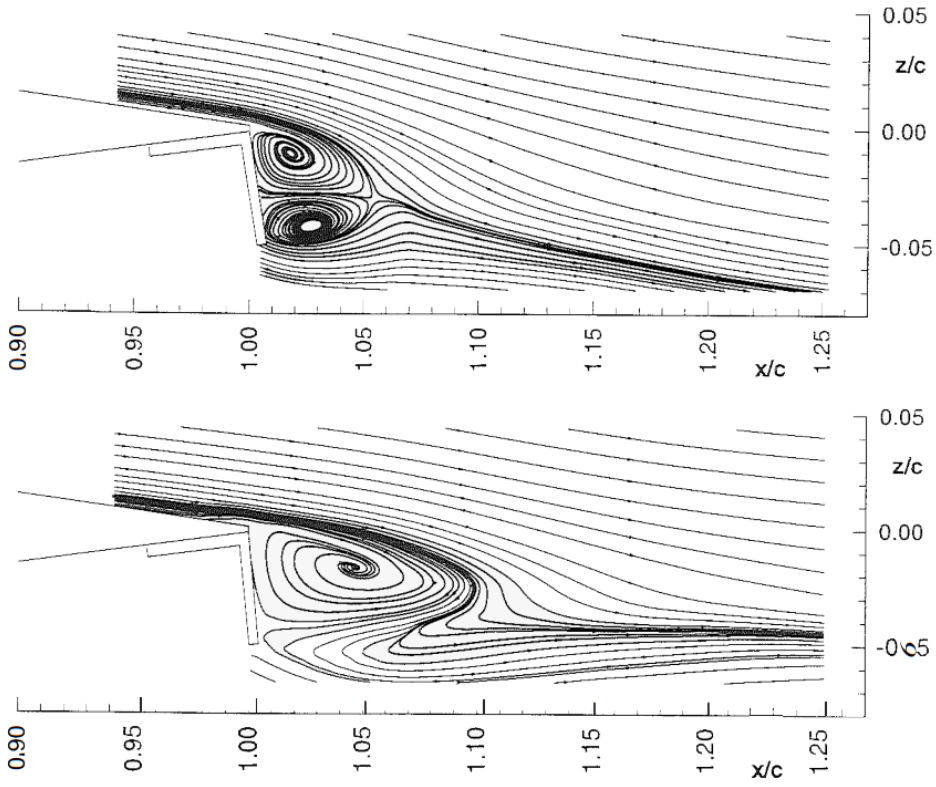

Figure A.20: Flow downstream of the Gurney flap; top figure: $\alpha = 0$, bottom figure: $\alpha = 10°$ (from [58])

Gurney flap is one of the rare inventions that came into aerospace industry from motorsport and not the other way around. Its inventor, Dan Gurney, is a well known American race car designer and driver. It is a simple thin plate mounted perpendicularly to the pressure side of the airfoil at its trailing edge. Usual Gurney

flap heights are from 1% to 5% of the chord length. Increase in C_l of up to 30% for single-element airfoils and up to 10% for two-element airfoils are reported in reference [59].

The flow about the Gurney flap was investigated in detail in reference [58]. At low angles of attack, two counter-rotating vortices form downstream of the flap. At higher angles of attack, the vortex from the suction side dominates the flow, see figure A.20. This vortex increases the circulation of the airfoil and its dumping velocity, as it acts similarly to adding another element behind the main airflow. Lift curve of the airfoil equipped with a Gurney flap shifts upwards, as with the addition of a second element. The disadvantage of the Gurney flap is that it increases the drag of the airfoil at low and moderate angles of attack, thus allowing substantially lower maximum L/D.

Variable incidence auxiliary (VIA) wing

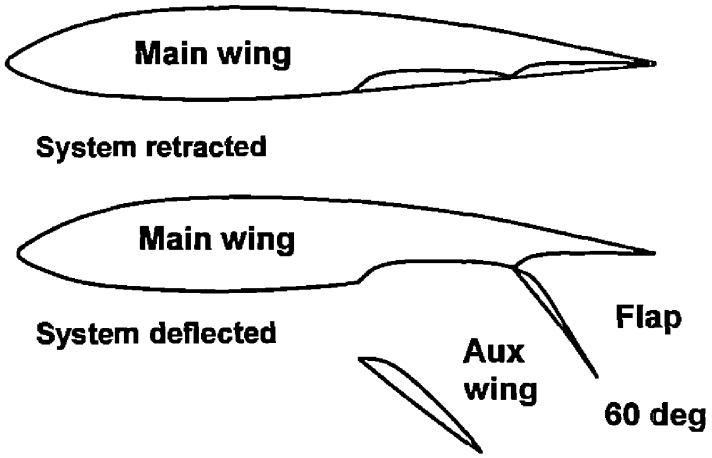

Figure A.21: VIA wing accompanied with the split flap at the trailing edge (from [60])

VIA wing (figure A.21) was patented by Roger Nahas [61]. The invention was meant for use on light general aviation aircraft. Wind tunnel results are presented in reference [60]. Maximum section lift coefficients measured were just below 2.0, which is lower than what can be achieved with plain and split flaps.

Zhu's flap

Reference [62] proposes a thin flap of full chord length above the main airfoil (figure A.22), named Zhu's flap after its inventor. Wind tunnel tests of a three dimensional aircraft model fitted with Zhu's flap were made at a Reynlods number of $1.89x10^5$. Increase in C_{Lmax} in comparison to the clean airfoil was about 0.7, giving the maximum three-dimensional lift coefficient of about 1.5. Relatively low values are due to low Reynlods number. In general, there is no improvement in comparison to the plain flap.

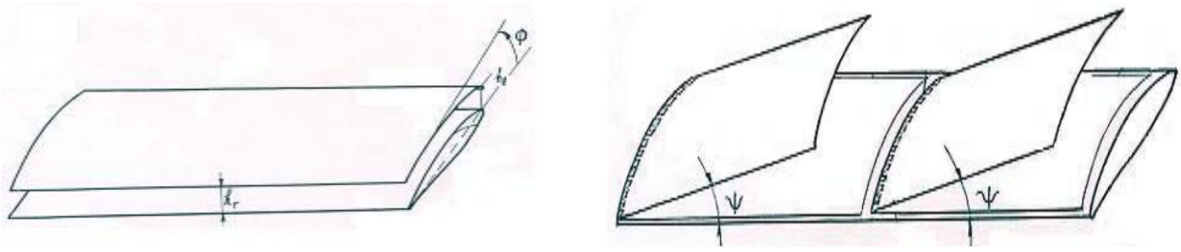

Figure A.22: Parallel Zhu's flap (left) and sloped Zhu's flap (right) (from [62])

A.6. MSES AUTOMATION SCRIPT

The following script was used to automate the MSES code with the commands from the Linux terminal. The most basic version of the automation script is presented.

```
#! /bin/csh

set xxx = $1 # name of .dat file without extension
set alfa = $2 # angle of attack
set re = $3 # Reynolds number
set mach = $4 # Mach number
set nrp = $5 # nr. of grid points per airfoil side

set niter_i = 30 # Number of iterations for msis, inviscid
set niter_v = 80 # Number of iterations for msis, viscous

set casename = "$xxx"_"$alfa"_"$nrp" # casename includes the num. of airfoil points

#call mset and guide it with EOF commands EOF
mset $xxx $xxx.dat > msetLog$xxx << EOF

15
$casename
7
N
$nrp

1
$alfa
2
1
0.75 0.80 0.5

u
0.55 1 0.5

3
4
13
y
14
0
EOF

sed -i "s/0.05000/$mach/" mses.$casename # replace Mach in mses.casename file

msis $casename $niter_i > inviscidRun$casename # run msis with niter iterations

sed -i "s/0.000E+00/$re/" mses.$casename # replace Reynolds in mses.casename file

msis $casename $niter_v > solutionLog$casename # run msis again, now viscous

set solutionCheck = ‘cat solutionLog$casename‘
set solNrOfLines = $#solutionCheck
set convTest = $solutionCheck[$solNrOfLines]

if ( $convTest == "tolerance" ) then
```

```
# call mplot, log output to file, save cp(x) plot
# first create new folder where plot.ps is created
set itPos = 0
@ itPos = $solNrOfLines - 69
set convergedIteration = $solutionCheck[$itPos]
mkdir $casename
mv mdat.$casename $casename
cd $casename
mplot $casename > plotlog$casename << EOF
1
2
14
12

0
EOF
set plotname = "$xxx"_a"$alfa"_"$re"_"$mach"_"$nrp".ps""
mv plot.ps ../log/$plotname # rename plot

set resLine = `cat plotlog$casename` # save plotlog file to a variable,
 # each string has its number
mv mdat.$casename ../mdat.$casename
rm -f plotlog$casename
cd ..
rmdir $casename
set convlogFileName = ""convlog"$xxx"_"$alfa".dat""
echo $nrp $re $mach $alfa $resLine[208] $resLine[211] $resLine[214] $resLine[316] ...
... $resLine[319] $convergedIteration >>$convlogFileName # append this line to a file
# print to convlogALL
echo $xxx $nrp $re $mach $alfa $resLine[208] $resLine[211] $resLine[214] ...
... $resLine[316] $resLine[319] $convergedIteration >>convlogALL.dat
echo $nrp $alfa $resLine[208]
mkdir caseConverged
# call mplot again to output bl data
mplot $casename > plotlog$casename << EOF
12

0
EOF
rm -f plotlog$casename
mv mdat.$casename log/mdat.$casename
else
rm -f mdat.$casename
rm -f plotlog$casename
endif

rm -f blade.$casename
rm -f mses.$casename
rm -f solutionLog$casename
rm -f msetLog$xxx
rm -f inviscidRun$casename
```

A.7. ACTUATION MECHANISM

Figure A.23 is a supplement to the equations in subsection 3.4.5.

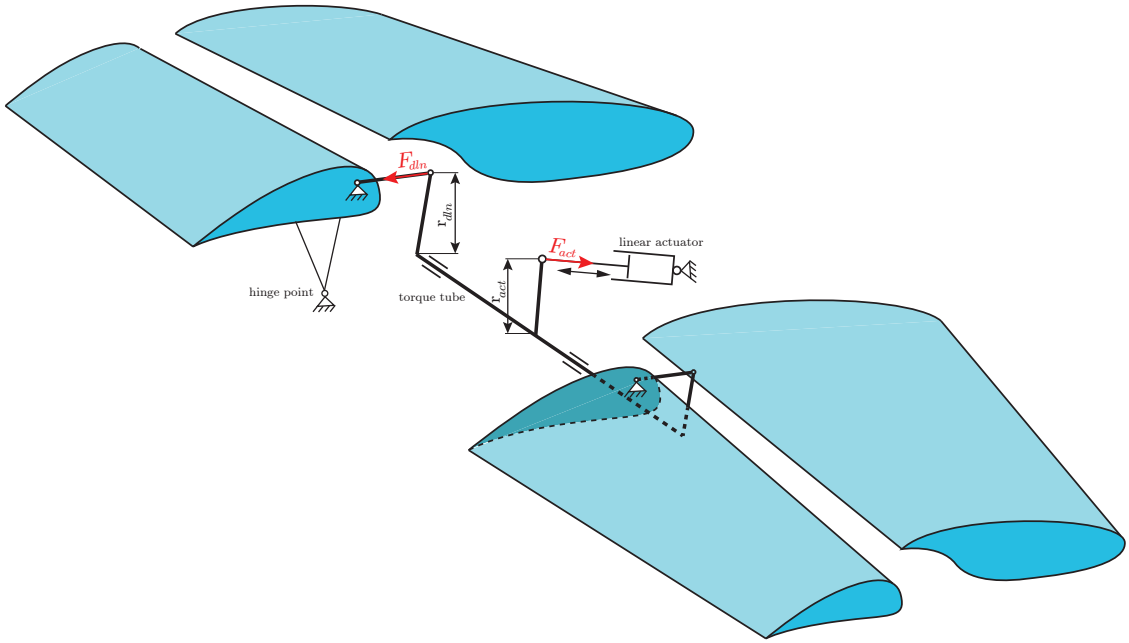

Figure A.23: Sketch of the proposed actuation mechanism layout for slotted flaps.